

**Dynamic laser speckle imaging for velocimetry in blood flow
A numerical study**

van As, K.

DOI

[10.4233/uuid:a24dac77-8bfd-4850-826b-c99fa5a7ace2](https://doi.org/10.4233/uuid:a24dac77-8bfd-4850-826b-c99fa5a7ace2)

Publication date

2024

Document Version

Final published version

Citation (APA)

van As, K. (2024). *Dynamic laser speckle imaging for velocimetry in blood flow: A numerical study*. [Dissertation (TU Delft), Delft University of Technology]. <https://doi.org/10.4233/uuid:a24dac77-8bfd-4850-826b-c99fa5a7ace2>

Important note

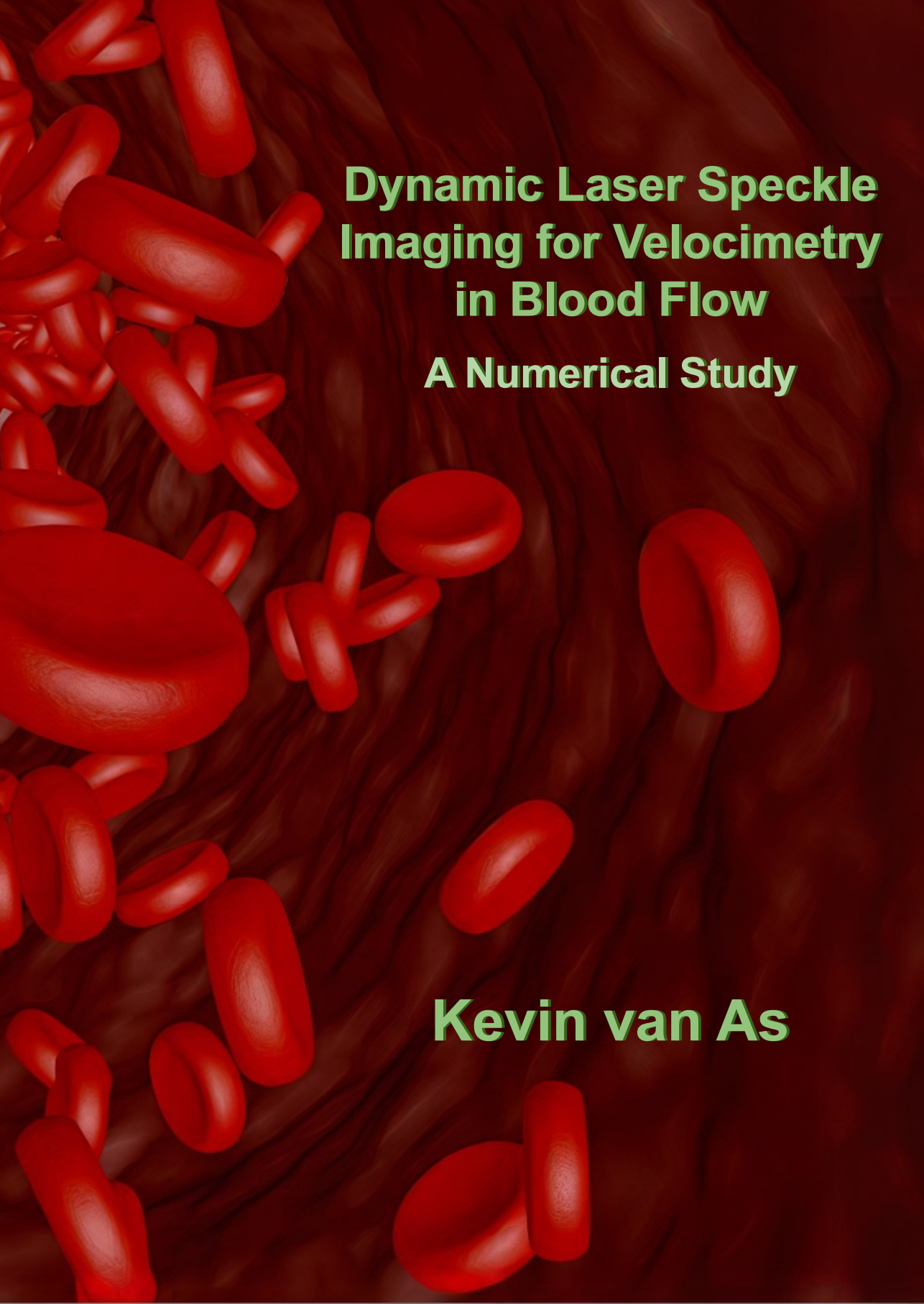
To cite this publication, please use the final published version (if applicable).
Please check the document version above.

Copyright

Other than for strictly personal use, it is not permitted to download, forward or distribute the text or part of it, without the consent of the author(s) and/or copyright holder(s), unless the work is under an open content license such as Creative Commons.

Takedown policy

Please contact us and provide details if you believe this document breaches copyrights.
We will remove access to the work immediately and investigate your claim.

A 3D digital illustration of a blood vessel. The vessel wall is a dark, textured brown. Inside, numerous red blood cells are shown in various orientations and positions, appearing to flow. The cells are bright red with a slight sheen, highlighting their biconcave disc shape. The overall scene is set against a dark, reddish-brown background.

**Dynamic Laser Speckle
Imaging for Velocimetry
in Blood Flow**

A Numerical Study

Kevin van As

DYNAMIC LASER SPECKLE IMAGING FOR VELOCIMETRY IN BLOOD FLOW

A NUMERICAL STUDY

DYNAMIC LASER SPECKLE IMAGING FOR VELOCIMETRY IN BLOOD FLOW

A NUMERICAL STUDY

Proefschrift

ter verkrijging van de graad van doctor
aan de Technische Universiteit Delft,
op gezag van de Rector Magnificus prof. dr. ir. T.H.J.J. van der Hagen
voorzitter van het College voor Promoties,
in het openbaar te verdedigen op
dinsdag 2 april 2024 om 10:00 uur

door

Kevin VAN AS

Ingenieur in de Technische Natuurkunde, Technische Universiteit Delft, Nederland
geboren te Alphen aan den Rijn, Nederland

Dit proefschrift is goedgekeurd door de promotoren.

Samenstelling promotiecommissie:

Rector Magnificus,	voorzitter
Prof. dr. S. Kenjereš, Dipl.-Ing.,	Technische Universiteit Delft, promotor
Prof. dr. ir. C.R. Kleijn,	Technische Universiteit Delft, promotor
Dr. N. Bhattacharya,	Technische Universiteit Delft, promotor

Onafhankelijke leden:

Prof. dr. J.M. Thijssen,	Technische Universiteit Delft
Prof. dr. B.H.W. Hendriks,	Technische Universiteit Delft
Prof. dr. ir. I.M. Vellekoop,	Universiteit Twente
Prof. dr. A.P. Mosk,	Universiteit Utrecht
Prof. dr. S. Stallinga,	Technische Universiteit Delft, reservelid



Nederlandse Organisatie voor Wetenschappelijk Onderzoek

Keywords: speckle imaging, light scattering, velocimetry, atherosclerosis

Printed by: Ridderprint, www.ridderprint.nl

Front & Back: K. van As, 3D designed in Blender. The image was subsequently tone and contrast enhanced, and upscaled using AI.

Copyright © 2024 by K. van As

ISBN 978-94-6483-916-6

An electronic copy of this dissertation is available at repository.tudelft.nl

*Whether you think you can,
or you think you can't
– you're right.*
– Henry Ford

*Tell me and I forget.
Teach me and I remember.
Involve me and I learn.*
– Benjamin Franklin

*If you can't explain it simply,
you don't understand it well enough.*
– Albert Einstein

*The more you know,
the more you realize you know nothing.*
– Socrates

CONTENTS

List of Figures	xi
List of Tables	xiii
Glossary	xv
Acronyms	xxv
Nomenclature	xxvii
Summary	xxxiii
Samenvatting	xxxv
Introduction	1
1 Theory	7
1.1 Mie theory	8
1.1.1 Maxwell's Equations and the Wave Equation	8
1.1.2 Derivation of the Scattered Field	9
1.1.3 Amplitude Scattering Matrix	13
1.1.4 Multiple Scatterers	14
1.2 Blood	16
1.2.1 Converting a volume distribution to a number distribution	17
1.2.2 The Navier-Stokes Equations and Rheology	19
1.3 Exact Solution to the Navier-Stokes Equations	19
1.3.1 Plug flow	20
1.3.2 Hagen-Poiseuille flow	20
1.3.3 Womersley flow	20
1.4 Lagrangian Particle Tracking (LPT)	21
2 Description of the algorithm/code	25
2.1 Optics	26
2.1.1 The Mie Algorithm	26
2.1.2 The Extended Algorithm (Camera, Multiscattering)	26
2.1.3 Memory Requirement of the Algorithm	29
2.1.4 Runtime complexity of the algorithm	30
2.1.5 Speedup by approximating the scattering matrix	31
2.1.6 Convergence of the Algorithm	33
2.1.7 Approximations and their Consequences	33

2.2	Fluids	37
2.2.1	Blood	37
2.2.2	Lagrangian Particle Tracking (LPT)	38
2.2.3	Numerically solving the Navier-Stokes Equations	40
2.2.4	Geometry / Mesh	41
2.3	Combined Physics	41
2.4	Summary	43
3	Optics Code Validation: the Fraunhofer Solution	47
3.1	Theory: the Fraunhofer Approximation	48
3.1.1	Solution 1: Rectangular Aperture.	49
3.1.2	Solution 2: Double Slit	49
3.1.3	Solution 3: Circular Aperture.	49
3.2	Methods	50
3.2.1	Geometry	50
3.2.2	Non-dimensionalization	50
3.2.3	Parameters.	51
3.3	Results	52
3.4	Conclusions.	54
4	Detecting a Heartbeat using Laser Speckle Imaging	57
4.1	Introduction	58
4.2	Approach	60
4.2.1	Speckle Imaging	60
4.2.2	Mie Theory.	62
4.2.3	Fluid Dynamics	62
4.2.4	Data Analysis	63
4.3	Code Description	64
4.3.1	Computational Fluid Dynamics (CFD)	64
4.3.2	Optics	64
4.4	Results	66
4.4.1	Convergence.	67
4.4.2	Extracting a Heartbeat	69
4.4.3	Future Work	71
4.5	Conclusions.	72
5	How Velocity affects the Speckle Contrast	77
5.1	Introduction	78
5.2	Simulation	78
5.2.1	Approach	78
5.2.2	Results.	80
5.3	Theoretical Comparison	82
5.3.1	Theory.	82
5.3.2	Results.	83
5.4	Conclusions.	86

6	Towards Detecting Atherosclerosis	89
6.1	Introduction	90
6.2	Generic Approach.	91
6.3	Computational Fluid Dynamics (CFD)	93
6.3.1	Approach	93
6.3.2	Results	95
6.4	Coupling fluids to optics	98
6.5	Speckle Imaging.	100
6.5.1	Approach: optics code description.	100
6.5.2	Approach: post-processing speckle	100
6.5.3	Results	102
6.6	Summary and Conclusions	105
7	Conclusions and Outlook	111
7.1	Conclusions, discussion and remaining questions	112
7.2	Outlook	117
A	Mie theory – the details	121
A.1	Why are terms omitted from the expansion?	121
A.1.1	Extract the Coefficients using Orthogonality	121
A.1.2	Find the Coefficients	123
A.2	Deriving the Mie coefficients	123
B	OptoFluids Code Implementation	125
B.1	Fluids	125
B.2	Optics.	126
B.2.1	Classes / Data structure	126
B.2.2	Pseudocode of the Algorithms	126
B.3	OptoFluids: combining the workflow	129
	Curriculum Vitae	135
	List of Publications	137

LIST OF FIGURES

1.1	Geometry of light scattering by an arbitrary particle	9
1.2	Definition of the scattering plane: orthogonal and parallel fields	14
1.3	Definition of \vec{z} : the displacement vector	15
1.4	Illustration of the initial phase	16
1.5	Shape of a Red Blood Cell	16
1.6	Radial hematocrit profile in a cylinder	17
1.7	Inversion of a Cumulative Probability Distribution	18
2.1	Cartoon of the multiscattering algorithm	27
2.2	Cartoon to illustrate the definition of the scattering order, p	28
2.3	How electric field data will be stored for multiscattering	29
2.4	Amplitude Scattering Matrix	32
2.5	Simulated particle density as a function of cylindrical radius	38
2.7	Cylindrical Mesh	41
2.9	Diagram - workflow of the combined fluids and optics codes	42
3.1	Diffraction Geometry	48
3.2	Scattering geometry for our validation study.	50
3.3	An interference pattern develops as distance is increased.	52
3.4	Validation results for the optics code I	53
3.5	Validation results for the optics code II	54
4.1	Sketch of Laser Speckle Imaging of an artery, and extracting a heartbeat	59
4.2	Illustration of temporal data sampling with short and large intervals	61
4.3	Some characteristic speckle figures	68
4.4	Convergence study: effect of spatial and temporal resolution	69
4.5	Results: speckle contrast time series and frequency spectra of a sinusoidally modulated flow	70
4.6	Results: speckle contrast time series and frequency spectra of a heartbeat-modulated flow	71
5.1	Sketch of Laser Speckle Imaging of a cylindrical artery	79
5.2	Results: speckle contrast against velocity and camera integration time	81
5.3	Results: master curve of the speckle contrast's dependency	81
5.4	Results: fit of theoretical models against our data, part 1	85
5.5	Results: fit of theoretical models against our data, part 2	85
6.1	Sketch of Laser Speckle Imaging of a stenosed artery, and our probing sites	92
6.2	Imposed flow rate at the arterial inlet: the 'heartbeat'	94

6.3	Results: flow profile contours in the artery at maximum inlet velocity . . .	95
6.4	Results: flow profile contours in the artery at average inlet velocity	96
6.5	Results: flow profile contours in the artery at minimum inlet velocity . . .	97
6.6	Results: cross-section of the flow profiles in the artery	98
6.7	Illustration of temporal data sampling with short and large intervals	99
6.8	Results: speckle contrast time series and frequency spectra in the stenosed artery at five different probing sites	103
7.1	Carotid artery with five sites.	115
B.1	Class UML of the MSFF code	126

LIST OF TABLES

2.1	Complexity of the Algorithm	30
3.1	Parameters used in the Fraunhofer validation I	51
3.2	Parameters used in the Fraunhofer validation II	52
4.1	Parameters used to study the effect of speckle boiling	67
5.1	Parameters used to fit the theoretical models to our simulation results	86
6.1	Parameters used in the fluid simulations	93
6.2	Parameters used for data acquisition	100
6.3	Parameters used in the optics simulations	101

GLOSSARY

- adapter interface** A 'good practice' code pattern, in which an interface is created through which two modules can interact with each other, without knowing each other's details.. 126
- Airy pattern** Pattern comprising concentric circles that appears in optical problems with circular apertures, see Sec. 3.1.3. 47
- amplitude scattering matrix** Matrix, as a function of the scattering angle, that upon multiplying the incoming field yields the scattered field. 13, 26, 62
- anisotropic** When properties are not the same in every direction. 122
- Ansys Fluent** Fluid dynamics (and related physical phenomena) modeling software by Ansys.. 93
- aperture** Hole through which light travels, diffracting the light. xv–xvii, xxi, xxvii, 48, 66, 83
- associated Legendre polynomial** A set of mathematical functions that are defined as the solution to the general Legendre differential equation. 10, 26
- atherosclerosis** Common blood condition – plaque may pile up inside your arteries, narrowing them and making them stiff, and risking big chunks of plaques to come loose at the same time, which could cause a blockage inside the artery (i.e., a stroke). xx, xxii, 1, 4, 72, 89–91, 105, 111, 114, 116
- autocovariance** Taking the covariance with a delayed version of itself. Used to determine how much time it takes for a signal to decorrelate over time.. xxvii, 82, 101
- backflow** Flow that locally moves downstream relative to the average cross-sectional velocity. 104
- backscattering** During multiscattering, the scattered wave of the first particle might scatter off of a second particle to then once again scatter off of the first particle. 29, 65, 78, 100
- Bessel function** A set of mathematical functions that are defined as the solution of the Helmholtz differential equation in cylindrical coordinates, which is the eigenvalue problem for the Laplace operator: $\nabla^2 f = -k^2 f$. xxviii, 49, 82, 122
- bifurcation** The region right before the fluid flow splits into two separate branches. 4, 92, 104, 115

- blood perfusion** Fluid flow through the tiny capillary networks in tissue; rate at which the blood is delivered to tissue in $[\text{m}^3/(\text{s} \cdot \text{kg})]$. 2, 71
- Brownian motion** At a molecular level, molecules drift around randomly due to random collisions with other molecules.. 82
- camera exposure time** Synonym for [camera integration time](#). xvi, 59, 78, 112
- camera integration time** A camera does not measure instantaneous data, but rather has its [aperture](#) opened for a certain time period, and then measures the average light that hit each pixel during that time, essentially measuring a blurred version of the instantaneous reality; synonym for [camera exposure time](#). xvi, xix, xxvii, xxix–xxxi, 61, 78, 99, 101, 102, 113, 131
- carotid artery** Major artery, starting as the [common carotid artery \(CCA\)](#) in the neck, and branching into the [internal carotid artery \(ICA\)](#) and [external carotid artery \(ECA\)](#) in the head. xvi, xxv, 2, 60, 79, 89–91, 105, 115
- circulation** Region in a fluid flow in which the fluid rotates along a closed curve. xxiv, 95, 104, 105
- coherent light** When light waves are spatially coherent (i.e., constant [polarisation](#)) and temporally coherent (i.e., constant frequency/wavelength and constant [phase](#)). 58, 78, 90, 91
- (computational) complexity** How the performance (i.e., runtime and/or memory requirement) of an algorithm scales with input problem size. 30, 65, 100
- conductivity** Measure of how well a material conducts a current when a voltage is applied to it. 8
- convergence** (of an algorithm) When the solution of the algorithm no longer changes as the number of iterations is increased, or as smaller spatial or temporal steps are taken, then the algorithm is said to converge (with a certain accuracy). 33, 68, 101, 118
- covariance** Measure of the strength of how two (or more) random variates correlate, e.g., a positive covariance means that when one variate is high, the other tends to be high as well.. xv, 82
- crest** Point where the amplitude of a periodic function is at its *maximum*. 70, 104
- cyclic boundary conditions** A [Boundary Condition \(BC\)](#) in which two opposite sides are set to equal values, e.g., what leaves one side re-enters at the opposite side. 64
- depolarisation** When light loses its [polarisation](#), i.e., when the fields start oscillating in multiple directions. 60, 101
- deviatoric stress** [Stress](#) minus the [hydrostatic pressure](#) to exclude its effect. 19

- diffraction** The spreading of light waves, e.g., due to it passing through a narrow [aperture](#) or it [scattering](#) off of a particle. [xv](#), [xxii](#), [8](#), [48](#), [61](#), [99](#)
- diffusive medium** A medium which strongly [diffuses](#) light. [xix](#), [xxii](#), [58](#)
- direct imaging** Capturing an image of an object directly, i.e., taking a photo; opposite: [indirect imaging](#). [xviii](#), [2](#), [58](#)
- double-slit experiment** In the double slit experiment, light is shone upon two long rectangular [apertures](#), after which the light waves [interfere](#) with themselves to form an interference pattern. [47](#)
- downstream** Further ahead in the flow, where the flow is going to, opposite of [downstream](#). [xv](#), [xvii](#), [102](#)
- downstream** The direction where the flow is originating from, opposite of [downstream](#). [xvii](#)
- electric susceptibility** Measure of polarization that a dielectric material obtains in response to an applied electric field. [8](#)
- flow rate** Volume of fluid flowing past a point per second. [xxx](#), [102](#)
- flow-through time** Characteristic time it takes a fluid parcel injected at the inlet to reach the outlet. [94](#)
- forward-scattering** [Scattering](#) with a [scattering angle](#) close to zero; when the scattered light moves (almost) in the same direction as the incoming light. [33](#)
- Fourier spectrum** Synonym of [frequency spectrum](#), named after the mathematician and physicist Joseph Fourier who set the foundations of frequency/Fourier analysis.. [99](#), [112](#), [131](#)
- Fraunhofer diffraction** Approximation of the [Fresnel diffraction](#) solution that is valid in the far-field. [47](#), [48](#)
- frequency mode** Periodic functions can be decomposed into a discrete set of frequencies, called ‘frequency modes’. The frequency with the highest amplitude (usually the first one) is the main mode, and subsequent frequencies are the higher-order modes which are at multiples of the main mode. See also: [frequency spectrum](#). [xvii](#), [57](#), [99](#), [102](#), [106](#)
- frequency signature** What the [frequency spectrum](#) looks like: if two frequency signatures are the same, the underlying signals must, too, be the same. [4](#), [105](#), [112](#), [115](#)
- frequency spectrum** Each function can be decomposed into the frequencies the function is made of. The frequency spectrum of a function shows the amplitudes of each frequency the function comprises, which could in general be a continuous spectrum of all frequencies, but periodic functions decompose into a discrete set of [frequency modes](#). [xvii](#), [xxii](#), [xxiv](#), [69](#), [91](#), [102](#)

- Fresnel diffraction** Approximation of the [Fresnel-Kirchhoff diffraction](#) solution that is valid near-axis. [xvii](#), [48](#)
- Fresnel-Kirchhoff diffraction** Exact solution to how a [monochromatic](#) spherical light wave propagates through space. [xviii](#)
- fringe** (Alternating) light and dark bands in the [intensity](#) pattern of light, often caused by [interference](#). [50](#), [68](#), [101](#)
- fully-developed speckle** [Speckle \(pattern\)](#) that originates from light waves with the [phases](#) uniformly distributed over $[0, 2\pi]$ radians. [60](#), [80](#)
- hematocrit** Volume fraction of [Red Blood Cells \(RBCs\)](#) present in blood. [16](#), [34](#), [65](#)
- hematology** The study of blood and blood disorders. [1](#), [33](#)
- Huygens-Fresnel principle** Principle saying that each point of a [wavefront](#) of sound/light can be treated as a point-source that sound/light originates from, expanding into every direction; derived from the [Fresnel-Kirchhoff diffraction](#) formula. [48](#)
- hydrostatic pressure** [Pressure](#) in a material caused by its own weight pressing downwards on itself (ρgH) and using the atmospheric pressure (P_{atm}) as a baseline: $P = \rho gH + P_{\text{atm}}$. [xvi](#)
- in-vitro** Within glass; a study that is not [in-vivo](#), but rather in a controlled test environment such as in a petri dish. [xviii](#), [xx](#)
- in-vivo** Within a living organism, as opposed to [in-vitro](#). [xviii](#), [1](#), [25](#), [58](#), [89](#), [90](#), [106](#), [111](#), [118](#)
- incompressible flow** Flow of a fluid whose volume (and thus density, also) does not change with pressure; a fluid that cannot be compressed. [19](#), [41](#), [93](#)
- indirect imaging** Creating an image of an object through indirect means, e.g., measuring the [scattered](#) light coming off of the object, which yields an image containing information about the object, but is not a photo of the object; opposite: [direct imaging](#). [xvii](#), [2](#), [72](#), [113](#)
- intensity** Measure for the brightness of light, i.e., of an electromagnetic field. It is computed by squaring the fields. [xviii](#), [xxviii](#), [xxx](#), [26](#), [47](#), [60](#), [78](#)
- interference** When waves interfere, they superimpose, often strengthening each other in some locations, while cancelling each other out in other locations. [xvii](#), [xviii](#), [26](#), [47](#), [58](#), [78](#), [90](#), [91](#)
- interparticle distance** Distance between two particles i and j , \vec{r}_{ji} . [xxx](#), [30](#), [47](#), [65](#), [79](#), [90](#)
- interpolation** To approximate the output of a function at a certain input parameter by using known function values at the two (or more) nearest input parameters. [31](#)

- Lagrangian particle tracking** A method of computing the trajectory of a particle based on all (fluid) forces acting on the particle, see Sec. 2.2.2. xxv, 21, 37, 64
- laminar** ‘Neat’ flow in which fluid particles follow smooth layered paths (i.e., streamlines). Opposite: **turbulent** flow. xxi, xxiii, 19
- laser speckle contrast imaging** **Laser speckle imaging**, but using the **speckle contrast** as a metric to study the scattering medium. xxv, 3, 58, 78, 89, 90, 105, 112, 117
- laser speckle imaging** When a **diffusive medium** is illuminated by a laser, the diffracted light will form a **speckle pattern**, containing information about the scattering medium, see Fig. 4.1. xix, xxv, 2, 26, 57, 72, 77, 119, 131
- Maxwell equations** Maxwell derived four equations, which are the governing equations of light. Or, more generally: of electromagnetic fields. 8
- microstepping** Our process of mimicking the finite **camera integration time** by performing optics simulations in rapid succession, and then averaging the result. We repeat this for each timestep at which we gather data. See Sec. 6.4. 99, 130, 131
- Mie theory** Exact solution to the **scattering** of light by a single spherical particle, as derived by Gustav Mie in 1908. xxiii, 9, 25, 31, 59, 78, 91, 111, 121
- monochromatic** Comprising a single color; comprising a single wavelength. xviii, 91, 100
- Monte Carlo method** Mathematical method that uses repeated random sampling of a chance process to estimate quantities of interest using statistical analysis. 58, 90
- morphology** The study of the form, shape and structure of (parts of) organisms. 33, 72
- multiscattering** When light **scatters** not only from each **scatterer** (i.e., ‘initial scattering’), but the scattered light too scatters from each scatterer recursively, see Fig. 2.1. xv, xxi, xxv, 2, 26, 57, 59, 78, 91, 98, 100, 111
- Navier-Stokes equations** A set of equations for conservation of mass and momentum, which govern the behaviour of fluids. 19, 40, 64, 93
- Newton’s binomial theorem** Theorem on how to expand $(a + b)^n$ in each individual component. This also works when taking the n ’th derivative of a function which has the form of the product of two functions: $f(x) = g(x)h(x)$. 34
- non-invasive** Without affecting the thing being measurement, e.g., a measurement on a patient without a need to use a needle or cut the patient open. 1, 58, 78, 90, 111
- non-Newtonian fluid** A fluid with a different **rheology** than Newton’s law of viscosity, which says that viscosity is independent of **stress**. Examples are: toothpaste, custard, shampoo and blood. 16, 37, 94, 112

- numerical experiment** Experiment conducted using a computer simulation, as opposed to a physical experiment that is often performed in a laboratory setup. [3](#), [111](#)
- Nyquist criterion** To prevent a loss of information when discretely measuring a signal, the sampling frequency should be at least double the highest frequency contained in the signal.. [80](#)
- objective speckle** [Speckle \(pattern\)](#) that forms without passing through any kind of imaging system, such as lenses.. [79](#)
- OpenFOAM** (Open-source Field Operation And Manipulation) A free open-source computational fluid mechanics code developed by OpenCFD Ltd. and the community.. [37](#), [93](#)
- orthogonality** Two vectors or two functions are said to be orthogonal if their inner product equals zero. The inner product of two functions is defined as the integral of the product of the two functions over a predefined relevant length scale. [xx](#), [11](#), [122](#)
- orthonormal** Two vectors are orthonormal if they are [orthogonal](#) and have a length equal to one. [48](#)
- particle image velocimetry** Experimental method for [velocimetry](#), in which the fluid is seeded with tracer particles. If these particles are sufficiently small, they will follow the streamlines of the fluid. By illuminating the fluid, the motion of these particles can be tracked over time (i.e., recording a video), and the velocity field can be computed for each frame.. [xxv](#), [2](#), [78](#), [91](#), [113](#)
- peripheral vascular disease** Disease in which blood circulation becomes limited (in certain parts of the body), reducing the availability of oxygen and nutrients; most commonly caused by [atherosclerosis](#). [2](#)
- permeability** Measure of magnetization that a material obtains in response to an applied magnetic field. [8](#), [62](#)
- permittivity** Measure of electric polarizability of a dielectric material. [8](#)
- phantom** (in fluid dynamics) Model used for [in-vitro](#) studying a flow, e.g., a transparent hollow artery made of an index-matched plastic. [60](#)
- phase** Waves have a phase which describes the point in the oscillation the wave is at. Specifically, the ‘initial phase’ determines the starting point of the wave, e.g., ϕ_0 in: $\cos((kz - \omega t) + \phi_0)$. [xvi](#), [xviii](#), [xxiv](#), [14](#), [16](#), [35](#), [60](#), [91](#)
- plane wave** A wave that stretches infinitely in two dimensions, i.e., a plane, while propagating in the third dimension. [xxv](#), [xxvi](#), [9](#), [14–16](#), [25–27](#), [48](#), [59](#), [78](#), [91](#), [100](#)
- plaque (arterial)** Sticky substance that piles up inside arteries, consisting of cholesterol, waste products, calcium and fibrin; see also: [atherosclerosis](#). [xv](#), [4](#), [90](#), [114](#)
- plug flow** Flow with a constant velocity, see Eq. (1.56). [20](#), [60](#), [79](#), [104](#), [112](#)

- Poiseuille flow** Exact static flow profile in a cylindrical geometry, see Eq. (1.58). 20, 62, 93, 104, 112
- polarisation** The direction in which (the electric field of) a transverse wave oscillates, which is orthogonal to the propagation direction. xvi, 11
- pressure** Force per unit area. xviii
- pulsatile flow** Flow with a periodic temporal dependency. xxiv, 61
- real-time** When dynamic results can be seen immediately, the results are available “in real-time”, as opposed to requiring processing first.. 1, 111
- reflection (diffuse)** When light hits a rough medium, it scatters in all directions, i.e., it *diffuses*. xvii, 60
- reflection (specular)** When light scatters off of a smooth surface (e.g., a mirror), the light ray is reflected by the law which states that ‘the angle of incidence equals the angle of reflection’. 60
- refraction** The redirection of a light ray as it passes from one medium into the next. xii
- refractive index** Dimensionless number that is a property of a medium, which is a measure for the [refraction](#) of light. 8, 26, 71, 80, 94, 119
- Reynolds number** Non-dimensional number in fluid mechanics equal to the ratio of inertia-dominated and viscous-dominated forces. At a sufficiently high Reynolds number, the fluid becomes [turbulent](#) as opposed to being [laminar](#) at low Reynolds numbers. 19, 39
- rheology** The study of how a fluid’s [viscosity](#) depends on the [strain rate](#) in the fluid. xix, 16, 37
- Ricatti-Bessel function** A set of mathematical functions that appear in some problems involving the solution of a spherical differential equation. They are related to the [spherical Bessel functions](#) of the first and the second kind: $\psi_n(\rho) \equiv \rho j_n(\rho)$ and $\xi_n(\rho) \equiv \rho h_n^{(1)}(\rho)$. 8, 12, 123
- scatterer** A particle that we use to [scatter](#) light. xix, xxii, 4, 9, 25, 26, 47, 58, 60, 90, 112, 113
- scattering** When a wave scatters, it diverts from its original straight path, e.g., by being disturbed by a particle or an [aperture](#). xvii–xix, xxi, xxiii, 2, 9, 58, 78, 100
- scattering angle** Angle in the [scattering plane](#) between the scattered wave and the incoming wave, see Fig. 1.2. xv, xvii, 13, 26, 48, 62
- scattering order** In our optics code, we implemented [multiscattering](#) iteratively. The scattering order is the number of times the wave has scattered by the scatterers thus far, see Fig. 2.2. 26, 78, 100

- scattering plane** Plane spanned by the propagation vectors of the incoming and the scattered field, see Fig. 1.2. [xxi](#), [13](#)
- sclerosed** Affected by (athero)sclerosis. [4](#), [92](#), [111](#)
- signal-to-noise ratio** Ratio of the strength/amplitude of the signal (i.e., the information) to the amplitude of the noise present in the measurement. [91](#), [105](#)
- size parameter** Dimensionless number that gives the size of a particle in terms of the light's wavelength, see above Eq. (1.28). [12](#), [26](#)
- speckle (pattern)** Spot-like random intensity pattern that forms due to interference after light [diffracts](#) from a [diffusive medium](#), e.g., see Fig. 4.3a. [xviii–xx](#), [xxii](#), [xxiii](#), [xxvii](#), [xxxi](#), [2](#), [42](#), [57](#), [58](#), [72](#), [78](#), [89](#), [90](#), [92](#), [100](#), [112](#)
- speckle boiling** When speckles randomly appear and disappear in a [speckle pattern](#), e.g., as a result of [scatterers](#) moving relative to each other or in-/outside of the imaging plane, it looks like the top of a pan of boiling water; hence 'speckle boiling'. [2](#), [4](#), [57](#), [58](#), [80](#), [90](#), [101](#), [104](#), [112](#), [118](#)
- speckle contrast** Measure for the contrast in a [speckle](#) image: ratio between the standard deviation and the mean intensity, see Eq. (4.1). [xix](#), [xxvii](#), [xxviii](#), [3](#), [60](#), [77](#), [80](#), [91](#), [100](#), [102](#), [105](#), [112](#), [117](#), [131](#)
- speckle decorrelation time** Characteristic timescale upon which the auto-correlation of a [speckle pattern](#) drops below a certain threshold (typically $1/e$). [xxx](#), [59](#), [77](#), [113](#)
- translating speckle** When [scatterers](#) move in the imaging plane, each with the same velocity, then [speckle pattern](#) simply moves along with the same velocity. [2](#), [58](#), [84](#), [90](#), [118](#)
- spectral analysis** Analyzing a signal by using the [frequency spectrum](#). [106](#)
- spectral noise** Noise in the [frequency spectrum](#). [71](#)
- spherical Bessel function** A set of mathematical functions that are defined as the solution of the Helmholtz differential equation in spherical coordinates, which is the eigenvalue problem for the Laplace operator: $\nabla^2 f = -k^2 f$. [xxi](#), [xxii](#), [xxviii](#), [xxxi](#), [10](#), [26](#), [62](#)
- spherical Hankel function** The spherical Hankel function of the first/second kind is a different name for the [spherical Bessel function](#) of the third/fourth kind, respectively. [12](#), [26](#)
- stagnation point** Point in a fluid flow at which the local velocity is zero. [95](#)
- statistical noise** When a data set is not infinite, there will be random fluctuations in a measured value around its true value, introducing a statistical error (noise) to the measurement. [63](#)
- steady state** Not changing as time advances; independent of time. [41](#)

stenosis An abnormal narrowing of an artery, limiting or obstructing blood flow. 1, 4, 89, 90, 104, 105, 115

Stokes number Non-dimensional number in fluid mechanics equal to the ratio of the characteristic time of a particle relative to the characteristic time of the flow. If the Stokes number is $\ll 1$, the particles respond immediately to any changes in the flow, which makes the particles behave as simple tracer particles that follow the flow's streamlines precisely. 39

strain Measure for the deformation of a material, including fluids. xxiii

strain rate The change of **strain** over time; derivative of strain with respect to time. xxi, 19

stress Force per unit area inside a material, including fluids. xvi, xix, 19

subjective speckle **Speckle (pattern)** that forms after being imaged with an imaging system, such as lenses.. 79

T-matrix method Computational technique to compute light **scattering** by non-spherical particles; think of it like a more generic – though more computationally expensive – **Mie method**. 33, 66, 100

Taylor expansion In a Taylor expansion, a function is approximated at $f(x)$ by taking the value at x_0 being nearby x , and estimating how to get from $f(x_0)$ to $f(x)$ by considering the function's derivatives up to a certain order. 34

trough Point where the amplitude of a periodic function is at its *minimum*. 70, 104

turbid medium A medium which both strongly absorbs and **scatters** light. 2, 57, 58, 86, 90

turbulence Flow with chaotic fluctuations in its pressure and velocity, resulting in eddies/vortices and a heavy time-dependent flow. Opposite: **laminar flow**. xix, xxi, 19

under-relaxation In an algorithm, the required change of a variable can be computed, as opposed to the new value. With under-relaxation you do not update the variable's value by the full change, but only a fraction of the change, to slow down strong non-linear fluctuations in the solution. 41

underresolved Imaging (the details of) an object requires a sufficient number of pixels; underresolving is when too few pixels are used – the details of the object are then lost, or in the most extreme case the object is smaller than one pixel. 63

velocimetry Measuring the velocity of a fluid. xx, xxvii, 1, 4, 78, 90

viscosity Measure of the resistance of a fluid to deformation. xxi, 16, 19

vortex A [circulation](#) in a flow. [104](#)

vorticity A measure of the local spinning motion in a flow field, mathematically equal to the curl of the flow velocity vector.. [118](#)

wave number Spatial frequency of a wave, $k = 2\pi/\lambda$. [8](#), [62](#)

wavefront Surface over which the [phase](#) of a wave is constant, at a specific time. [xviii](#)

white noise A noisy signal with a statistically uniform [frequency spectrum](#). [91](#)

windowing To subdivide an image into smaller parts, see the paragraph above Eq. (4.6). [63](#), [101](#), [112](#)

Womersley flow Exact flow profile for time-dependent flow in a cylindrical geometry, see Eq. (1.59). [20](#)

Womersley number Non-dimensional number in (bio)fluid mechanics for [pulsatile flow](#), representing the ratio between pulsatile flow frequency terms to the viscous effects. [20](#)

ACRONYMS

- BC** Boundary Condition. [xvi](#), [9](#), [12](#), [69](#), [70](#), [80](#), [84](#), [122](#), [123](#)
- CCA** common [carotid artery](#). [xvi](#)
- CFD** Computational Fluid Dynamics. [4](#), [20](#), [25](#), [41](#), [42](#), [60](#), [64](#), [78](#), [91–93](#), [98](#), [99](#), [105](#), [111](#), [115](#), [125](#), [130](#)
- ECA** external [carotid artery](#). [xvi](#), [60](#), [79](#), [92](#), [95](#), [97](#), [104](#), [105](#)
- FF** Far-Field. [13](#), [26](#), [27](#), [33–36](#), [48](#), [49](#), [51](#), [53](#), [54](#), [62](#), [64–66](#), [72](#), [78](#), [79](#)
- I/O** Input & Output. [27](#), [126](#)
- ICA** internal [carotid artery](#). [xvi](#), [91](#), [92](#), [95–97](#), [104](#), [105](#)
- IPW** Incoming Plane Wave. [14–16](#), [27–29](#), [34](#), [48](#), *Glossary: [plane wave](#)*
- LPT** Lagrangian Particle Tracking. [21](#), [38](#), [93](#), *Glossary: [Lagrangian particle tracking](#)*
- LSCI** Laser Speckle Contrast Imaging. [xxvii](#), [3](#), [4](#), [58](#), [78](#), [79](#), [89–92](#), [98](#), [99](#), [105](#), [106](#), [112–119](#), *Glossary: [laser speckle contrast imaging](#)*
- LSI** Laser Speckle Imaging. [2](#), [3](#), [26](#), [41](#), [57](#), [59–61](#), [69](#), [71](#), [72](#), [77](#), [86](#), [97](#), [119](#), [131](#), *Glossary: [laser speckle imaging](#)*
- MRA** Magnetic Resonance Angiography. [1](#), [90](#)
- MRI** Magnetic Resonance Imaging. [1](#), [115](#), [116](#)
- MSFF** Multi-Scattering Far-Field. [26](#), [54](#), [126](#), *Glossary: [multiscattering](#)*
- NF** Near-Field. [27](#)
- OOP** Object-Oriented Programming. [29](#), [126](#)
- PIV** Particle Image Velocimetry. [2](#), [78](#), [91](#), [93](#), [94](#), [96](#), [97](#), [113](#), *Glossary: [particle image velocimetry](#)*
- PPG** Photoplethysmography. [2](#), [4](#), [111](#)
- PSF** point-spread function. [66](#)

PW Plane Wave. 9, 11, 26–28, 34, 35, 50, 59, 61, 62, 64, 65, 72, 129, *Glossary*: [plane wave](#)

RAM Random Access Memory. 28, 30, 33

RBC Red Blood Cell. xviii, 16, 25, 33, 34, 37, 38, 59, 60, 65, 71, 72

SSFF Single-Scattering Far-Field. 26, 52–54

VSH Vector Spherical Harmonic. 10–13, 62, 121–123

NOMENCLATURE

- a [m¹] Spherical particle radius, page 10
- α [-] Dimensionless number: Womersley; Represents the ratio between transient inertial force and viscous force, page 20
- a_n [-] Mie coefficient for the even term of the scattered field, page 12
- β [-] Correction factor for the loss of correlation caused by the ratio of pixel size to [speckle \(pattern\)](#) speckle size, page 82
- b_n [-] Mie coefficient for the odd term of the scattered field, page 12
- C [-] Depending on the author, the [speckle contrast](#) is denoted as either C or K . In this thesis I'll use K , page 60
- c [m¹s⁻¹] Speed of light in vacuum, page 8
- χ [-] Electric susceptibility, page 8
- c_n [-] Mie coefficient for the odd term of the internal field, page 11
- c_{rohs} [-] Constant defining the 'region of high-sensitivity' for performing [velocimetry](#) using [LSCI](#), page 114
- $C_t^{(2)}(\tau)$ [-] [Autocovariance](#) of temporal ([speckle](#)) fluctuations, page 82
- D [m¹] Characteristic length scale, page 19
- D [m¹] [Aperture](#) diameter, page 66
- d [m¹] Physical distance particles have travelled during one [camera integration time](#), page 80
- d_n [-] Mie coefficient for the even term of the internal field, page 11
- d_{speckle} [m¹] Width of a typical [speckle](#), page 66
- \vec{E} [Vm⁻¹ = NC⁻¹ = m¹kg¹s⁻³A⁻¹] Electric field, page 8
- E_0 Electric field - magnitude when using complex notation, page 11
- \vec{E}_1 Electric field - inside the scatterer, page 10
- \vec{E}_2 Electric field - total outside the scatterer, page 9
- \vec{E}_i Electric field - incident, page 9

$e^{-i\omega t}$	This thesis uses the minus sign convention in the complex wave notation, page 8
ϵ	$[\text{m}^{-3}\text{kg}^{-1}\text{s}^4\text{A}^2]$ Complex (electric) permittivity, page 8
ϵ_0	$[\text{m}^{-3}\text{kg}^{-1}\text{s}^4\text{A}^2]$ (Electric) permittivity of vacuum, page 8
\vec{E}_s	Electric field - scattered, page 9
f	$[\text{s}^{-1}]$ Frequency, page 62
f_i^{ext}	$[\text{Nm}^{-1} = \text{kg}^1\text{s}^{-2}]$ External force per unit length, page 19
f_s	$[\text{s}^{-1}]$ Data sampling frequency, page 99
$F(t)$	$[-]$ Time-dependent modulation function, page 62
\vec{H}	$[\text{m}^{-1}\text{A}^1]$ Magnetic field, page 8
H	$[\text{m}^1]$ Characteristic length scale (thickness), page 38
$h_n^{(1)}$	$[-]$ Spherical Bessel function of the third kind (or Hankel function of the first kind) and of order n , page 12
I	$[\text{Wm}^{-2} = \text{kg}^1\text{s}^{-3}]$ Intensity , page 29
J_n	$[-]$ Bessel function of the first kind and of order n , page 49
j_n	$[-]$ Spherical Bessel function of the first kind and of order n , page 11
K	$[-]$ Speckle contrast , page 60
k	$[\text{m}^{-1}]$ Wave number, $\frac{2\pi}{\lambda}$, page 8
k_0	$[\text{m}^{-1}]$ Wave number in vacuum, $\frac{2\pi}{\lambda_0}$, page 8
κ	$[-]$ $n\kappa$ is the complex part of the complex refractive index, page 8
L	$[\text{m}^1]$ Characteristic length scale (length), page 38
L	$[\text{m}^1]$ Length of cylinder, page 17
L	$[\text{m}^1]$ Orthogonal distance between the center of the aperture and the camera; Used only in Chap. 3., page 51
λ	$[\text{m}^1]$ Wavelength, page 8
\vec{M}	$[-]$ Vector Spherical harmonic 1, page 10
M	$[-]$ Number of pixels of the camera, page 30
M	$[-]$ Total number of pixels of the camera, page 65
m	Sum index for the azimuthal term (Mie theory), page 10
m	$[-]$ Relative refractive index $\frac{N_1}{N_2}$, page 12

- m [kg¹] Mass, page 38
- $M_{x/y}$ [-] Number of pixels in the x/y -direction of the camera, page 64
- μ [-] Short for $\cos\theta$, page 13
- μ [NA⁻² = m¹kg¹s⁻²A⁻²] (Magnetic) permeability, page 8
- μ [Pa · s = m⁻¹kg¹s⁻¹] (Dynamic) viscosity, page 19
- μ_0 [NA⁻² = m¹kg¹s⁻²A⁻²] (Magnetic) permeability of vacuum, page 8
- $n_{s,int}$ [-] Number of samples used to sample the [camera integration time](#), see Fig. 4.2, page 61
- \vec{N} [-] Vector Spherical harmonic 2, page 10
- N [-] Complex refractive index, page 8
- N [-] Number of particles, page 17
- n Sum index for the radial term (Mie theory), page 10
- n [-] Real refractive index, page 8
- n_C Cut-off index of the infinite Mie sum, page 26
- \hat{n} [-] Unit normal vector to some surface, page 10
- ν [m²s⁻¹] Kinematic viscosity, page 19
- ω [s⁻¹] Angular frequency, page 8
- P [Pa = m⁻¹kg¹s⁻²] Pressure, page 19
- p [-] Scattering order; The number of particles the light scattered upon before hitting the camera., page 27
- $\Delta\varphi$ [rad] Phase difference, page 27
- φ [rad] Azimuthal cylindrical angle, page 14
- φ [rad] Azimuthal spherical angle, page 10
- ϕ [-] Volume fraction; Hematocrit, page 17
- π_n [-] Short for $\frac{P_n^1(\cos\theta)}{\sin\theta}$, page 13
- P_n^m [-] Associated Legendre polynomial, page 10
- $P(r)$ [-] Probability density function with argument r , page 17
- $P(r \leq R_1)$ [-] Cumulative probability density function with argument R_1 and parameter r , page 18

ψ_n	[–] Ricatti-Bessel function of the first kind and of order n , page 12
Q	[m ³ s ⁻¹] Flow rate , page 102
\vec{r}	[m ¹] Position vector $x\hat{x} + y\hat{y} + z\hat{z}$, page 15
R	[m] Radius of a cylinder, page 19
r	[m ¹] Radial cylindrical coordinate (context: fluid dynamics), page 17
r	[m ¹] Radial spherical coordinate, page 10
\vec{r}_{ji}	[m ¹] Distance between particles j and i , page 30
r	[m ¹] Magnitude of displacement vector (interparticle distance), page 15
\vec{r}	[m ¹] Displacement vector, page 15
Re	[–] Dimensionless number: Reynolds; Represents the ratio of inertial forces and viscous forces, page 19
ρ	[–] Short for kr , page 10
ρ	[m ⁻³ kg ¹] Mass density, page 19
[S]	[–] Amplitude Scattering Matrix, page 13
s	[m ¹] Radial cylindrical coordinate (for Mie theory), page 14
S_1	[–] Amplitude Scattering Matrix Element related to E_{\perp} , page 13
S_2	[–] Amplitude Scattering Matrix Element related to E_{\parallel} , page 13
σ	[m ⁻³ kg ⁻¹ s ³ A ²] Conductivity, page 8
σ_I	[Wm ⁻² = kg ¹ s ⁻³] Standard deviation of intensity , page 60
σ_{ji}	[m ⁻¹ kg ¹ s ⁻²] Deviatoric stress tensor, page 19
St	[–] Dimensionless number: Stokes; Represents the ratio of the particle response time and the characteristic fluid timescale, page 39
Δt_{int}	[s ¹] Timestep used to sample the camera integration time , see Fig. 4.2, page 61
Δt	[s ¹] Time interval, page 61
T	[s ¹] Total simulation time, page 67
t	[s ¹] Time, page 8
τ	[s ¹] Characteristic timescale, page 38
τ_c	[s ¹] Speckle decorrelation time , page 59

τ_n	[-] Short for $\frac{dP_n^1(\cos\theta)}{d\theta}$, page 13
θ	[rad] Zenith spherical angle, page 10
θ_s	[rad] Scattering angle from Mie theory, page 13
t_{int}	[s ¹] Camera integration time , page 59
U	[m ¹ s ⁻¹] Characteristic velocity scale of the fluid, page 19
u	Uniformly generated random number, page 18
u	[m ¹ s ⁻¹] Velocity, page 19
u_i	[m ¹ s ⁻¹] i 'th component of the velocity vector, page 19
V	[m ¹ s ⁻¹] Characteristic velocity scale of the particle, page 38
V	[m ³] Volume, page 17
$v(r)$	[m ¹ s ⁻¹] Radial-dependency of the velocity, $u(r, t)$, page 62
w_{speckle}	[m ¹] Characteristic length scale for the speckle size, page 83
x	[-] (Optics) Size parameter = $k_2 a$, page 12
x_i	[m ¹] i 'th component of the position vector, page 19
ξ_n	[-] Ricatti-Bessel function of the third kind and of order n , page 12
y	[-] (Optics) Size parameter times relative refractive index = $k_1 a = mx$, page 12
z	[m ¹] Distance between the object and the image plane, page 66
z	[m ¹] Height cylindrical coordinate, page 14
z_n	[-] Any kind of spherical Bessel function of order n , page 10
$z_n^{(1)}$	[-] Spherical Bessel function of the first kind and of order n , page 11
$z_n^{(3)}$	[-] Spherical Bessel function of the third kind and of order n , page 12
$\langle Y \rangle$	These brackets denote the mean of some quantity Y , page 19
Y_1	The subscript '1' refers to some quantity Y inside the scatterer, page 9
Y_2	The subscript '2' refers to some quantity Y outside the scatterer, page 9
Y_e	The subscript 'e' refers to 'even', page 10
Y_f	The subscript 'f' refers to 'fluid', page 21
Y_o	The subscript 'o' refers to 'odd', page 10
Y_p	The subscript 'p' refers to 'particle', page 21

SUMMARY

Cardiovascular diseases are one of the leading causes of death worldwide, for example by causing strokes. Timely diagnosis of such diseases is pivotal for a patient's chance of survival. Furthermore, in the present world in which medical expenses are going through the roof, we can save greatly on costs if certain diseases are detected in an earlier stage. To that end, our research is focused on improving medical measurement techniques, to give doctors a greater arsenal to combat these diseases.

Ideally, a measurement technique is cheap, accurate, and all while causing minimal discomfort to the patient. Light-based techniques have proven previously to have great potential to fulfil that role. For example, that tiny device that you can put on your finger, and similarly the sensor in a sports watch, are able to measure your heart rate using light.

For our research we have developed a computer model, such that we can use the power of modern computing. Our model is able to predict how light is reflected by red blood cells flowing through an artery. The computer is then able to rapidly simulate many scenarios, producing a lot of data about what the reflected light looks like for each scenario. From that data, we are able to say something about what a certain pattern in the reflected light says about the underlying system: the flowing red blood cells.

As a first step, we have used our model to figure out how we can determine the heart rate from the reflected light. You could argue that that's nothing special, as your sports watch can already do precisely that, but it's an important step nonetheless, since our technique is different than what your sports watch is doing. Namely, the data our technique provides is more complex, but as a consequence also contains much more information and thereby yields a greater potential if we just become able to extract that information from the data.

Therefore, our second step was to determine the exact velocity of the red blood cells from the reflected light, which is quite of a magical thing when you think about it: even though we cannot 'see' the red blood cells directly, we can still 'see' how fast they are moving. Although we succeeded in determining the velocity, in reality a doctor will likely need to do some tweaking to account for patient-specific factors, such as skin tone.

Finally, we studied the disease atherosclerosis, in which accumulating cholesterol causes arteries to become more narrow, which ultimately could lead to a stroke. The narrowing of an artery, alters the flow behavior of the red blood cells, which we were able to pick up by studying changing patterns in the reflected light from our simulations. By extension, it should be possible to use reflected light to detect atherosclerosis, rapidly and cheaply flagging patients who are at risk.

We have shown the potential of reflected light techniques for medical diagnosis purposes. Although further research and work is still required to put these techniques into practice for doctor's to use, we have set the groundwork to enable these techniques in the not-too-distant future.

SAMENVATTING

Hart- en vaatziekten, zoals een hartinfarct, behoren tot de grootste doodsoorzaken wereldwijd. Wanneer deze ziekten ruim op tijd gediagnosticeerd worden, dan neemt de overlevingskans van patiënten sterk toe. Bovendien kunnen we de hoge medische kosten van dure therapieën terugbrengen door ziekten eerder te detecteren. Om dat te bereiken, onderzoeken wij hoe we medische meettechnieken kunnen verbeteren, zodat dokters een groter arsenaal hebben om hart- en vaatziekten te bestrijden.

De ideale meettechniek is goedkoop, accuraat, en zo comfortabel mogelijk voor de patiënt. Uitermate geschikt daarvoor zijn technieken die licht gebruiken. Neem bijvoorbeeld dat kleine apparaatje dat je op je vinger plaatst, of de sensor in een sporthorloge: je meet je hartslag met behulp van licht(absorptie).

Wij hebben voor ons onderzoek een computermodel ontwikkeld die in staat is om te berekenen hoe licht wordt weerkaatst door rode bloedcellen die door aderen stromen. Het grote voordeel van zo'n computermodel, is dat de computer zeer snel veel verschillende situaties kan simuleren. In de gegenereerde data zitten patronen. Ons doel is om uit die patronen informatie te halen over het onderliggende systeem – de stromende rode bloedcellen – en daarmee een nieuwe medische meettechniek te ontwikkelen.

Als eerste stap hebben wij ons computermodel gebruikt om te bepalen hoe je een hartslag kunt meten met behulp van weerkaatst licht. Dit klinkt waarschijnlijk als niets bijzonders – want jouw sporthorloge kan dat natuurlijk ook al – maar toch is het een hele belangrijke stap. Onze meettechniek is namelijk anders, en gebruikt weerkaatst licht om veel complexere data te produceren. Het grote voordeel is dat in die complexe data veel meer informatie verstopt zit. Als wij die informatie eruit weten te halen, dan kunnen wij meer dingen van het bloed meten.

Daarom was onze tweede stap om iets met onze meettechniek te doen wat een sporthorloge niet kan: kunnen we de snelheid van de stromende rode bloedcellen meten? Dit is best magisch eigenlijk: ook al kunnen wij de rode bloedcellen niet direct 'zien', kunnen we toch 'zien' hoe snel ze gaan! Het is ons gelukt om deze snelheid te meten; echter, in de praktijk zal een dokter met wat instellingen moeten spelen om goed te kunnen meten: patiënt-afhankelijke factoren zoals huidskleur beïnvloeden namelijk het resultaat.

Onze laatste stap was om de ziekte atherosclerose te bestuderen, oftewel aderverkalking: het dichtslibben van de aderen door een ophoping van cholesterol. Een vernauwde ader beïnvloedt het gedrag van de stromende rode bloedcellen, wat tot karakteristieke patronen in het weerkaatste licht zal leiden. Als we deze patronen omkeren, kunnen wij met onze meettechniek vernauwde aders detecteren. Doordat onze meettechniek snel en goedkoop is, kunnen risicopatiënten tijdig gesignaleerd worden.

We hebben met dit onderzoek de grote potentie van het gebruiken van weerkaatst licht als medische meettechniek gedemonstreerd. Alhoewel eerst meer onderzoek nodig is voordat deze techniek in de praktijk ingezet kan worden, hebben we met ons onderzoek een stevige basis gelegd om dit in de nabije toekomst mogelijk te maken.

INTRODUCTION

BLOOD IS PIVOTAL

Blood is of pivotal importance to many living beings, including us, as humans. Through our red blood cells, blood energizes organs by supplying oxygen. Through our white blood cells, blood is the vessel of the immune system to cure us from diseases. And through our platelets, blood is able to mend cuts to prevent bleeding by forming clots with the platelets. Given the importance of blood, it should come to no surprise that cardiac and **hematological** diseases (e.g., **atherosclerosis**) often prove critical if not treated adequately and timely.

To correctly diagnose such diseases is difficult, as symptoms are often quite generic. For a correct diagnosis, more information is required, requiring gathering data through performing measurements. Therefore, being able to perform reliable measurements on blood properties and blood flow is crucial for a doctor to correctly diagnose a patient.

Many techniques exist for measuring blood properties and composition, such as extracting a patient's blood and analysing its contents in a laboratory. This can, in fact, yield information on a great many diseases not directly relating to the blood itself.

MEASURING BLOOD FLOW

Diseases such as atherosclerosis are more related to the flow of blood through the arterial system than to the properties and composition of the blood itself. Various techniques exist for determining properties and anomalies of the blood flow, preferably through measurements performed outside of the body. Each technique has its advantages and disadvantages; or, applications in which it performs well and others in which it cannot be used. Ideally, measurement techniques should be **non-invasive**, in addition to being cheap, accurate, **in-vivo** and **real-time**.

Medical sonography uses transmission or reflection of ultrasound, which is particularly useful for imaging soft tissue. [1] Probably the most well-known application is fetal (B-mode or M-mode) ultrasound, i.e., imaging unborn babies using sound echos. [2, 3] *Doppler sonography*, using the Doppler effect for **velocimetry**, can be used to visualize and measure the blood velocity locally. This technique is useful for locating a **stenosis** [4]; however – like all Doppler-based techniques – whereas it has a good axial (depth) resolution, its lateral (sideways) resolution is poor, requiring the measurement device to be placed as parallel to the flow as possible. This is a limitation, as many important arteries are more or less parallel to the skin, making perpendicular imaging most practical.

Another technique that can measure the blood velocity locally – and thereby detect stenoses amongst many other things – is *Magnetic Resonance Angiography (MRA)*, which is a type of **MRI** specially for blood flow. [4, 5] In **MRA**, hydrogen atoms are excited electromagnetically, and, subsequently, the photons emitted as the atoms de-excite are mea-

sured. This technique is very accurate and versatile, but it is unfortunately very expensive and provides a considerable amount of discomfort to the patient.

As a cheap and versatile imaging technique, light has historically held great potential. [6] When **direct imaging** is possible, *Particle Image Velocimetry (PIV)* can be used for velocimetry by carefully tracking the movement of the imaged particles. [7] When direct imaging is not possible (i.e., **indirect imaging**), such as in **turbid media**, *photoacoustic imaging* could be used to image contrasts between absorptive and non-absorptive tissue at up to 2-3 cm depth in the body. [6, 8] Short pulses of light are used to locally heat primarily the highly absorptive tissue, which causes a small expansion of the tissue, producing an ultrasound wave that can be measured.

However, to perform measurements it is not necessarily required to do imaging. Alternatively, *Photoplethysmography (PPG)* might be useful. **PPG** is a very cheap technique that measures light absorption by illuminating skin at one side and measuring at the other side. **PPG** is popularly used in a pulse oximeter to measure a heartbeat through the fluctuations in light absorption as more or less red blood cells pass by over time. [9] **PPG** may also be used to detect **peripheral vascular disease** [10], and to measure oxygen saturation and blood pressure.

Whereas **PPG** only considers the absorption of light, the full **scattered field of light** after passing through or reflected by a body part could yield much more information about the underlying medium. *Diffuse optics techniques* may be used to study dynamics in turbid media, such as blood flow in the body. [11, 12]

LASER SPECKLE IMAGING TECHNIQUES

A technique that capitalizes on the scattered light specifically is *Laser Speckle Imaging (LSI)*: a method for indirect imaging, in which a plane wave of coherent light illuminates a patient locally, and the subsequent (**multiply scattered light**) is measured. The result is a somewhat random interferometric pattern: a **speckle pattern**. Any dynamics in the scattering medium will result in the speckle pattern to change over time through **translating speckle** or so-called **speckle boiling** [13]; therefore, the dynamics of the speckles contains information about (the dynamics of) the underlying medium.

Until now, **LSI** has mostly been used to study **blood perfusion** from capillary beds. [14, 15] Recently, a technique called *dynamic light scattering imaging (DLSI)* was developed, which uses temporal speckle intensity autocorrelation functions to improve the quantitative measurement of cerebral blood flow. [16] Other researchers have recently combined **LSI** with **PIV** into their *optical speckle image velocimetry (OSIV)* technique, which works by tracking the speckles of translating speckle, but without the need for seeding particles like in **PIV**. [17] Both methods are able to beautifully reconstruct the entire velocity field in the capillary system of mice's brains. Unfortunately, DLSI requires the dynamics to be sufficiently slow and will in practice only work for small arteries (i.e., diameter $< 200\mu\text{m}$), while OSIV relies on negligible speckle boiling to properly track the movement of the speckles. Another, related, major limitation to both methods is that they could only be achieved in an invasive manner: opening up the mouse's skull.

In the present thesis, we are interested primarily in measuring the blood flow in the **carotid artery**, where the above techniques optimised for blood perfusion cannot be used directly, as different length and time scales are involved in our application. How-

ever, it has been shown previously that *Laser Speckle Contrast Imaging (LSCI)* is a good candidate technique for the carotid artery. [18–20] The LSCI technique is a type of LSI, in which the *speckle contrast* is used as a metric. Through the speckle contrast, we can measure the dynamics of the speckle pattern, providing a measure of the dynamics of the underlying scattering medium. [21]

Presently, LSCI is not yet the desired fully quantitative measurement technique that it hopefully can become. [17, 22] For example, in an actual in-vivo situation, amongst many other noise factors, a patient's skin will introduce noise on the measured signal. Further research is required to study the precise effect of such a static surrounding medium, and thereafter how to filter that effect to enable measuring in-vivo and non-invasively. And even if we do, each individual patient might require a different filter, for which patient-specific calibration may always remain necessary. [22]

Additionally, there still exists disagreement in the literature about how to quantitatively derive the velocities inside the scattering medium from a speckle pattern. Although the speckle contrast, K , provides a metric to measure the velocity, the precise relationship between velocity and K remains elusive, even in a 'perfect' laboratory situation. [14, 23–26] Therefore, more research is required to settle the debate, and to turn LSCI into the non-invasive and in-vivo quantitative measurement technique that it can hopefully become.

RESEARCH QUESTIONS AND METHODOLOGY OF THIS THESIS

The goal of my thesis is to unlock the full potential of LSCI for blood flow velocimetry from outside the body, or at least take big steps towards that end:

Can we perform velocimetry measurements using light scattered by in-vivo flowing blood for medical diagnosis purposes?

A positive answer to this question could lead to a new medical measurement technique that is cheap, while resulting in only minimal discomfort to the patient by being non-invasive and in-vivo. Hopefully, this technique will aid in prematurely detecting serious arterial diseases, such as atherosclerosis.

To answer the research question, we deploy a numerical methodology, i.e., we perform computer simulations of both the blood flow and the LSCI measurement technique in their mutual interaction. In a simulation setup, we are able to vary input parameters and for each combination generate an output, i.e., perform *numerical experiments*. The goal is to find relationships between output and input, and thereby gain a thorough understanding of the physics involved in the scattering of light by red blood cells and accounting for all interacting factors. The advantage of our approach over physical experiments, is that in numerical experiments we can more quickly vary parameters, and situations difficult to reproduce in a laboratory setup may be attainable in numerical experiments; however, physical experiments will always be required in conjunction with numerical experiments to verify their veracity

Eventually, our work should lead to new medical measurement devices. To that end, we have developed a new computational model and computer code to simulate the whole LSCI process.

OUTLINE OF THIS THESIS

The underlying electromagnetic, optical and fluid dynamics theories that our model is based on, will first be discussed in Chap. 1.

Subsequently, Chap. 2 will outline our numerical **LSCI** algorithm, as well as discuss the made simplifications and their consequences. The first part of Chap. 2 describes our optics code, which simulates instantaneous light scattering by an ensemble of particles. The second part of Chap. 2 presents the fluids code, which is used for simulating the motion of particles, including in complex arterial geometries. The third and last part of Chap. 2 describes the coupling of the optics code to the fluids code to simulate light scattering by arbitrarily moving particles. The used fluids code is a well established **Computational Fluid Dynamics (CFD)** code that needs little further validation; however, our optics code is new and will be validated in Chap. 3.

In the following three chapters, we subdivide our research question into three specific questions. While related, each has a different (medical) application.

Firstly, in Chap. 4 we perform numerical experiments to answer the question whether **LSCI** can at least do the same as **PPG**: “*Can we use **LSCI** to measure the **frequency signature** of a flow modulated by a pulsatile heartbeat-like signal?*” We deploy a simple cylindrical geometry seeded with spherical tracer particles, representing blood flow in a patient’s artery. We study the effect of various quantities – most notably the effect of the very important **speckle boiling** phenomenon.

Secondly, in Chap. 5 we take the next step towards extracting more information from the **LSCI** measurements. The goal is to perform quantitative **velocimetry** measurements – “*Can we use **LSCI** to measure the velocity of the underlying **scatterers** in a turbid flow?*” – and compare the obtained quantitative relationship to theoretical models. This is an important question, as there exists the aforementioned disagreement in the literature as to how to quantitatively derive the velocity from the speckle contrast [14, 24], while performing accurate *quantitative* measurements is pivotal to medical devices.

Thirdly, in Chap. 6 we take the first major step towards what a medical device could potentially do – “*Can we detect atherosclerosis from light scattered by in-vivo flowing blood?*” We simulate a complex patient-specific **sclerosed** artery, i.e., an artery suffering from the disease **atherosclerosis** in which a buildup of **plaque** has caused the narrowing of the artery. We find characteristic signatures in the scattered light for specific underlying flow features, e.g., for a **bifurcation** and for the region around the **stenosis**.

Finally, Chap. 7 will bring it all together to answer our main research question, provide opportunities for future research, and speculate about other applications of our research.

BIBLIOGRAPHY

1. Carovac, A., Smajlovic, F. & Junuzovic, D. Application of ultrasound in medicine. *Acta Informatica Medica* **19**, 168 (2011).
2. Mohamed, A. A., Arifi, A. A. & Omran, A. The basics of echocardiography. *Journal of the Saudi Heart Association* **22**, 71–76 (2010).
3. Fetal Ultrasound. *Johns Hopkins Medicine*. <https://www.hopkinsmedicine.org/health/treatment-tests-and-therapies/fetal-ultrasound> (Jan. 2022).
4. Meschia, J. F., Klaas, J. P., Brown Jr, R. D. & Brott, T. G. Evaluation and management of atherosclerotic carotid stenosis. *Mayo Clinic Proceedings* **92**, 1144–1157 (2017).
5. Magnetic Resonance Angiography (MRA). *Johns Hopkins Medicine*. <https://www.hopkinsmedicine.org/health/treatment-tests-and-therapies/magnetic-resonance-angiography-mra> (Nov. 2019).
6. Yun, S. H. & Kwok, S. J. Light in diagnosis, therapy and surgery. *Nature biomedical engineering* **1**, 0008 (2017).
7. Adrian, R. J. Twenty years of particle image velocimetry. *Experiments in fluids* **39**, 159–169 (2005).
8. Steinberg, I. *et al.* Photoacoustic clinical imaging. *Photoacoustics* **14**, 77–98 (2019).
9. Allen, J. Photoplethysmography and its application in clinical physiological measurement. *Physiological measurement* **28**, R1 (2007).
10. Peripheral Vascular Disease. *Johns Hopkins Medicine*. <https://www.hopkinsmedicine.org/health/conditions-and-diseases/peripheral-vascular-disease> (Aug. 2021).
11. Tuchin, V. *Tissue Optics: Light Scattering Methods and Instruments for Medical Diagnosis* (SPIE press Bellingham, 2007).
12. Boas, D. A. & Dunn, A. K. Laser speckle contrast imaging in biomedical optics. *Journal of Biomedical Optics* **15**, 011109 (2010).
13. Asakura, T. & Takai, N. Dynamic laser speckles and their application to velocity measurements of the diffuse object. *Applied Physics* **25**, 179–194 (1981).
14. Draijer, M., Hondebrink, E., van Leeuwen, T. & Steenbergen, W. Review of laser speckle contrast techniques for visualizing tissue perfusion. *Lasers in Medical Science* **24**, 639 (2009).
15. Dunn, A. K. Laser speckle contrast imaging of cerebral blood flow. *Annals of Biomedical Engineering* **40**, 367–377 (2012).

16. Postnov, D. D., Tang, J., Erdener, S. E., Kiliç, K. & Boas, D. A. Dynamic light scattering imaging. *Science advances* **6**, eabc4628 (2020).
17. Qureshi, M. M. *et al.* Quantitative blood flow estimation in vivo by optical speckle image velocimetry. *Optica* **8**, 1092–1101 (Aug. 2021).
18. Nemati, M., Presura, C. N., Urbach, H. P. & Bhattacharya, N. Dynamic light scattering from pulsatile flow in the presence of induced motion artifacts. *Biomed. Opt. Express* **5**, 2145–2156 (2014).
19. Nemati, M. *et al.* Application of full field optical studies for pulsatile flow in a carotid artery phantom. *Biomedical optics express* **6**, 4037–4050 (2015).
20. Nemati, M., Kenjeres, S., Urbach, H. P. & Bhattacharya, N. Fractality of pulsatile flow in speckle images. *Journal of Applied Physics* **119**, 174902 (2016).
21. Fercher, A. F. & Briers, J. D. Flow visualization by means of single-exposure speckle photography. *Optics Communications* **37**, 326–330 (1981).
22. Briers, D. *et al.* Laser speckle contrast imaging: theoretical and practical limitations. *Journal of Biomedical Optics* **18**, 066018 (2013).
23. Briers, J. D. & Webster, S. Laser speckle contrast analysis (LASCA): a non-scanning, full-field technique for monitoring capillary blood flow. *Journal of Biomedical Optics* **1**, 174–180 (1996).
24. Duncan, D. D. & Kirkpatrick, S. J. Can laser speckle flowmetry be made a quantitative tool? *J. Opt. Soc. Am. A* **25**, 2088–2094 (2008).
25. Duncan, D. D., Kirkpatrick, S. J. & Gladish, J. C. *What is the proper statistical model for laser speckle flowmetry?* in *Complex Dynamics and Fluctuations in Biomedical Photonics V* **6855** (2008), 685502.
26. Liu, C., Kiliç, K., Erdener, S. E., Boas, D. A. & Postnov, D. D. Choosing a model for laser speckle contrast imaging. *Biomed. Opt. Express* **12**, 3571–3583. <https://opg.optica.org/boe/abstract.cfm?URI=boe-12-6-3571> (June 2021).

1

THEORY

In this chapter, the relevant background theory will be summarised. Some more detailed derivations are delegated to an appendix. In Sec. 1.1, Mie theory will be derived, which computes the light scattered by a spherical scatterer of any size. In Sec. 1.2, the relevant properties of blood are described, followed by the governing equations describing any flow: the Navier-Stokes equations. In Sec. 1.3 some relevant exact solutions to the Navier-Stokes equations are given. In Sec. 1.4, Lagrangian particle tracking is described, together with the possibly relevant forces, which is used to simulate the movement of particles.

This chapter was published previously: Van As, K. (2015). *Interferometric Scattering of Light by an Ensemble of Flowing Spherical Particles: A Numerical Study* [Master's Thesis, Delft University of Technology]. [1] Available online via <http://repository.tudelft.nl>.

1.1. MIE THEORY

While studying the colour effects of colloidal gold particles, in 1908 Gustav Mie (1868-1957) derived a solution for **diffraction** by a sphere [2]. This paper was written in German. Ever since, two English translations have appeared in the literature [3, 4], which wasn't until 1976. In fact, Mie's paper was almost ignored altogether until 1945 [5], likely because his theory was impractical, given the infinite series and **Ricatti-Bessel functions** involved. His solution had to wait for the digital era and until stable algorithms were developed.

Nowadays, many books on Electrodynamics and Optics derive the Mie solution. In van de Hulst [6], a brief derivation using Gaussian units is given, which is a nice starting point. Stratton [7] contains a more rigorous derivation, as do Bohren & Huffman [8].

In this section, the book of Bohren & Huffman will be followed closely, without referring it repetitively. The most important steps and thoughts in the derivation will be summarised.

1.1.1. MAXWELL'S EQUATIONS AND THE WAVE EQUATION

Let \vec{E} resp. \vec{H} be the electric and magnetic fields. Then, assuming a periodic field $\vec{A} = \text{Re}\{\vec{A}_c e^{-i\omega t}\}$ ($\vec{A}_c \in \mathbb{C}^3$), with $\vec{A} \in \{\vec{E}, \vec{H}\}$, the **Maxwell equations** may be written in the form:

$$\nabla \cdot (\epsilon \vec{E}_c) = 0, \quad (1.1)$$

$$\nabla \times \vec{E}_c = i\omega\mu\vec{H}_c, \quad (1.2)$$

$$\nabla \cdot \vec{H}_c = 0, \quad (1.3)$$

$$\nabla \times \vec{H}_c = -i\omega\epsilon\vec{E}_c, \quad (1.4)$$

where ω is the frequency of the periodic solution, μ is the (magnetic) **permeability** and the complex (electric) **permittivity** is

$$\epsilon = \epsilon_0(1 + \chi) + i\sigma/\omega, \quad (1.5)$$

where σ is the **conductivity** and χ is the **electric susceptibility**. All these parameters depend on the propagation medium.

Starting from Maxwell's Equations, it is possible to derive the vector wave equation, which both \vec{E} and \vec{H} must satisfy:

$$\nabla^2 \vec{A}_c + k^2 \vec{A}_c = \vec{0}, \quad (1.6)$$

where $k^2 = \omega^2\mu\epsilon \rightarrow k = \omega(N/c) \equiv Nk_0$ is the **wave number**, where the (complex) **refractive index** was introduced, given in terms of the electromagnetic constants/coefficients:

$$N = \sqrt{\frac{\epsilon\mu}{\epsilon_0\mu_0}} = n(1 + i\kappa) \quad (1.7)$$

where the subscript 0 indicates the value of the parameter in vacuum. Also, $c = 1/\sqrt{\epsilon_0\mu_0}$ is the speed of light in vacuum.

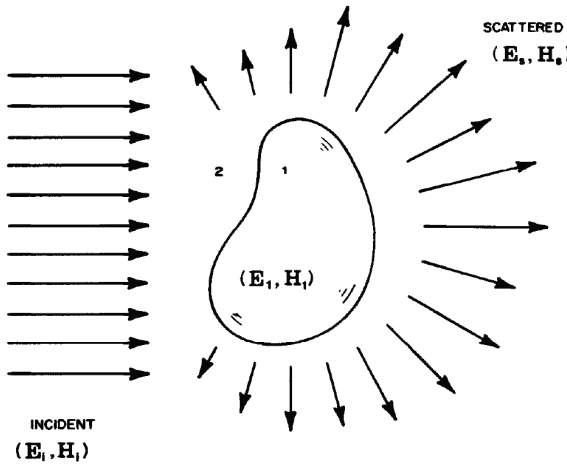


Figure 1.1: Geometry of the scattering problem by an arbitrary particle. In Mie theory, a spherical particle will be considered. Reproduced from Bohren & Huffman Fig. 3.1 (p58) [8].

The scalar wave equation (Helmholtz equation) is just Eq. (1.6):

$$\nabla^2 \psi + k^2 \psi = 0. \quad (1.8)$$

As tempting as it is, the individual components of \vec{A}_c do not satisfy the scalar wave equation separately. From Eq. (1.8) this is not obvious, since the coupling of the components occur in the **Boundary Conditions (BCs)**, to be considered below.

1.1.2. DERIVATION OF THE SCATTERED FIELD

Consider the **scattering** geometry in Fig. 1.1. A **Plane Wave (PW)** is incident on a particle, which will exert a force on the electrons within the particle. Their movement will both alter the internal and external field. In scattering theory, we consider the external field as a superposition of the incident, \vec{E}_i , and scattered field, \vec{E}_s :

$$\vec{E}_2 = \vec{E}_i + \vec{E}_s. \quad (1.9)$$

At the particle's boundary, these internal and external fields are coupled via electromagnetic **BCs**. In **Mie theory**, a spherical **scatterer** is observed, which gives a *relatively* easy exact solution.

Boundary Conditions. **BCs** are contained within the Maxwell equations and found by integrating them over a small volume or a small loop around a boundary. Integrating over a volume yields a condition for the normal component via Eqs. (1.1 and 1.3). The tangential component follows from Eqs. (1.2 and 1.4). These **BCs** are respectively:

$$[\epsilon_2 \vec{E}_2 - \epsilon_1 \vec{E}_1] \cdot \hat{n}|_{r=a} = 0, \quad (1.10)$$

$$[\mu_2 \vec{H}_2 - \mu_1 \vec{H}_1] \cdot \hat{n}|_{r=a} = 0, \quad (1.11)$$

$$[\vec{E}_2 - \vec{E}_1] \times \hat{n}|_{r=a} = \vec{0}, \quad (1.12)$$

$$[\vec{H}_2 - \vec{H}_1] \times \hat{n}|_{r=a} = \vec{0}, \quad (1.13)$$

where \hat{n} is the outwards normal of the particle: $\hat{n} = \hat{r}$ for a sphere. Index 1 refers to the internal field and index 2 refers to the external field, cf. Fig. 1.1. a denotes the radius of the spherical particle.

Solve the Scalar Wave Equation. The scalar wave equation Eq. (1.8) in spherical coordinates is most easily solved using separation of variables (r, θ, φ) . The linearly independent basis set of solutions are:

$$\begin{aligned}\psi_{enm} &= \cos(m\varphi) P_n^m(\cos\theta) z_n(kr), \\ \psi_{onm} &= \sin(m\varphi) P_n^m(\cos\theta) z_n(kr),\end{aligned}\tag{1.14}$$

where e and o denote ‘even’ and ‘odd’ respectively. P_n^m is the [associated Legendre polynomial](#) and z_n denotes any [spherical Bessel function](#). As usual when solving a linear differential equation, the general solution is a superposition of all solutions in the basis set of solutions.

Solve the Vector Wave Equation. As mentioned, \vec{E} and \vec{H} do not satisfy the scalar wave equation. However, the solution to the scalar wave equation may be used to construct solutions to the vector wave equation (proof by direct substitution):

$$\begin{aligned}\vec{M} &= \nabla \times (\vec{r}\psi), \\ k\vec{N} &= \nabla \times \vec{M}, \\ k\vec{M} &= \nabla \times \vec{N},\end{aligned}\tag{1.15}$$

which gives a total of four vector solutions for each $\{n, m\}$. These solutions are called [Vector Spherical Harmonics \(VSHs\)](#). Written out in its entirety, using¹ $\rho \equiv kr$:

$$\begin{aligned}\vec{M}_{\{e\}mn} &= \begin{Bmatrix} -\sin m\varphi \\ \cos m\varphi \end{Bmatrix} \frac{m}{\sin\theta} P_n^m(\cos\theta) z_n(\rho) \hat{\theta} \\ &+ \begin{Bmatrix} -\cos m\varphi \\ -\sin m\varphi \end{Bmatrix} \frac{dP_n^m(\cos\theta)}{d\theta} z_n(\rho) \hat{\varphi},\end{aligned}\tag{1.16}$$

$$\begin{aligned}\vec{N}_{\{o\}mn} &= \begin{Bmatrix} \cos m\varphi \\ \sin m\varphi \end{Bmatrix} n(n+1) P_n^m(\cos\theta) \frac{z_n(\rho)}{\rho} \hat{r} \\ &+ \begin{Bmatrix} \cos m\varphi \\ \sin m\varphi \end{Bmatrix} \frac{dP_n^m(\cos\theta)}{d\theta} \frac{1}{\rho} \frac{d(\rho z_n(\rho))}{d\rho} \hat{\theta} \\ &+ \begin{Bmatrix} -\sin m\varphi \\ \cos m\varphi \end{Bmatrix} \frac{P_n^m(\cos\theta)}{\sin\theta} \frac{m}{\rho} \frac{d(\rho z_n(\rho))}{d\rho} \hat{\varphi}.\end{aligned}\tag{1.17}$$

¹Note that ρ depends on k , which depends on the medium via the refractive index: $k = Nk_0$.

Expand the Incident Field in terms of Vector Spherical Harmonics. The incident field is a **PW**, which is without loss of generality² written as:

$$\vec{E}_i = E_0 e^{ik_2 z} \hat{x} = E_0 e^{ik_2 r \cos \theta} (\sin \theta \cos \varphi \hat{r} + \cos \theta \cos \varphi \hat{\theta} - \sin \varphi \hat{\phi}), \quad (1.18)$$

which may be expanded in terms of **VSHs**, which are the basis functions of the studied system:

$$\vec{E}_i = E_0 \sum_{n=1}^{\infty} i^n \frac{2n+1}{n(n+1)} \left(\vec{M}_{o1n}^{(1)} - i \vec{N}_{e1n}^{(1)} \right), \quad (1.19)$$

which follows from the equivalent of Fourier's trick: take the functional inner product and by the orthogonality of the **VSHs** Eq. (1.15) many terms drop out. The coefficients may then be computed using the non-zero inner products of the non-orthogonal functions. The '(1)' refers to the use of the spherical Bessel function of the first kind, $z_n^{(1)} \equiv j_n$, which is the only finite Bessel function in the origin, which is required since Eq. (1.18) is finite in the origin.

Arriving at this solution is the most difficult part of the Mie derivation. To quote Bohren & Huffman [8] (p92): *"This is undoubtedly the result of the unwillingness of a plane wave to wear a guise in which it feels uncomfortable; expanding a plane wave in spherical wave functions is somewhat like trying to force a square peg into a round hole."*

Notably in Eq. (1.19), only the $m = 1$ term survived, because the incident field Eq. (1.18) only possesses the $m = 1$ term. By **orthogonality** of the cosine and sine function, all terms other than $m = 1$ will then drop out during expansion.

Finally, the magnetic field, \vec{H}_i , follows from the curl of Eq. (1.19), cf. Eq. (1.2):

$$\vec{H}_i = \frac{-k_2}{\omega \mu_2} E_0 \sum_{n=1}^{\infty} i^n \frac{2n+1}{n(n+1)} \left(\vec{M}_{e1n}^{(1)} + i \vec{N}_{o1n}^{(1)} \right). \quad (1.20)$$

Expand the other Fields in terms of Vector Spherical Harmonics. The next step in the derivation is to expand the other fields in terms of **VSHs**, as that is the general solution to the vector wave equation Eq. (1.6). We may write:

$$\vec{E}_1 = \sum_{n=1}^{\infty} E_n \left(c_n \vec{M}_{o1n}^{(1)} - i d_n \vec{N}_{e1n}^{(1)} \right), \quad (1.21)$$

$$\vec{H}_1 = \frac{-k_1}{\omega \mu_1} \sum_{n=1}^{\infty} E_n \left(d_n \vec{M}_{e1n}^{(1)} + i c_n \vec{N}_{o1n}^{(1)} \right), \quad (1.22)$$

where $E_n = E_0 i^n (2n+1) / n(n+1)$, which is merely for convenience. The spherical Bessel function of the first kind has been used, because of its finiteness at the origin, which is contained within the internal region. Again, the magnetic field followed from the curl.

²A sphere is highly symmetrical, so at this point the coordinate system is arbitrary. However, by choosing the propagation direction as the z -axis and the polarisation of the electric field along the x -axis, we fix the coordinate system. If in some external lab frame the propagation direction and/or the **polarisation** is different (but still orthogonal), a simple rotation of axis permits usage of the Mie solution as derived with a fixed orientation, i.e., no generality was lost in fixing the coordinate system.

Similarly, the scattered field may be expanded according to:

$$\vec{E}_s = \sum_{n=1}^{\infty} E_n \left(i a_n \vec{N}_{e1n}^{(3)} - b_n \vec{M}_{o1n}^{(3)} \right), \quad (1.23)$$

$$\vec{H}_s = \frac{k_2}{\omega \mu_2} \sum_{n=1}^{\infty} E_n \left(i b_n \vec{N}_{o1n}^{(3)} + a_n \vec{M}_{e1n}^{(3)} \right), \quad (1.24)$$

where the spherical Bessel function of the third kind \equiv **spherical Hankel function** of the first kind, $z_n^{(3)} \equiv h_n^{(1)}$ has been used. This follows from its asymptotic behaviour. It becomes an outgoing spherical wave for $kr \gg n^2$:

$$h_n^{(1)}(kr) \sim \frac{(-i)^n e^{ikr}}{ikr}, \quad (1.25)$$

which is to be expected on physical grounds for a scattering process.

The reader may wonder why $m \neq 1$ is again omitted. And why are the \vec{N}_{omn} and \vec{M}_{emn} terms omitted for \vec{E} ? This follows from the **BCs**, in combination with the orthogonality of the **VSHs** and the fact that the incident field Eq. (1.19) does not possess those terms. Since I'd not just believe that either, a more detailed description may be found in App. A.1.

Find the Mie Coefficients. The Mie coefficients, $\{a_n, b_n, c_n, d_n\}$, are finally found by applying the **BCs** Eqs. (1.10-1.13) to the field expansions Eqs. (1.19-1.24). The derivation may be found in App. A.2. Four equations with four unknowns are then found, from which all four coefficients follow. In this research, only the scattering coefficients are of interest:

$$a_n = \frac{\mu_2 m^2 j_n(y) [x j_n(x)]' - \mu_1 j_n(x) [y j_n(y)]'}{\mu_2 m^2 j_n(y) [x h_n^{(1)}(x)]' - \mu_1 h_n^{(1)}(x) [y j_n(y)]'}, \quad (1.26)$$

$$b_n = \frac{\mu_1 j_n(y) [x j_n(x)]' - \mu_2 j_n(x) [y j_n(y)]'}{\mu_1 j_n(y) [x h_n^{(1)}(x)]' - \mu_2 h_n^{(1)}(x) [y j_n(y)]'}, \quad (1.27)$$

where $x \equiv k_2 a$ is the **size parameter**, $y \equiv k_1 a = mx$, and m is the *relative* refractive index:

$$m \equiv \frac{k_1}{k_2} = \frac{N_1}{N_2} = \sqrt{\frac{\epsilon_1 \mu_1}{\epsilon_2 \mu_2}}. \quad (1.28)$$

To simplify the Mie coefficient, we introduce the **Ricatti-Bessel functions**:

$$\psi_n(\rho) \equiv \rho j_n(\rho), \quad (1.29)$$

$$\xi_n(\rho) \equiv \rho h_n^{(1)}(\rho), \quad (1.30)$$

from which the Mie coefficients simplify to:

$$a_n = \frac{\mu_2 m \psi_n(y) \psi_n'(x) - \mu_1 \psi_n(x) \psi_n'(y)}{\mu_2 m \psi_n(y) \xi_n'(x) - \mu_1 \xi_n(x) \psi_n'(y)}, \quad (1.31)$$

$$b_n = \frac{\mu_1 \psi_n(y) \psi_n'(x) - \mu_2 m \psi_n(x) \psi_n'(y)}{\mu_1 \psi_n(y) \xi_n'(x) - \mu_2 m \xi_n(x) \psi_n'(y)}. \quad (1.32)$$

In the present research, $\mu_1 = \mu_2 = \mu_0 \equiv \mu$, and thus μ will drop out of the coefficients.

1.1.3. AMPLITUDE SCATTERING MATRIX

Substituting the definition of the VSHs Eqs. (1.16 and 1.17) into the field expansion Eq. (1.23), yields:

$$\vec{E}_s \cdot \hat{r} = \frac{\cos \varphi}{\rho^2} \sum_{n=1}^{\infty} E_n i a_n n(n+1) \sin \theta \pi_n(\cos \theta) \xi_n(\rho), \quad (1.33)$$

$$\vec{E}_s \cdot \hat{\theta} = \frac{\cos \varphi}{\rho} \sum_{n=1}^{\infty} E_n (i a_n \tau_n(\cos \theta) \xi'_n(\rho) - b_n \pi_n(\cos \theta) \xi_n(\rho)), \quad (1.34)$$

$$\vec{E}_s \cdot \hat{\phi} = \frac{-\sin \varphi}{\rho} \sum_{n=1}^{\infty} E_n (i a_n \pi_n(\cos \theta) \xi'_n(\rho) - b_n \tau_n(\cos \theta) \xi_n(\rho)), \quad (1.35)$$

where two angular functions were introduced to replace the associated Legendre polynomials:

$$\tau_n(\cos \theta) \equiv \frac{dP_n^1(\cos \theta)}{d\theta}, \quad \pi_n(\cos \theta) \equiv \frac{P_n^1(\cos \theta)}{\sin \theta}. \quad (1.36)$$

As it turns out, these two angular functions possess nice recursive properties, useful for numerical algorithms [8, 9].

If we now apply the **Far-Field (FF)** approximation, ξ_n may be replaced by its asymptotic limit, cf. Eqs. (1.25 and 1.30). It then follows that the radial component of \vec{E}_s falls off $1/\rho$ faster than the other components, making it negligible in the **FF**. We are left with (using $\mu \equiv \cos \theta$):

$$\vec{E}_s \cdot \hat{\theta} \sim \cos \varphi \frac{e^{i\rho}}{-i\rho} E_0 \sum_{n=1}^{\infty} \frac{2n+1}{n(n+1)} \left(a_n \tau_n(\mu) + b_n \pi_n(\mu) \right), \quad (1.37)$$

$$\vec{E}_s \cdot \hat{\phi} \sim -\sin \varphi \frac{e^{i\rho}}{-i\rho} E_0 \sum_{n=1}^{\infty} \frac{2n+1}{n(n+1)} \left(a_n \pi_n(\mu) + b_n \tau_n(\mu) \right). \quad (1.38)$$

Upon introduction of the **amplitude scattering matrix**, $[S](\mu)$, this may be written in the form:

$$\begin{bmatrix} \vec{E}_s \cdot \hat{\theta} \\ \vec{E}_s \cdot \hat{\phi} \end{bmatrix} = \frac{e^{i\rho}}{-i\rho} E_0 \begin{bmatrix} S_2 & 0 \\ 0 & S_1 \end{bmatrix} \begin{bmatrix} \cos \varphi \\ -\sin \varphi \end{bmatrix}, \quad (1.39)$$

where the components of the amplitude scattering matrix are given by

$$\begin{aligned} S_2(\mu) &\equiv \sum_{n=1}^{\infty} \frac{2n+1}{n(n+1)} \left(a_n \tau_n(\mu) + b_n \pi_n(\mu) \right), \\ S_1(\mu) &\equiv \sum_{n=1}^{\infty} \frac{2n+1}{n(n+1)} \left(a_n \pi_n(\mu) + b_n \tau_n(\mu) \right). \end{aligned} \quad (1.40)$$

Finally, recall that the incident field was chosen to travel in the \hat{z} -direction and polarised in the \hat{x} -direction. With this convention, $\theta = \theta_s$ is the **scattering angle**: the angle between the propagation vector of the incident field ($\vec{k}_i = k\hat{z}$) and the propagation vector of the scattered field ($\vec{k}_s = k\hat{r}$). The **scattering plane**, which is per definition the plane spanned by those two propagation vectors, is a vertical plane rotated with an angle φ with respect to the \hat{x} -axis. This is illustrated by Fig. 1.2.

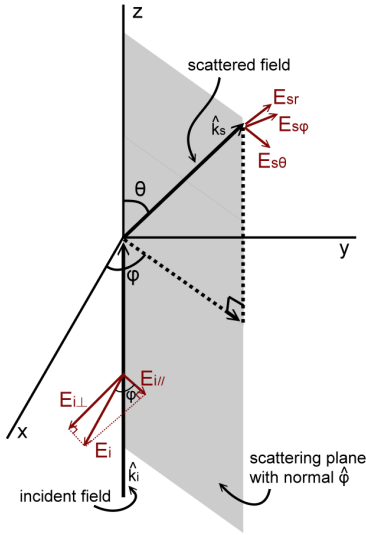


Figure 1.2: The standard scattering geometry is shown: an **Incoming Plane Wave** is coming in from below with $\hat{k}_i = \hat{z}$ and is scattered radially outward from the origin $\hat{k}_s = \hat{r}$, which is the position of a scatterer.

The scattering plane is per definition the area spanned by these two propagation vectors, which is shown as a gray shaded area in the figure. Its unit normal is $\hat{\phi}$.

Any incident field (here: polarised in the \hat{x} -direction) may be resolved into a parallel (E_{\parallel}) and perpendicular (E_{\perp}) component relative to the scattering plane. The same applies to the scattered field. For an arbitrary coordinate system, the fields may then be expressed in terms of those parallel and perpendicular components.

Noting that a rotation of axis preserves orthogonality, it follows that for an arbitrary coordinate system we can use the component parallel and perpendicular to the scattering plane. In cylindrical coordinates (s, φ, z) , the incident field may be written as

$$\vec{E}_i = E_0 e^{ikz} \hat{x} = E_0 e^{ikz} (\cos \varphi \hat{s} - \sin \varphi \hat{\phi}), \quad (1.41)$$

where the $\hat{\phi}$ -component is orthogonal to the scattering plane and \hat{s} is parallel to it (see Fig. 1.2).

Comparing this result for the incident field with Eq. Eq. (1.39), and noting that the $\hat{\phi}$ -component is orthogonal to the scattering plane and that the $\hat{\theta}$ -component is parallel to it, we may write:

$$\begin{bmatrix} E_{s\parallel} \\ E_{s\perp} \end{bmatrix} = \frac{e^{ik(r-z)}}{-ikr} \begin{bmatrix} S_2 & 0 \\ 0 & S_1 \end{bmatrix} \begin{bmatrix} E_{i\parallel} \\ E_{i\perp} \end{bmatrix}, \quad (1.42)$$

where e^{-ikz} was merely introduced to cancel the exponential in Eq. (1.41), i.e., the left hand side is solely a function of r (and θ via $[S]$) and not of z , which is confusing in Mie theory literature.

1.1.4. MULTIPLE SCATTERERS

When multiple scatterers are considered, it is required to convert Mie theory to some global coordinate system, i.e., currently the origin was set in the center of the scatterer, which is ambiguous with multiple scatterers. Also, the different scatterers will very likely have a different initial **phase**, which must be considered.

Global Coordinates. In order to define Mie theory with respect to some global coordinate system, it is important to express everything relative to some common origin. In Fig. 1.3, we define

$$\vec{z} \equiv \vec{r} - \vec{r}', \quad (1.43)$$

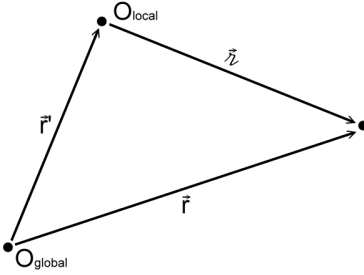


Figure 1.3: \tilde{z} is used to define a difference in position, which permits the local coordinates (which used \tilde{r} in previous sections) to be written in global coordinates (which now claims the symbol \tilde{r}).

where \tilde{r} is the position with respect to the global origin and \tilde{r}' is the position of the local origin with respect to the global origin. In Mie theory, \tilde{r}' is the position of the scatterer with respect to the global origin.

Using this symbol, it is possible to replace all \tilde{r} derived in local coordinates by \tilde{z} and the solution in global coordinates has been found. E.g., Eq. (1.42) becomes:

$$\begin{bmatrix} E_{s\parallel} \\ E_{s\perp} \end{bmatrix} = \frac{e^{ik(\tilde{z}-z)}}{-ik\tilde{z}} \begin{bmatrix} S_2 & 0 \\ 0 & S_1 \end{bmatrix} \begin{bmatrix} E_{i\parallel} \\ E_{i\perp} \end{bmatrix}. \quad (1.44)$$

Initial Phase. Since Mie theory was derived in a local coordinate system, the reference to any sort of initial phase is lost. However, it is still implicitly contained within the solution, i.e., the factor $e^{-i\omega t}$ is omitted in the complex notation of the electric field, but the combination of $e^{-i\omega t}$ and e^{ikz} determines a spacetime origin for the **Incoming Plane Wave (IPW)**, which cannot be the same for all scatterers.

Fig. 1.4 shows a test geometry which has an identical distance between each particle and the scattering target, such that only the initial phase may influence the relative phase of the two scatterers. Since we wish to measure the scattered field of the two scatterers simultaneously, it is required to sample the IPW at a different time (t_{-1} vs. t_0) at the same z or at a different z at the same time (t_0). So, with respect to some common global origin where $z = 0$, we may write for the field at the scatterer's local origin (using $\vec{k}_i = k\hat{z}$):

$$\vec{E}(\vec{r}_1, t) = \vec{E}(\vec{0}, t) e^{i\vec{k}_i \cdot \vec{r}_1} = \vec{E}(\vec{0}, t) e^{ikz_1}, \quad (1.45)$$

$$\vec{E}(\vec{r}_2, t) = \vec{E}(\vec{0}, t) e^{i\vec{k}_i \cdot \vec{r}_2} = \vec{E}(\vec{0}, t) e^{ikz_2}, \quad (1.46)$$

and since $\vec{E}(\vec{0}, t)$ may be unambiguously defined, the relative phase difference immediately follows. So, the incident field of particle j may be given by:

$$\vec{E}_j = E_0 e^{i(kz_{\text{local}} - \omega t)} e^{ikz_j} \hat{x}, \quad (1.47)$$

where the first exponential is the exponential used in (local) Mie theory, whilst the second is a phase difference picked up due to the global coordinates, which must be taken into account explicitly, separately from the Mie solution.

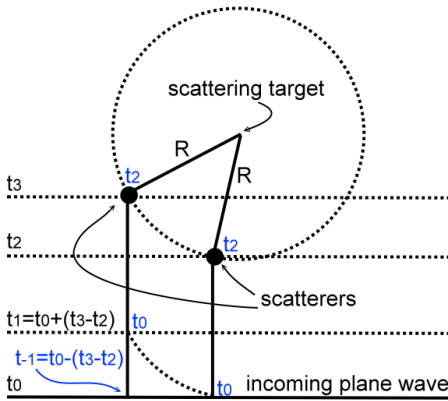


Figure 1.4: This figure helps in understanding the initial phase within Mie theory. The scattering target (e.g., a camera) is at a fixed identical distance from the two scatterers, such that the final phase need not be considered.

The (black) times on the very left show the times from the perspective of the Incoming Plane Wave (IPW). As expected, the wave does not arrive at the two scatterers at the same time.

The (blue) times shown at the 'events' are reverse-engineered times: If we are to measure at the scattering target at a fixed time, we cannot consider the IPW at the same time *and* at the same position simultaneously.

1.2. BLOOD

For a human to survive, his organs need to be given useful energy. Blood is the means for the human body to transfer all kinds of proteins and oxygen to the organs. Via white blood cells, the immune system too uses the blood to fight infections.

Blood consists of the yellow liquid blood plasma in which particles are dispersed: RBCs (erythrocytes), white blood cells (leukocytes) and platelets (thrombocytes). The hematocrit is about 45% (for men) [10], blood plasma occupies about 54.3% and white blood cells about 0.7%. Blood plasma consists of 92% water and 8% dissolved proteins, e.g., glucose. At 37°C, the resulting blood density is 1060 kg/m³ [11, 12].

For the present research, primarily the RBCs are of interest. These donut-shaped particles (see Fig. 1.5) are responsible for transporting oxygen through the body, which they acquire from the lungs.



Figure 1.5: This figure shows the shape of a RBC. It is a flexible oval biconcave disk, a donut-shape if you will. Its flexibility implies that it is able to change its shape as to be able to squeeze through smaller arteries.

The high volume fraction of particles causes blood to behave like a non-Newtonian fluid: it has a different rheology than simple water. In line with the theory of evolution, this adapted rheology increases the transport compared with what pure blood plasma would be able to do. The (dynamic) viscosity of blood is about $\mu_{\text{blood}} = 3$ to 4 mPa·s at 37°C. This is about a factor 4 more viscous than water ($\mu_{\text{water}} = 0.890$ mPa·s at 25°C) [13].

In this flow, there is a radial distribution for the RBC-concentration, as is measured by Aarts et. al. [14] and shown in Fig. 1.6. This distribution may be converted into a radial distribution for the particle number density, which may serve as a probability density function when injecting particles in a flow simulation.

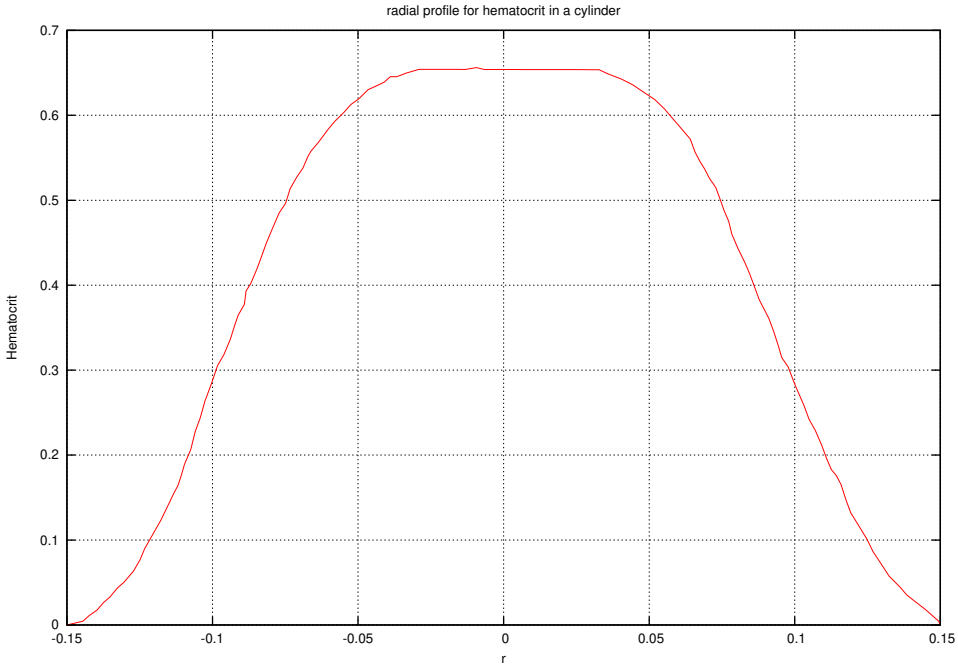


Figure 1.6: Radial hematocrit profile in a cylinder as measured by Aarts et. al. [14].

1.2.1. CONVERTING A VOLUME DISTRIBUTION TO A NUMBER DISTRIBUTION

If ϕ denotes the hematocrit, then we may write that in an infinitesimal thin cylinder surface (between r and $r + dr$):

$$\begin{aligned}\phi(r) &= \frac{dV_{\text{rbc}}(r)}{dV(r)}, \\ dV &= 2\pi r dr L, \\ dN(r) &= \frac{dV_{\text{rbc}}}{V_{1\text{rbc}}},\end{aligned}$$

where V denotes a volume, dN is the number of particles within the volume dV and L is the length of the cylinder. And thus:

$$\frac{dN(r)}{dr} = [\phi(r)r] \frac{2\pi L}{V_{1\text{rbc}}} \equiv NP(r), \quad (1.48)$$

where $P(r)$ is the probability density function for the particle number and N is the total number of particles within a cylinder of length L and radius R :

$$P(r) = \frac{\phi(r)r}{\int_0^R \phi(r)r dr}, \quad (1.49)$$

$$N = \frac{2\pi L}{V_{1\text{rbc}}} \int_0^R \phi(r)r dr. \quad (1.50)$$

Here, N is required to obtain the correct particle concentration, whereas $P(r)$ is required to obtain the correct radial particle distribution. For the present research, N is strongly limited by the computational resources and thus the required N cannot be achieved.

The cumulative particle distribution is then given by:

$$P(r \leq R_1) = \int_0^{R_1} P(r) dr. \quad (1.51)$$

which is useful for numerically converting a uniform distribution (as generated by the computer) to an arbitrary distribution, i.e., if $u \in U[0, 1]$, then we can find the r_{inj} at which to inject the particle by inverting the equation $P(r_{inj} \leq R_1) = u$. Fig. 1.7 illustrates this graphically.

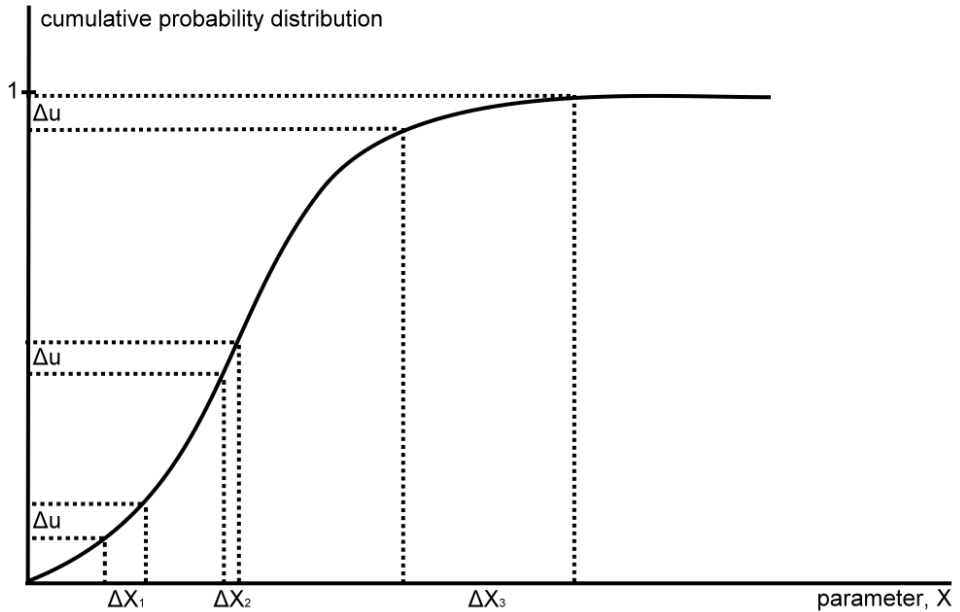


Figure 1.7: This figure shows a cumulative probability function, $P(x \leq X)$, for some parameter, x . The derivative of this function is the probability density function, i.e., the slope of this function is a measure for how probable x is: the steeper the function at some x_1 , the more likely that x_1 is chosen.

A random number $u \in U[0, 1]$ can then be mapped to the x -axis. It is shown that for some constant range Δu , the range Δx varies. Since all numbers in Δu are equally likely, this means that values for x are not equally likely.

In other words, $f(x) \equiv P(x \leq X)$ and since $f(x)$ is uniformly increasing, $P(f(x) \leq f(X)) = f(x)$. But if we take a random number $u \in U[0, 1]$, then $P(f(x) \leq u) = u$. It then follows that $P(x \leq X) = u$ for $X = f^{-1}(u)$, i.e., $x = f^{-1}(u)$ should be taken, when sampling for x using uniform numbers, to satisfy the required probability density function.

1.2.2. THE NAVIER-STOKES EQUATIONS AND RHEOLOGY

The equations of fluid dynamics to be solved are the [Navier-Stokes equations](#) for [incompressible flow](#), using the Newtonian model for the [stress tensor](#) [15]:

$$\frac{\partial u_i}{\partial x_i} = 0, \quad (1.52)$$

$$\frac{\partial u_i}{\partial t} + u_j \frac{\partial u_i}{\partial x_j} = \frac{1}{\rho} \left(-\frac{\partial P}{\partial x_i} + \frac{\partial \sigma_{ji}}{\partial x_j} + f_i^{\text{ext}} \right), \quad (1.53)$$

$$\sigma_{ji} = \mu \left(\frac{\partial u_i}{\partial x_j} + \frac{\partial u_j}{\partial x_i} \right), \quad (1.54)$$

where u_i is the velocity in the x_i direction, x_i denotes the i 'th coordinate: $x_i \in \{x, y, z\}$ for $i \in \{1, 2, 3\}$, ρ is the fluid density, μ the fluid viscosity, P is the pressure, σ_{ij} is the [deviatoric stress](#) tensor and f_i^{ext} represents the sum of all external forces per unit volume (e.g., gravity). The Einstein summation convention is employed³.

Blood does, however, not behave like a Newtonian fluid. Consequently, Eq. (1.54) should be replaced by a different constitutive relationship when a non-Newtonian fluid model is assumed (i.e., a different rheology). For the scope of the present research, a Newtonian model will be assumed nonetheless. For future research, non-Newtonian models for blood can be found in e.g. Merrill [16], who shows that blood behaves like a Newtonian fluid for high [strain rate](#) $\dot{\gamma} = \frac{\partial u_z}{\partial r} > 100 \text{ s}^{-1}$ (in cylindrical coordinates), but has an offset in its shear stress (i.e., the yield stress) for small strain rates with a different accompanying viscosity.

1.3. EXACT SOLUTION TO THE NAVIER-STOKES EQUATIONS

Whilst the Navier-Stokes equations Eqs. (1.52-1.54) are non-linear and there exists no general solution (as of today), it may still be solved exactly for some specific cases, typically for a well-defined simple geometry and a sufficiently low [Reynolds number](#).

The Reynolds number is the ratio of inertial forces and viscous forces and thus provides a measure for whether the flow is *inertia-dominated* (which will eventually result in [turbulence](#) at a sufficiently high geometry-dependent Reynolds number, e.g., about $Re > 4000$ for pipe flow) or *viscous-dominated* (which results in [laminar](#) flow for a sufficiently low Reynolds number):

$$Re \equiv \frac{UD}{\nu} = \frac{\langle u \rangle 2R}{\nu}, \quad (1.55)$$

where U is a typical velocity scale, D a typical length scale and ν is the kinematic [viscosity](#) of the fluid at hand. The second expression is in terms of the more common parameters used for pipe-flow: R is the radius of the pipe and $\langle u \rangle$ is the mean velocity:

$$\langle u \rangle \equiv \frac{\int u(r) da}{\int da} = \frac{\int_0^R u(r) r dr}{\int_0^R r dr}. \quad (1.56)$$

³In the Einstein summation convention, any repeated indices within the same term imply an inner product, e.g., $a_i b_i = a_1 \cdot b_1 + a_2 \cdot b_2 + a_3 \cdot b_3$. Singular indices represent a set of equations, being a set of three equations in the Navier-Stokes equations: one for each dimension.

1.3.1. PLUG FLOW

In case of a laminar unidirectional flow in an infinite environment, the velocity will simply remain constant in magnitude and direction:

$$\vec{u} = U\hat{z}. \quad (1.57)$$

This solution is called **plug flow**. In more realistic situations, this solution is still useful as a simplification. For example, in the case of flow inside a tube, there are several situations that approach plug flow [15]. (1) Nearby the entrance of a tube the velocity profile is still developing, approaching plug flow in its center. (2) In pulsatile flow, the flow profile is rather complex, but for a high Womersley number (see Sec. 1.3.3) the fluctuations become smaller, approaching plug flow. (3) For a non-Newtonian fluid, such as blood, the velocity profile is flattened in the center of the tube, which equals plug flow locally.

1.3.2. HAGEN-POISEUILLE FLOW

For the case of a cylinder of radius R , there exists an exact solution for the steady-state ($\frac{d\psi}{dt} = 0$) fully-developped ($\vec{u} = u(r)\hat{z}$, $P = P(z)$) profile. The result is the following:

$$\vec{u}(r) = \left(-\frac{dP}{dz}\right) \frac{1}{4\mu} (R^2 - r^2) \hat{z}. \quad (1.58)$$

Applying Eq. (1.56) to **Poiseuille flow** allows us to express the mean velocity, $\langle u \rangle$, in terms of the maximum velocity, $u_{max} = u(r=0)$. The result is that $u_{max} = 2\langle u \rangle$.

1.3.3. WOMERSLEY FLOW

The **Womersley flow** exact solution is similar to the Hagen-Poiseuille solution, but with the $\frac{d}{dt}$ -term included. For an arbitrary time-dependency of the pressure gradient, the solution $u(r, t)$ takes the form of an inverse temporal Fourier transform of the Fourier transform of $\frac{\partial P}{\partial z}$ multiplied by Bessel functions of the first kind and of zeroth order, J_0 . For a cosine forcing of frequency ω_0 , $\frac{\partial P}{\partial z} = \left|\frac{\partial P}{\partial z}\right|_{max} \cos(\omega_0 t)$, this inverse Fourier transform may be carried out, resulting in:

$$\begin{aligned} u(r, t) &= -\left|\frac{\partial P}{\partial z}\right|_{max} \frac{1}{\rho\omega_0} \left[A(r) \sin(\omega_0 t) + B(r) \cos(\omega_0 t) \right], \\ A(r) &\equiv \Re\{y(r/R)\}, \\ B(r) &\equiv \Im\{y(r/R)\}, \\ y(x) &= 1 - \frac{J_0(\alpha_0 i^{3/2} x)}{J_0(\alpha_0 i^{3/2})}, \end{aligned} \quad (1.59)$$

where $\alpha_0 \equiv \sqrt{\omega_0/\nu}R$ is the dimensionless **Womersley number** and ρ is the mass density of the fluid. This solution could be used to evolve Lagrangian particles (see Sec. 1.4) in a time-dependent cylindrical fluid flow, without requiring a **Computational Fluid Dynamics (CFD)** code.

1.4. LAGRANGIAN PARTICLE TRACKING (LPT)

To simulate particles with a subgrid size, [Lagrangian Particle Tracking \(LPT\)](#) is used. Particles are point-particles subject to forces and are evolved using Newton's law and some integration scheme. Defining $\vec{Y}(t)$ as the particle position, $\vec{V}(t) = \frac{d\vec{Y}(t)}{dt}$ as the particle velocity and $\vec{u}(\vec{x}, t)$ as the fluid velocity, and letting the subscript p refer to the particle and f to the fluid, the forces can then be written as [17, 18]:

- **Particle Inertia Force.** (left-hand side of Newton's equation) $\vec{F}_{in} = m_p \frac{d\vec{V}}{dt}$
- **Gravity and Buoyancy Force.** $\vec{F}_g = (m_p - m_f) \vec{g}$
- **Viscous Drag Force (Stokes).** $\vec{F}_d = -6\pi\mu R_p (\vec{V}(t) - \vec{u}(\vec{Y}(t), t))$
- **Pressure Force.** $\vec{F}_{pr} = m_f \left(\frac{D\vec{u}}{Dt} - \nu \nabla^2 \vec{u} \right) \Big|_{\vec{Y}(t)}$
- **Added-mass Force.** $\vec{F}_{am} = -\frac{m_f}{2} \frac{d(\vec{V}(t) - \vec{u}(\vec{Y}(t), t))}{dt}$
- **Basset/History Force.** $\vec{F}_B = \frac{R_p}{\sqrt{\pi\nu}} \int_{-\infty}^t \frac{d(\vec{V}(\xi) - \vec{u}(\vec{Y}(\xi), \xi))}{d\xi} \frac{d\xi}{\sqrt{t-\xi}}$

where $\frac{d\Psi}{dt} = \frac{\partial\Psi}{\partial t} + \vec{V} \cdot \nabla\Psi$ and $\frac{D\Psi}{Dt} = \frac{\partial\Psi}{\partial t} + \vec{u} \cdot \nabla\Psi$ for any Ψ . Which results in the following force equation for particle motion:

$$\vec{F}_{in} = \vec{F}_{pr} + \vec{F}_{am} + \vec{F}_d + \vec{F}_g + \vec{F}_B. \quad (1.60)$$

BIBLIOGRAPHY

1. Van As, K. *Interferometric Scattering of Light by an Ensemble of Flowing Spherical Particles: A Numerical Study* MA thesis (Delft University of Technology, 2015). <http://resolver.tudelft.nl/uuid:8dcdfd7c-d31d-4e70-a838-46441076bcb6>.
2. Mie, G. Beiträge zur Optik trüber Medien, speziell kolloidaler Metallösungen. *Annalen der Physik* **4**, 377–445 (1908).
3. Mie, G. Contributions to the optics of turbid media, particularly of colloidal metal solutions. *Royal Aircraft Establishment*. Translation of [2] (1976).
4. Mie, G. Contributions to the optics of turbid media, particularly of colloidal metal solutions. *Sandia Laboratories*. Translation of [2] (1978).
5. Wriedt, T. *Mie Theory 1908-2008, Introduction to the conference in Present developments and Interdisciplinary aspects of light scattering* (2008).
6. Van de Hulst, H. C. *Light Scattering by Small Particles* Dover. (Original work published 1957). ISBN: 978-0-486-64228-4 (Dover Publications, 1981).
7. Stratton, J. A. *Electromagnetic Theory* (McGraw-Hill Book Company, 1941).
8. Bohren, C. F. & Huffman, D. R. *Absorption and Scattering of Light by Small Particles* Wiley Professional Paperback. ISBN: 0-471-05772-X (John Wiley & Sons, Inc., 1998).
9. Barber, P. W. & Hill, S. C. *Light Scatter by Particles: Computational Methods* Wiley Professional Paperback. (Original work published 1990). ISBN: 9971-50-832-X (World Scientific Publishing Co. Pte. Ltd., 1998).
10. Purves, W. K., Sadava, D., Orians, G. H. & Heller, H. C. *Life: The Science of Biology* 7th, 954. ISBN: 0-7167-9856-5 (Sunderland, Mass: Sinauer Associates, 2004).
11. Shmukler, M. *Density of Blood* (The Physics Handbook, 2004).
12. Cutnell, J. & Johnson, K. *Physics* Fourth, 308 (Wiley, 1998).
13. Elert, G. *Viscosity* (The Physics Hypertextbook, 1998).
14. Aarts, P. A. M. M. *et al.* Blood Platelets are Concentrated Near the Wall and Red Blood Cells, in the Center in Flowing Blood. *Arteriosclerosis* **8**, 819–824 (1988).
15. Kundu, P. K., Cohen, I. M. & Dowling, D. R. *Fluid Mechanics* Fifth, 110–114 (Elsevier, 2012).
16. Merrill, E. W. Rheology of Blood. *Physiological Reviews* **49**, 863–888 (1969).
17. Corssin, S. & Lumley, J. On the equation of motion for a particle in turbulent fluid. *Appl. Sci. Res. (A)* **6**, 114–116 (1956).
18. Maxey, M. R. & Riley, J. J. Equation of motion for a small rigid sphere in a nonuniform flow. *Phys. Fluids* **26**, 883–889 (1983).

2

DESCRIPTION OF THE ALGORITHM/CODE

Based on *Mie theory* (Sec. 1.1), we have designed and implemented an algorithm¹ to compute the light scattered by an ensemble of particles. Thus given an incoming *plane wave* and given a certain configuration of *scatterers*, the optics code should compute the intensity profile as measured by a given distant camera. This computed intensity will be independent of time, unlike the instantaneous intensity, as will be discussed in Sec. 2.1.2.

In *in-vivo* blood flow, these scatterers (*RBCs*) are moving as a function of time in the arteries, requiring us to study dynamic light scattering. To that end, the optics code must be executed repetitively for each timestep, and the results combined to mimic a measurement of an actual camera.

The optics code will use the result of a separate fluid dynamics code, which evolves the particle positions over time, as its input. A separate code will take care of the coupling of the two codes, such that any *Computational Fluid Dynamics* (*CFD*) code can be used as an input to our optics code.

This chapter briefly describes the assumptions and the functionality of the optics code (Sec. 2.1), the fluids code (Sec. 2.2) and the coupling code (Sec. 2.3). A detailed description of the codes is delegated to App. B. Evidently, some approximations were to be made; the effects of which will also be discussed. Subsequently, Chap. 3 will show a validation study for the optics code.

A large part of this chapter was published previously: Van As, K. (2015). *Interferometric Scattering of Light by an Ensemble of Flowing Spherical Particles: A Numerical Study* [Master's Thesis, Delft University of Technology].

[1] Available online via <http://repository.tudelft.nl>.

¹Our code described in this chapter has been published open-source, see the [List of Publications](#) on page 137.

2.1. OPTICS

The optics code² is responsible for simulating **Laser Speckle Imaging (LSI)**, i.e., computing the **intensity** profile at a given camera for a given incoming **Plane Wave (PW)** and a given distribution of spherical **scatterers**. The computation will be performed in an **interferometric** manner, i.e., the phase will carefully be taken care of for each individual trajectory.

Currently, two codes have been created: **Single-Scattering Far-Field (SSFF)**, which only takes single scattering into account, and **Multi-Scattering Far-Field (MSFF)**, which takes **multiscattering** into account without any statistical averaging, which is an extension to the **SSFF** code. In either case, a **FF** assumption is made for the distance between the scatterers.

2.1.1. THE MIE ALGORITHM

As a starting point, the Bohren & Huffman Mie code ('bhmie') has been used, which accompanies their book [2]. Their code has been written in F77 (Fortran). Their code computes the **amplitude scattering matrix** as a function of the **scattering angle**, $[S](\theta_s)$, for a single homogeneous sphere. The scattering angles necessarily are a sequence of evenly spaced scattering angles between 0° and 180° . Additionally, it also outputs some θ_s -averaged quantities, like the extinction efficiency. The only input parameters required by bhmie are the **size parameter**, x , and the relative **refractive index**, m (see Eq. (1.28) and the text just above it).

This code has been adapted to take as an argument an array of arbitrary scattering angles.³ Then, any computed quantities which are not required for the present study (like the extinction efficiency), we have removed from the code.

In bhmie, $[S]$ is computed cf. Eq. (1.40), which is an infinite sum. This sum is truncated at the index n_C , which has been found empirically:

$$n_C = \text{round}\left(x + 4x^{\frac{1}{3}} + 2\right), \quad (2.1)$$

where x is the size parameter of the sphere. This heuristic was proposed by Wiscombe in 1979 [3, 4] and is merely a given wisdom in Bohren & Huffman's book. The **Bessel/Hankel functions** and **Legendre polynomials** are computed using recursion relationships, given the exact (or asymptotic) value for some index. The book of Barber & Hill nicely summarises all these, and more, computational techniques for easy reference [5].

2.1.2. THE EXTENDED ALGORITHM (CAMERA, MULTISCATTERING)

Fig. 2.1 shows qualitatively what the algorithm is expected to do. Briefly, an incoming **PW** is scattered by each particle to each other particle. In the very-**FF** these scattered fields are again **PWs**, and thus the exact same equations may be used to scatter those fields again by each particle to each other particle. Ad infinitum. I will refer to these iterations as "**scattering orders**".

²Our code described in this chapter has been published open-source, see the [List of Publications](#) on page 137.

³Actually, the cosine of the scattering angles, since the scattering angle only appears as a cosine in the algorithm.

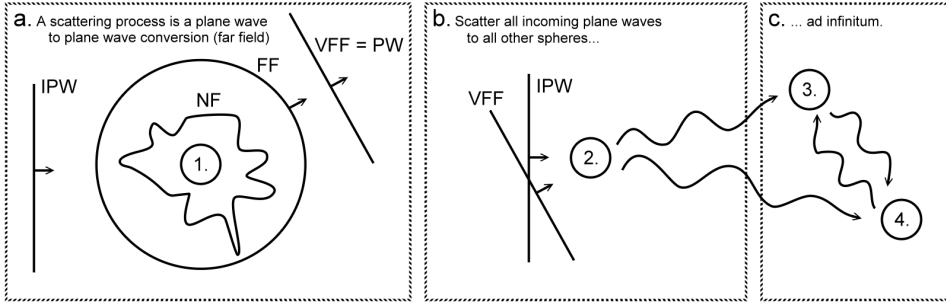


Figure 2.1: The figure shows the workflow of the algorithm in an animated manner. In (a), there is an incoming **Plane Wave (PW)** (IPW) incident on the spherical scatterer labelled '1', which will scatter. In the **Near-Field (NF)**, this gives a very complex scattered field as described by Mie theory Eq. (1.40). In the **Far-Field (FF)**, this may be approximated by a spherical wave (which is still a function of the scattering angle), which in the very-FF may be approximated as a **PW**.

In (b), a second scatterer is illuminated by both the scattered **PW** and the original incoming **PW**, which will again result in a **PW** in the very-FF. In this manner, each scatterer can scatter each wave to each other scatterer, until convergence.

In (c), it is noted that this scattering process may continue ad infinitum when it is performed in the described iterative manner.

Fig. 2.2 illustrates what the scattering order means. It also discriminates between three distinct regions in the multiscattering-process, which are to be treated differently. In initialscatter, the **IPW** is involved, which can be interpreted as the start-up of the multiscattering part of the code. In multiscatter, the scattered field from each particle, l , is used as an **IPW** for each particle, i , and is to be scattered to each particle, j , where $l \neq i$ and $i \neq j$. Note that the figure does not show the “from each particle, l , to each particle, j , via each other particle, i ”-process, but rather shows exactly one l , one i and one j (Fig. 2.3 will help with that, as will be described below). Lastly, in scatter2cam, the scattered fields from each particle of all scattering orders are scattered towards *every pixel* of the camera, accumulated, and the intensity is computed. Finally, add some **I/O** around these three routines and the entire optics code has been described.

From a mathematical point of view, the algorithm is structured as follows. Using that fields add up arithmetically and using the Mie algorithm with the **FF** approximation applied (cf. Eq. (1.44)), which gives the scattered field given an **IPW**, we have:

$$\tilde{E}_j^p = \sum_{i \neq j} \tilde{E}_{ji}^p, \quad (2.2)$$

$$\tilde{E}_{ji}^p = \sum_{l \neq i} \tilde{E}_{jil}^p, \quad (2.3)$$

$$\tilde{E}_{jil}^p = [S]_{jil} \tilde{E}_{il}^{p-1} \frac{\exp i \Delta \varphi_{ji}}{-i k z_{ji}}, \quad (2.4)$$

where \tilde{E} is the (electric) field, p denotes the scattering order, $\{l, i, j\}$ are indices which denote the three scatterers involved, $\Delta \varphi_{ji} = k z_{ji}$ is the phase picked up from moving from particle i to j , z_{ji} is the distance between particles i and j . The sums over l and i are in words: “for each **IPW** (originating from particle l), via each other particle i , scatter

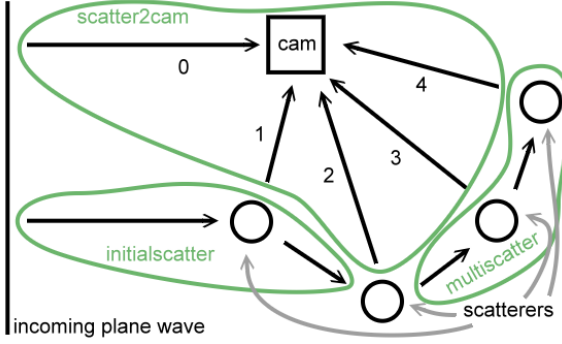


Figure 2.2: This figure illustrates what the scattering order, p , means. Zeroth order scattering is the direct arrival of the incoming PW on the camera. Any order above that is the number of scatterers the field has ‘seen’ before reaching the camera.

The figure also identifies three distinct regions in the multiscattering-process which each require a slightly different algorithm, as described in the text.

Evidently, every scattering order has many more contributions than is shown in the present figure.

to particle j ”. $[S]$ is the amplitude scattering matrix, which is the output of the blmie algorithm of Sec. 2.1.1 with as input the scattering angle. $[S]$ thus depends on all three indices, because it takes three points to span an angle. Combining the equations and rearranging terms, it follows that:

$$\vec{E}_j^p = \sum_{i \neq j} \frac{\exp i\Delta\varphi_{ji}}{-ikz_{ji}} \sum_{l \neq i} [S]_{jil} \vec{E}_{il}^{p-1}, \quad (2.5)$$

where it is noted that the spherical wave term could be taken out of the sum. This equation is to be interpreted as an iterative equation which takes us up one scattering order.

Eventually, every scattering order needs to be scattered to every pixel, c , of the camera, as depicted in Fig. 2.2. Since fields add up arithmetically, this becomes:

$$\vec{E}_c = \sum_p \vec{E}_c^p, \quad (2.6)$$

where \vec{E}_c^p is found from Eq. (2.5) by setting $j = c$ (because a scattering target needs not be sphere j , but might as well be pixel c). Bringing everything together and rearranging terms, we then find:

$$\vec{E}_c = \vec{E}_c^0 + \vec{E}_c^{\text{scattered}} = \vec{E}_c^0 + \sum_i \frac{\exp i\Delta\varphi_{ci}}{-ikz_{ci}} \sum_{l \neq i} [S]_{cil} \sum_{p=1}^{\infty} \vec{E}_{il}^{p-1}, \quad (2.7)$$

where \vec{E}_c^0 denotes the IPW at the position of pixel c . Be careful not to omit the phase of the IPW which is hidden within \vec{E}_c^0 , cf. Eq. (1.47). The term \vec{E}_{il}^{p-1} , is the result of the multiscattering-process, cf. Eq. (2.3) (after changing indices), with the IPW as its starting point: $\vec{E}_{il}^{1-1} \equiv \vec{E}_i^0$ (using the phase belonging to the position of the sphere). Note that when the equation is written in this manner, $[S]_{cil}$ is only needed exactly once. “This manner”, implies that we can scatter an accumulated field from each sphere, i , to each pixel, c , where the accumulated field is:

$$\vec{E}_{il}^{\text{accum}} = \sum_{p=1}^{\infty} \vec{E}_{il}^{p-1}. \quad (2.8)$$

This will save both computational time and RAM.

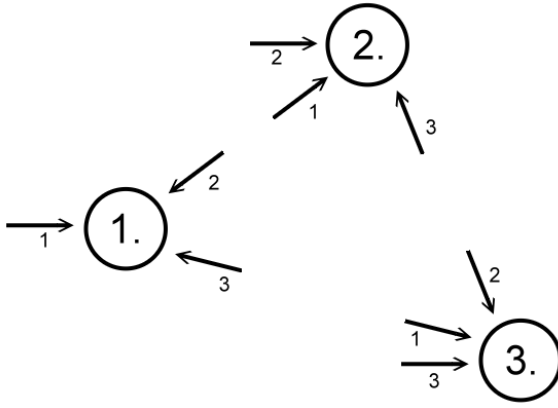


Figure 2.3: This figure illustrates all interactions between particles. The numbers denote the ‘source’ of the arrow, with the incident field referred to as the number of the sphere (since that index was unused anyway). These numbers may be used as indices to store \vec{E}_{il} , as used in the algorithm. So, in an OOP-manner, within each sphere i , N_l fields are stored. The result is a Lattice-Boltzmann-like memory storage, in analogy with fluid dynamics.

Fig. 2.3 shows three spheres with all their required interactions (excl. camera). Within the shown arrows, information may be stored. In Fig. 2.1b two fields incident on particle 2 were shown. Those incident fields were called \vec{E}_{il} in e.g. Eq. (2.5). Now, for each sphere, i , we may store this field in arrow l . Given the equations, we need to store three fields within each arrow: \vec{E}_{il}^{p-1} , \vec{E}_{ji}^p and $\vec{E}_{il}^{\text{accum}}$. The first is the result of the previous iteration, ‘old’, the second is what is currently being computed, ‘new’, and the third is the accumulator used to scatter to the camera once the multiscattering-process has converged.

Finally, the intensity on the camera has been computed as

$$I_c = |\vec{E}_c|^2 = \vec{E}_c^* \vec{E}_c, \quad (2.9)$$

where I_c is the intensity in pixel c , and \vec{E}_c is the complex electric field, cf. Eq. (2.7). Strictly speaking, $I_{\text{true}} \propto I_{\text{computed}}$, depending on, e.g., the calibration of the physical camera. Note that this is a time-averaged intensity. The instantaneous intensity would scale with $\cos^2(\phi_0 + \omega t)$, which averages out to a simple constant of proportionality.

Note that Eq. (2.7) is equivalent to the Lippmann-Schwinger equation for quantum scattering problems [6], and the used infinite series expansion is equivalent to the Born scattering series [7]. Deploying known solution methods to the Born series, could in future work yield an alternative method of solving our equation [8, 9].

2.1.3. MEMORY REQUIREMENT OF THE ALGORITHM

Let N denote the number of particles, then from Eq. (2.5) it follows that we require

$$8\text{bytes} \cdot \left(\left(\underbrace{1/2}_{\text{sym. in } l \& j} \right) \left(\underbrace{2}_{S1, S2} \right) \left(\underbrace{N-1}_{N_i} \right) \left(\underbrace{N}_{N_i} \right) \left(\underbrace{N-1}_{N_j} \right) \right) = O(8N^3) \text{ bytes} \quad (2.10)$$

memory to store $[S]$, which may be reduced by $O(N^2)$ by noting that the [backscattering](#) matrix is a constant for a given sphere i , and

$$8\text{bytes} \cdot \left(\left(\underbrace{3}_{3D} \right) \left(\underbrace{3}_{\text{new\&old\&accum}} \right) \left(\underbrace{N}_{N_j} \right) \left(\underbrace{N}_{N_i \& IPW} \right) \right) = 72N^2 \text{ bytes} \quad (2.11)$$

to store the fields (cf. Fig. 2.3). The **interparticle distance**, \tilde{z}_{ji} , needs not be stored as it is computed with just one (vectorised) subtraction, which is negligible compared to `bhmie`. Its amplitude requires Pythagoras, but is still very much negligible and not worth complicating the code for.

Note that there is as well a scattering matrix to scatter from particle l , via particle i , to camera pixel c . Which would require require $O(16MN^2)$ bytes, similar to Eq. (2.10) without the symmetry, and where M is the number of pixels. Since there are already 10^4 pixels to have a 1D resolution of 100 pixels, this is typically higher than N for realistic computations. Sadly, for $M = 100^2$ and $N = 1000$ this results in 160GB, which is too demanding for the **RAM**. However, as was noted using Eq. (2.8), it needs not be stored in **RAM**, since it is only required once. Instead, $8 \cdot O(3MN)$ bytes will be stored during `scatter2cam` for computational efficiency of `bhmie`, i.e., `bhmie` is faster if performed in a batch-process, because it can reuse its Bessel functions and Legendre polynomials. Calling `bhmie` requires an additional amount of **RAM** equal to $8 \cdot O(4MN)$ bytes, resultig in a total of $O(56MN)$ bytes.

As an example calculation, using 1000 particles and $300 \cdot 300$ pixels, we would require approximately 8GB of **RAM** during the `multiscatter` routine. And during the `scatter2cam` routine, we would require 2.2 GB, which occasionally spikes to 5 GB. Or, using 602 particles and $300 \cdot 300$ pixels, we require 1.8GB during `multiscatter` and 1.3 GB spiking to 3 GB during `scatter2cam`. Note that the memory requirement of the first example is particle-limited, whereas the second becomes pixel-limited. Since both cases are realistic, one should consider both routines when determining the memory requirement for a given case.

2.1.4. RUNTIME COMPLEXITY OF THE ALGORITHM

The algorithm is structured in three phases, which were shown in Fig. 2.2. Each of these contributes to the runtime **complexity** of the algorithm, which describes how the runtime of the algorithm scales with the input size at sufficiently large input sizes.

In the `initialscatter` routine, `bhmie` first is called exactly once using a vector size of $N - 1$ to scatter the incident field from the first to the second sphere, which is negligible. Then it is called N times to prepare for the `multiscatter` routine using a vector size $N(N - 1)$. Additionally, there is a loop over j and i , $O(N(N - 1))$, which performs virtually the same calculations as the `multiscatter` routine.

In the `multiscatter` routine, at its top level, the algorithm consists of four loops, as shown in Alg. 3 of App. B.2. The inner loop is ran a total number of $pN(N - 1)(N - 1)$ times, and has a complexity of $O(1)$. This results in a complexity of $O(pN^3)$.

Table 2.1: Summary of all runtime complexities involved in the individual routines of the algorithm.

	Loop work	Call <code>bhmie</code>	Total
<code>initialscatter</code>	N^2	$N \times N^2 n_C$	$N^3 n_C$
<code>multiscatter</code>	pN^3	-	pN^3
<code>scatter2cam</code>	MN^2	$N \times MN n_C$	$MN^2 n_C$
Total	$N^2(M + pN)$	$N^2 n_C(M + N)$	$N^2(Mn_C + N(n_C + p))$

In the `scatter2cam` routine, `bhmie`, again, is called N times, but now with a vector size of $M(N - 1)$. Then, Eq. (2.7) is performed, requiring $O(N(N - 1))$ operations (recall that \sum_p was accumulated in `multiscatter`, cf. Eq. (2.8)). This is to be done for each pixel, c , resulting in a complexity of $O(MN^2)$.

The complexity of `bhmie` is $O(n_C n_\theta)$, where n_C is the truncation index of the infinite sum from [Mie theory](#) and n_θ is the vector size as used above (which is the number of scattering angles).

The accumulated result is summarised in Tab. 2.1, neglecting lower order terms. Please note that complexities are frequently misinterpreted. They describe the behaviour of a code in the limit that the parameters of the complexity (N , M , ...) go to ∞ . For practical cases, it may very well be that the neglected lower order terms do in fact contribute significantly more to the required computational resources, simply because they have a greater constant of proportionality than the higher order terms.

2.1.5. SPEEDUP BY APPROXIMATING THE SCATTERING MATRIX

The `bhmie` routine, which performs the expensive calculation of computing the scattering matrix for one scattering angle, is called a total number of $N^2(M + N)$ times (see Tab. 2.1). It is easily seen that for merely $N = 100$ particles and a camera with just $M = 100 \times 100$ pixels, these are already $O(10^8)$ calculations. Therefore, it came to no surprise that in our example application $\sim 90\%$ of the runtime of our code was spent inside the `bhmie` routine. This means that optimising everything but `bhmie` may yield a speedup of maximum $\sim 11\%$; therefore, the only way to achieve a good speedup of up to a factor 10, is to optimise the `bhmie` routine. This is an example of the 3%-scenario Donald Knuth was talking about⁴:

*We should forget about small efficiencies, say about 97% of the time:
premature optimization is the root of all evil.*

– Donald Knuth

Fig. 2.4 visualises what the elements of the scattering matrix as a function of the scattering angle look like for the parameters that we will use in Chap. 4. In particular, in the bottom-right figure one may count ~ 50 fluctuations over the entire domain of the function. As an approximation, we could divide each fluctuation in 20 points – thus the entire domain in 1000 points – and only compute the scattering matrix at those points. The scattering matrix for all other input angles may then be found through linear [interpolation](#)⁵.

The gain of this interpolation strategy, is that we would now only need to call `bhmie` $O(10^3)$ times, as opposed to the example above of $O(10^8)$ times. This yields an *immense* speedup at virtually no loss of accuracy⁶, effectively eliminating the computational time spent on `bhmie`. Since, in the example of our application, 90% of our time was spent on this, our code speeds up by approximately a factor ~ 10 as a consequence.

⁴I.e., optimising parts of your code that yield a negligible gain should be avoided at all times, because you pay the price of making your code less clear and less maintainable, while you gain *nothing* for that pain!

⁵To yield more accurate interpolations, higher order interpolation schemes may be implemented in the future.

⁶If one is worried about the interpolation accuracy of 10^3 points, 10^4 points could as well be used for virtually the same total computational time, as $10^4/10^8 \ll 1$ still.

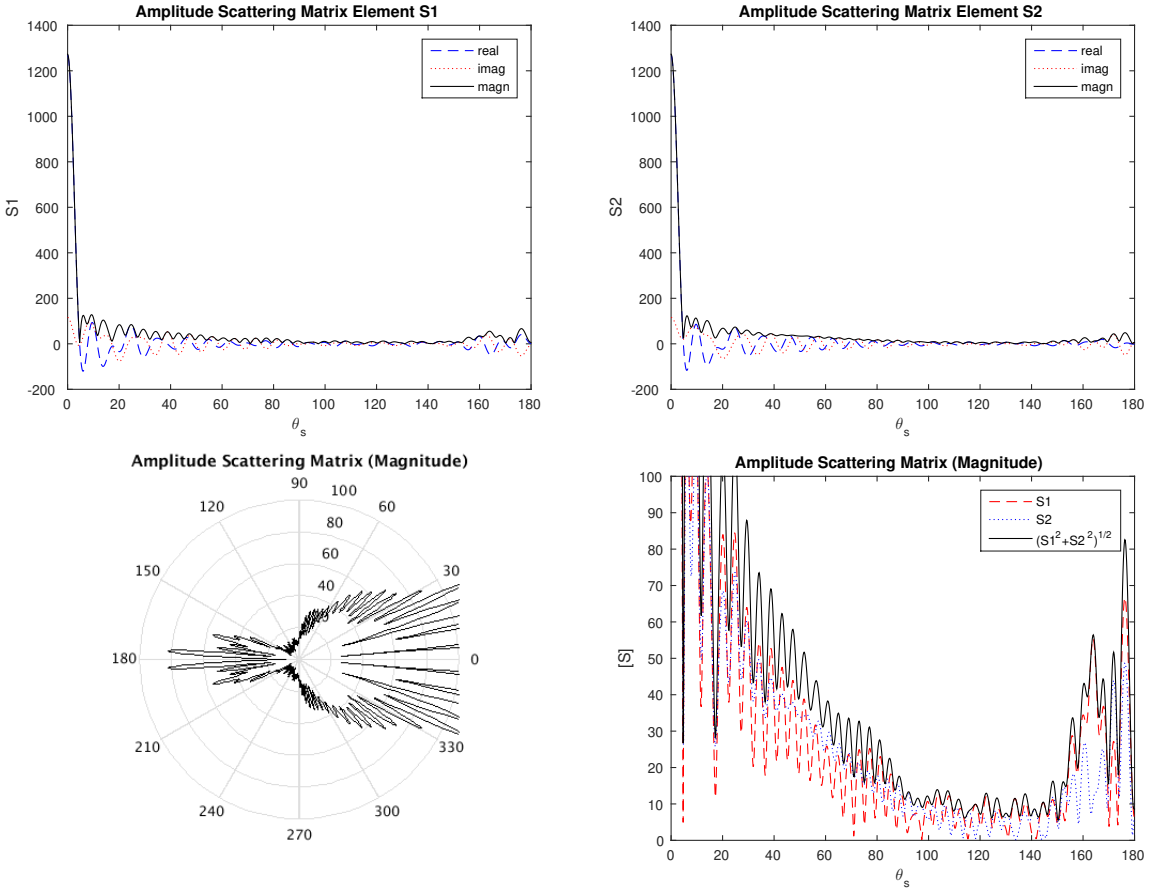


Figure 2.4: The amplitude scattering matrix elements S_1 and S_2 cf. Eq. (1.40) are shown as a function of the scattering angle. The used parameters are: relative refractive index $m = 1.52$ (in Eq. (1.28)), wavelength $\lambda = 532\text{nm}$, particle radius $a = 4\mu\text{m}$, and size parameter $x \approx 47$. The bottom-right figure provides a zoomed-in version of the magnitudes, leaving out the huge forward scattering peak. The bottom-left figure plots $\sqrt{S_1^2 + S_2^2}$ in a polar plot.

Finally, note that this interpolation strategy yields a very good speedup *only* since the scattering matrix depends on *just one* input parameter: the scattering angle. If, in the future, non-spherical particles [10] or particles with differing optical properties would be considered, the scattering matrix will become a multivariate function. With two input parameters interpolation should still be possible, but a lower speedup will be attainable.

New memory and runtime complexities. Note that, whilst our code does indeed speed up considerably, the runtime complexity (see Sec. 2.1.4) remains $O(N^2(M + pN))$ to perform all loop work. The memory requirement (see Sec. 2.1.3) does improve, as we now only need to store the scattering matrix in 10^3 points, as opposed to for $O(N^3)$ input

values. The resulting memory complexity then becomes $72N^2$ bytes, cf. Eq. (2.11), to store the electromagnetic fields, which for $N = 10^3$ is a negligible RAM requirement.

2.1.6. CONVERGENCE OF THE ALGORITHM

In general, the study of convergence of an algorithm is a difficult one. Instead, a seemingly sufficient condition is relatively easily seen from Eq. (2.4). If that equation is not to diverge as a function of the scattering order, p , we require that

$$k\lambda > \max_{\theta_s} ([S](\theta_s)), \quad (2.12)$$

which right away gives a measure of how far the FF ought to be for convergence of the FF-approximation. Satisfying this condition will be a sufficient condition, provided that the sum in Eq. (2.3) does not grow out of bounds. This is guaranteedly satisfied if

$$k\lambda > N \max_{\theta_s} ([S](\theta_s)) \quad (2.13)$$

holds, but for randomly distributed particles it is easily seen that this is an extremely strong condition, since this condition assumes that all particles are distributed such that their scattering angles give a maximum $[S]$ for all particles. Fig. 2.4 show what the amplitude scattering matrix looks like as a function of the scattering angle, θ_s . Clearly, for most values of θ_s , $[S]$ is a factor $O(10^2)$ lower than its maximum value.

With that being said, Eq. (2.13) is certainly too strong, but even Eq. (2.12) appears to be strong in terms of convergence, because if it is not satisfied for some spheres, the algorithm may still converge numerically, although it becomes more difficult. However, the algorithm numerically converging is not the same as the convergence of the algorithm to the true solution. If the electric field is to increase in strength in any scattering event, it becomes difficult to believe that conservation of energy is satisfied. However, this is paradoxical, since it is allowed for the electric field to increase in strength in one direction, as long as it decreases in another (which is a direction which was not of interest and was thus not considered).

Regardless, Eq. (2.12) should yield a practical sufficient condition, although its sufficiency cannot be guaranteed in general.

2.1.7. APPROXIMATIONS AND THEIR CONSEQUENCES

Spherical Particles. The first approximation made, is the fact that we assume that RBCs may be approximated by spherical scatterers. Steinke and Shepherd [11] have shown that Mie theory can successfully be applied to randomly-oriented RBCs. Evidently, RBCs in blood flow will have a preferential alignment. Nilsson et. al. [10] observe a single RBC using the T-matrix method and found that the forward-scattering peak of a sphere is lower and broader than for oblate spheroids (which is still not the precise shape of a RBC, but it is closer to its true shape than a sphere). In other words, the amplitude scattering matrix, $[S]$, is affected by the shape of the particles. Also, an azimuthal-dependency is introduced, which is absent for the case of a sphere. Based on their numerical study of a single particle, they conclude that it 'seems inappropriate' to use the spherical Mie theory to study RBCs. Especially if fundamental hematological and morphological properties of RBCs are of interest. Nevertheless, at the same time one

would expect that if the particles are dense enough (and RBCs in blood are dense with a typical hematocrit of 45%, see Sec. 1.2), multiscattering will blur the precise shape of [S], making the spherical assumption statistically more valid.

If the spherical assumption is not to be made, one could attempt implementing the T-Matrix method, as described in Barber & Hill [5]. For time-dependent simulations with $O(1000)$ particles, however, this will bring along a steep increase in the required computational resources.

Infinite Series Truncation. Now that we have chosen spherical scatterers, the exact Mie solution may be used to solve the scattering of an IPW by a single scatterer. There are no further assumptions inside Mie theory: it is exact. However, it is exact using an infinite series representation, which enforces it to be approximated (truncated) if it is to be evaluated. The series is truncated after n_C terms, cf. Eq. (2.1). Regardless of how accurate this truncation is, the other approximations made will certainly be more questionable than truncating this series.

A similar problem lies within the computation of the Bessel/Hankel functions and Legendre Polynomials, required by Mie theory: They are computed using recursion, which has the consequence that any rounding errors will eventually blow up. For this reason, Bohren & Huffman [2] explicitly warn their reader not to ‘simply’ increase n_C , as you may unknowingly make your simulation less accurate.

Far-Field Assumption. Three FF-assumptions have been made: (1) the camera is in the FF, (2) the particles are in each other’s FF and (3) particles are sufficiently small for the spherical wave to be a PW over the size of the particle. Given the second assumption, the first assumption is an obvious assumption. The second and third assumptions require elaboration.

Starting with (3), mathematically this is the question of whether a spherical wave has a constant amplitude over the size of a particle and is thus a simple PW. A stronger version yet would be to say that the field is constant altogether (no longer a wave) over the size of the particle, which we will observe first.

A spherical wave, moving outwards from the origin, is given by (the real part of):

$$\Psi(r) = \frac{e^{ikr}}{kr}, \quad (2.14)$$

where the factor $e^{-i\omega t}$ has been omitted. Now, if R denotes the *constant* distance between the source of Ψ and the particle under consideration (as before) and δ is the radius of the particle, then $\Psi(R + \delta)$ (at the particle’s boundary) may be expressed in terms of $\Psi(R)$ (at its center). Applying a Taylor expansion to $\Psi(R + \delta)$ around $\delta R/R = 0$, and deploying Newton’s binomial theorem, gives:

$$\Psi(R + \delta) = \Psi(R) \sum_{n=0}^{\infty} \frac{(\delta/R)^n}{n!} \sum_{j=0}^n \binom{n}{j} (ikR)^{n-j} (-1)^j j! \quad (2.15)$$

$$\approx \Psi(R) \left(1 + \frac{\delta R}{R} (ikR - 1) + \left(\frac{\delta}{R} \right)^2 \left(\frac{1}{2} (ikR)^2 - ikR + 1 \right) \right). \quad (2.16)$$

The physical property is the real part of this complex function, which is approximately:

$$\operatorname{Re}\{\Psi(R+\delta)\} \approx \operatorname{Re}\{\Psi(R)\} \left(1 - \frac{\delta}{R}\right) - \operatorname{Im}\{\Psi(R)\} k\delta, \quad (2.17)$$

and consequently equality implies that $\frac{\delta}{R} \ll 1 \cap k\delta \ll 1$. Recall that these conditions describe the situation in which the particle is so small, that even the **phase** is constant on the length scale of the particle. Recalling Eq. (2.12), which gives a sufficient condition for convergence, the conditions may be rewritten as

$$\frac{\delta}{R} \ll 1 \quad \cap \quad \max(|S|) \frac{\delta}{R} < kR \frac{\delta}{R} = k\delta \ll 1. \quad (2.18)$$

Given a typical value of $\max_{\theta_s}(|S|(\theta_s)) \approx 10^3$ (size parameter $x = 42$ and refractive index $m = 1.52$), it follows that the second condition is *at least* a factor 10^3 stronger than the first for the present parameters.

Tracing back, we can say something about the weaker assumption made in (3), which assumed a **PW** rather than a constant field, as was studied above:

$$\Psi(R+\delta) \approx \frac{e^{ik(R+\delta)}}{kR} \left(1 - \frac{\delta}{R} + \left(\frac{\delta}{R}\right)^2\right), \quad (2.19)$$

where solely the reciprocal has been expanded. From this it is seen that a spherical wave may be written as a plane wave if $\frac{\delta}{R} \ll 1$, which interestingly was the weaker part of above condition for a constant field. From Eq. (2.19) it is easily seen that the relative error made *in the wave function* is approximately $\frac{\delta}{R}$. E.g., if $\frac{\delta}{R} = 0.1$, a 10% error is made, *in the wave function*.

Regarding (2), saying that the particles are in each other's **FF** is saying that the inter-particle distance should be much greater than a characteristic length. Mathematically, this boils down to the question if it is justified to take the asymptotic value of the Hankel functions in Mie theory. The expansion of the spherical Hankel function for big $z \equiv k\lambda$ is given by:

$$h_n^{(1)}(z) = e^{iz} \left(-\frac{ie^{-\frac{1}{2}in\pi}}{z} + \frac{e^{-\frac{1}{2}in\pi} n(n+1)}{2z^2} + O(z^{-3}) \right), \quad (2.20)$$

$$= (-i)^n e^{iz} \left(\frac{1}{iz} + \frac{n(n+1)}{2z^2} + O(z^{-3}) \right), \quad (2.21)$$

which immediately shows that $h_n^{(1)}(z)$ becomes independent of n for big z , and hence could be taken out of the sum in Mie theory. Sadly, the second term scales with n^2 and n is an index that runs until ∞ , so z must be a greater ∞ than n .

This problem is resolved by observing the full Mie sum, cf. Eq. (1.40). Ignoring the coefficients a_n and b_n and the Legendre functions, it is proportional to $\frac{2n+1}{n(n+1)}$. Consequently, the importance of the terms drops as $\frac{2}{n}$ for big n . So, while indeed the Hankel functions do not converge to the first term in the expansion for all n as z grows big, the series no longer cares about those Hankel functions.

To make this FF-assumption more quantitative, we note that the series will be truncated at n_C , cf. Eq. (2.1). If it is again assumed that the terms in the Mie series are equally important for all n , then we obtain a very worst case estimate of what FF means:

$$z \gg \frac{n_C(n_C + 1)}{2}. \quad (2.22)$$

For $\lambda = 6 \cdot 10^{-7}$ m and $r_{\text{sph}} = 4 \cdot 10^{-6}$ m, this results in $z \gg 0.16$ mm. Again, this is a very worst case requirement. A lower z may very well be feasible. If a_n and b_n would be taken into account, which is difficult to do generally, the requirement will soften.

The speed of light is much greater than the fluid speed. It is assumed that the speed of light is much greater than the velocity of the particles (and thus the fluid). The consequence of this assumption is that it is not required to consider the retarded time: the instantaneous time suffices. If this assumption is not made, the position of the scatterers would need to be backtracked to the time at which they scattered the light, rather than taking the current snapshot of all positions.

If this assumption is not satisfied, an error will be made in [S] for each scattering event, because the used scattering angles ($\{\theta_s\}$) will be incorrect. Also, an error will be made in the phase, since the calculated pathlength of the light may differ from the true ones. The first error is difficult to analyse, since the fluctuations in [S] as function of θ_s are a very complex function of the parameters of Mie theory (x, m). The second error may be analysed by noting that the maximum error in the phase occurs when the particle moves in the direction of \vec{k} . If the velocity of a particle is v , then in a time Δt , the phase changes according to (with $z = z(t)$):

$$\begin{aligned} \phi(t) &= kz - \omega t = k(z - ct), \\ \phi(t + \Delta t) &= k(z + v\Delta t - c(t + \Delta t)) \\ &= \phi(t) + k(v - c)\Delta t \\ &= \phi(t + \Delta t)|_{v \ll c} + kv\Delta t. \end{aligned} \quad (2.23)$$

From which it follows that $kv\Delta t \ll 2\pi$ is the criterion which justifies the assumption. Now, note that the Δt of interest is the time it takes the light to travel from the light source to the camera, as this is what was assumed to be instantaneous: $\Delta t_{\text{max}} = z_{\text{max}}/c$. The value for z_{max} is technically infinite, because of the multiscattering-process. However, since each successive scattering order contributes less than the previous one to the final result, the series is truncated. A typical measure for z_{max} would then be:

$$z_{\text{max}} = O(|\vec{r}_{\text{cam}} - \vec{r}_{\text{CM}}|) + pO(\langle |\vec{z}| \rangle), \quad (2.24)$$

where \vec{r}_{cam} is the position of the camera, \vec{r}_{CM} is the center-of-mass position of the particles and $\langle |\vec{z}| \rangle$ is the mean interparticle distance.

Altogether, this results in the following criterion:

$$kv\Delta t = k \frac{v}{c} \left(O(|\vec{r}_{\text{cam}} - \vec{r}_{\text{CM}}|) + pO(\langle |\vec{z}| \rangle) \right) \ll 2\pi. \quad (2.25)$$

This may be made a little more concrete by noting the criterion for convergence Eq. (2.12). Using that for $\lambda = 600\text{nm}$ and $a = 4\mu\text{m}$, $[S]_{\text{max}} \approx 10^3$ in the forward direction (as was used in the text just below Eq. (2.18)), taking the camera to be at a distance $f\langle|\vec{z}|\rangle$, and $\langle|\vec{z}|\rangle = mz_{\text{min}}$, we can write:

$$\frac{v}{c}m(f+p)10^3 < k\frac{v}{c}z_{\text{max}} \ll 2\pi, \quad (2.26)$$

and consequently a worst-case criterion (by numerical convergence) would be (for say, $m = p = f = 10$):

$$\frac{v}{c} \ll \pi \cdot 10^{-5}, \quad v \ll 10^3 \text{ m/s}, \quad (2.27)$$

which is extremely easily satisfied for any flow, let alone blood flow. A realistic case will not be too far off from the assumptions for $\{m, p, f\}$ made, and consequently the $v \ll c$ assumption in our algorithm is justified (for the tested parameters).

2.2. FLUIDS

For the fluids part of our multiphysics problem, **OpenFOAM** will be used (see App. B.1). The purpose of the fluids code is to compute the positions of the **RBCs** as they move along with the fluid. These positions will be written to a file (one file per ‘writeTime’), which will be converted to the input of the optics code by the linker. Our ultimate goal is to have the fluids code model blood flow in a complex patient-specific artery geometry.

2.2.1. BLOOD

Blood, which was described in Sec. 1.2, is usually modelled as a **non-Newtonian fluid**, rather than a mixture between blood plasma and its many dispersed particles. Then, any particles of interest (e.g. in drug delivery) are modelled as **Lagrangian particles**. For the present research the **RBCs** are of interest, which differ from the above particles in two important ways:

Firstly, they are asymmetrical and thus rotation plays a role, most certainly for the light scattering. Currently, the optics code does, however, scatter the light from particles as if they are spheres and thus rotation does not matter in the current stage, but will in the future. Hence in the present stage, taking this into account for the fluids code does not have a high priority.

Secondly, they are extremely densely packed with a typical hematocrit of 45%. This will certainly mean that **RBCs** aren’t simple tracer particles and that they are two-way coupled with the fluid, and possibly four-way coupled including particle-particle interactions as well. However, if blood is modelled as a non-Newtonian fluid, the effect the **RBCs** have on the fluid has already been taken into account by means of empirical models for the **rheology** of blood. Then, particle-particle interactions may, too, be forgotten about for the used cylindrical geometry (see Sec. 2.2.4), since all particles will be “keeping their lane” without collisions, while any other effects (e.g., drag applied to adjacent “lanes”) are in the rheology. This is only true, however, if we use an empirical result for the radial particle distribution, as was shown in Sec. 1.2. Applying Fig. 1.6 and Eq. (1.49) gives the particle number distribution (histogram) resp. the particle volume distribution shown in Figs. 2.5.

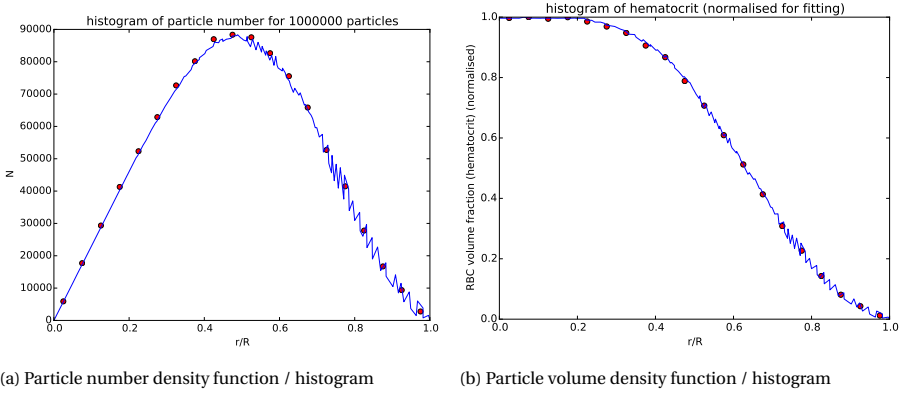


Figure 2.5: Particles are injected using the radial hematocrit profile given in Fig. 1.6. This was converted to a number density profile according to Eq. (1.49). The histogram of how 10^6 generated particles are distributed is shown in these two figures (dots), while the solid line is simply Aarts et. al.'s result (Fig. 1.6). This shows that they do indeed follow the required distribution, which confirms the method of Sec. 1.2.1.

The reader may wonder why the solid line is noisy. The reason is that Aarts et. al.'s plot has a range from $-R < r < R$, which we converted to the range $0 < r < 1$ by simply flipping the data points. The noise is the consequence of the fact that their radial distribution profile was not perfectly symmetric around $r = 0$. For our radial distribution profile we then take the average (which is per definition the smoothed version of the shown noisy line) of their left ($r < 0$) and right ($r > 0$) side. Evidently, the noisiness of the solid line does not affect the histogram, since the solid line is merely a probability distribution and because we deploy binning.

Although non-Newtonian effects will affect the (radial) velocity profile in the cylinder (and hence the time-dependency of the scattering profile), they do not affect the *instantaneous* scattering profile, since this solely depends on the radial particle distribution, which has been taken care of. It will, however, hypothetically affect how the scattering profile evolves over time. Hence at the present stage, non-Newtonian effects have not yet been taken into account, although they should in the near future. So, for now Eq. (1.54) will be used to describe the rheology of the fluid.

2.2.2. LAGRANGIAN PARTICLE TRACKING (LPT)

Now that RBCs are being modelled using LPT, it is important to determine what forces are relevant for the present problem of blood flow in the arteries. The possibly relevant forces have been described in Sec. 1.4. Using dimensional analysis, we can estimate the order of magnitude of each of those forces.

The forces scale with particle mass $m_p = \rho_p \frac{4}{3} \pi a^3$, fluid mass $m_f = \rho_f \frac{4}{3} \pi a^3$, characteristic velocity scales V (particle) and U (fluid), characteristic length scales H (in the pipe thickness direction) and L (in the stream direction) and characteristic timescales τ_p and τ_f .

- **Particle Inertia Force.** $\sim \frac{m_p V}{\tau_p}$
- **Gravity and Buoyancy Force.** $\sim (m_p - m_f) g$ (in direction of \vec{g})
- **Viscous Drag Force (Stokes).** $\sim 6\pi a \mu (V - U)$

- **Pressure Force.** $\sim m_f U \left(\frac{1}{\tau_f} - \frac{v}{H^2} \right)$
- **Added-mass Force.** $\sim m_f \frac{V-U}{\tau_p + \tau_f}$
- **Basset/History Force.** Vojir and Michaelides [12] show that the Basset term is relevant (rigid sphere, viscous fluid) when there are high-frequency velocity variations. And then, it is most pronounced for fluid to particle density ratios of 0.002 to 0.700. For the present case the density ratio is about 1, which shows virtually no influence of the Basset force. Certainly for the simple cylindrical geometry, there are no high-frequency velocity fluctuations: it has a steady state solution. Hence the Basset force will be neglected. This conclusion is in line with the findings of De Gruttola et. al. [13].

The typical timescale of the fluid is $\tau_f \sim \frac{L}{U}$. The typical timescale of the particles is $\tau_p = \frac{2\rho_p a^2}{9\nu\rho_f}$ [14, 15]. Defining the **Stokes number** as the ratio $St \equiv \frac{\tau_p}{\tau_f}$, we can rewrite τ_p in terms of τ_f . Anticipating on the typical numbers below, the Stokes number will be $St \sim 2 \cdot 10^{-7}$, which implies that $\tau_p \ll \tau_f$. This is sufficiently low to assume that the particles are merely tracer particles and thus that the velocity scales U and V will be of the same order of magnitude, $U \sim V$.

Upon applying the above, substituting the relation of the masses, and letting $\Delta U = (V - U)$, we then find:

- **Particle Inertia Force.** $\sim \frac{4}{3}\pi \frac{\rho_p a^3 U^2}{L} St^{-1}$
- **Gravity and Buoyancy Force.** $\sim \frac{4}{3}\pi a^3 (\rho_p - \rho_f) g$ (in direction of \vec{g})
- **Viscous Drag Force (Stokes).** $\sim 6\pi a \nu \rho_f \Delta U$
- **Pressure Force.** $\sim \frac{4}{3}\pi \rho_f a^3 U \left(\frac{U}{L} - \frac{v}{H^2} \right)$
- **Added-mass Force.** $\sim \frac{4}{3}\pi \rho_f a^3 \frac{U \Delta U}{L}$

Now, typical numbers for the given quantities are: $\rho_f = 1.16 \cdot 10^3 \text{ kg/m}^3$, $\rho_p = 1.1 \cdot 10^3 \text{ kg/m}^3$, $\nu = 8.28 \cdot 10^{-6} \text{ m}^2/\text{s}$, $a = 4 \text{ }\mu\text{m}$ and $H \sim R = 8 \text{ mm}$. The typical **Reynolds number** is $Re = 50$, from which we can take $U \sim u_{max} = 5.2 \text{ cm/s}$. A useful value for L would be the entrance/evolution length for laminar pipe flow, since that is the length over which streamwise variations happen and L was introduced only in relation to τ . A formula for the evolution length fitted using numerical results is given by Durst et. al. [16], which is valid for the given Reynolds number (unlike most engineering formulas out there). The result is that $L \sim 9.2 \text{ cm}$. Using these numbers, we can estimate the order of magnitude of all forces:

- **Particle Inertia Force.** $\sim \frac{4}{3}\pi \frac{\rho_p a^3 U^2}{L} St^{-1} \sim 4 \cdot 10^{-8} \text{ N}$
- **Gravity and Buoyancy Force.** $\sim \frac{4}{3}\pi a^3 (\rho_p - \rho_f) g$ (in direction of \vec{g}) $\sim 2 \cdot 10^{-13} \text{ N}$
- **Viscous Drag Force (Stokes).** $\sim 6\pi a \nu \rho_f \Delta U \sim 7 \cdot 10^{-7} \text{ kg/s} \cdot \Delta U$

- **Pressure Force.** $\sim \frac{4}{3}\pi\rho_f a^3 U \left(\frac{U}{L} - \frac{v}{H^2} \right) \sim 7 \cdot 10^{-15} \text{ N}$
- **Added-mass Force.** $\sim \frac{4}{3}\pi\rho_f a^3 \frac{U\Delta U}{L} \sim 2 \cdot 10^{-13} \text{ kg/s} \cdot \Delta U$

From these estimates, it immediately follows that the added-mass is negligible compared to Stokes drag. Pressure is negligible compared to buoyancy, and buoyancy is only important compared to Stokes drag if $\Delta U < 3 \cdot 10^{-7} \text{ m/s}$. This number is sufficiently low to state that, within the characteristic timescales of interest, Stokes drag is the only important force. This implies that it is to be expected that $V = U$ (with negligible error). The ‘particle inertia force’ is in fact not really a force: it is the left-hand side of Newton’s equation. Therefore, its order of magnitude is merely a measure for the particle response time, and it is always relevant.

Regarding gravity, having it turned on would not be desirable, as it would slowly destroy the neat radial particle distribution profile, which was obtained from experimental results⁷. At the present stage, the cases should remain simple to be able to draw conclusions more easily.

The particles will be modelled as one-way coupled. This is justified, because at the present stage we will only simulate $N = 100$ particles. For the parameters of Chap. 4, these have a resulting volume fraction of $O(10^{-6})$, which is sufficiently low to assume one-way coupling, according to Peirano et al. [17]. In actual blood, or even in dilute experiments, particles are much more densely packed. To simulate this effect, the best way is to adopt a non-Newtonian fluid model, rather than two-way coupling the particles. Two-way coupling the particles would only have an effect if one would actually simulate densely packed particles. There is however no reason for the fluids code to simulate so many particles, because the optics code currently cannot handle that many particles anyway.

2.2.3. NUMERICALLY SOLVING THE NAVIER-STOKES EQUATIONS

In OpenFOAM, the [Navier-Stokes equations](#) are discretised using the Finite-Volume Method. This method converts partial differential equations to a set of coupled equations. For a set of coupled linear equations, a single matrix inversion can solve the entire problem. Alternatively, the problem can be solved iteratively without inverting a single matrix. The Navier-Stokes equations do, however, result in a set of coupled non-linear equations, which are to be solved iteratively. OpenFOAM’s pimpleFoam solver is able to do so.

THE PIMPLE ALGORITHM

OpenFOAM’s pimpleFoam uses the iterative “PIMPLE” algorithm, which is a combination of the “Pressure Implicit with Splitting of Operator (PISO)” algorithm [18] and the “Semi-Implicit Method for Pressure Linked Equations (SIMPLE)” algorithm [19]. PIMPLE essentially takes PISO as an internal algorithm for an outer loop as seen in the SIMPLE algorithm. The resulting PIMPLE algorithm is as follows:⁸.

⁷Note that from Fig. 2.5 it followed that the experimental radial distribution profile was not symmetric. This might be due to gravity, since the author has not mentioned the direction of gravity in their experiments.

⁸The PIMPLE algorithm appears to be unique to OpenFOAM (correct me if I’m wrong). Its documentation consists merely of the source code for the solver: “\$FOAM_APP/solvers/incompressible/pimpleFoam”.

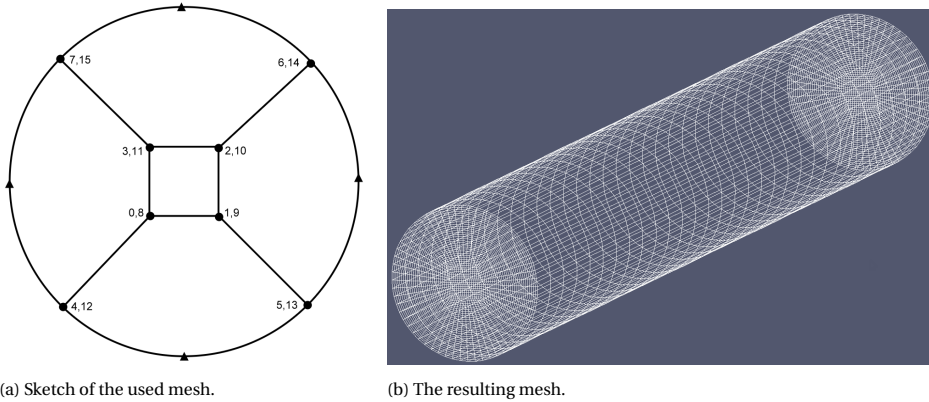


Figure 2.7: Geometry for the simple cylindrical case. (a) Sketch of the multiblock mesh, to be used by OpenFOAM. The numbers indicate vertex numbers in a tuple of the front ($z = 0$) and back ($z = L$) index. The triangles are anchors to be used to create a circular shape. (b) The resulting mesh, visualised in Paraview.

The inner loop (PISO) consists of solving the momentum and pressure equations in succession using a predictor-corrector approach for a fixed number of corrector steps. The outer loop (SIMPLE) iteratively repeats the inner loop until a certain convergence criterion is satisfied, or the maximum number of iterations has been reached. The velocity and pressure (for [incompressible flow](#)) are updated using [under-relaxation](#). Once the outer loop has converged, PIMPLE continues with the next timestep. I'd like to think of the loops as finding a [steady state](#) solution for the next timestep.

2.2.4. GEOMETRY / MESH

In [CFD](#), the flow is solved on a grid, conforming some geometry. While it is possible to simulate virtually any geometry with the fluids code, in the present research arteries are of interest, being either a simple cylinder or a full patient-specific complex arterial model. The cylindrical geometry allows for comparison with experiments more easily. As an example, the mesh for a cylindrical geometry is shown in Figs. 2.7.

2.3. COMBINED PHYSICS

Since our computational approach to [LSI](#) is one-way coupled, the fluids and optics codes will be two separate codes, rather than one monolithic code⁹. This provides a lot more convenience and flexibility: it permits virtually any existing [CFD](#) code to be used as the input to our optics code.

For this to work properly, the fluids code and optics code must be able to communicate, i.e., the output of the fluids code needs to be translated to the input of the optics code. To emphasise, the task of the fluids code is to compute the particle positions as a

⁹A monolithic code is per definition a single code which performs all tasks. This design principle discourages resuability and flexibility and should be avoided if there is no reason to design a code that way. Since the fluids code is independent of the optics code, there is no reason for the combined physics to be a single monolithic code, because it is possible for them to be two separate codes without any additional effort.

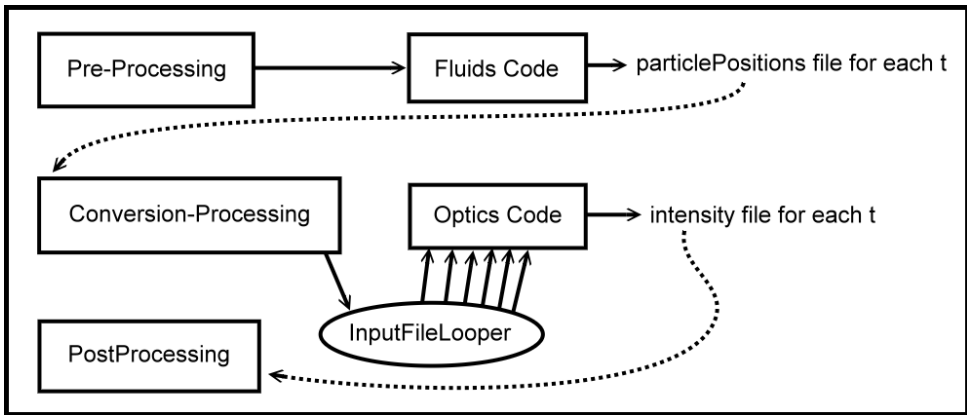


Figure 2.9: This figure shows the workflow of executing the combined code. The workflow consist of three independent branches, which are, in principle, not connected. The first is related to the fluids code, the second to the optics code, whilst the third is related to any post-processing activities.

function of time. The optics code takes these particle positions (amongst other input parameters) and computes the light scattering intensity at some predefined positions (i.e., at the camera's pixels). The whole linking process of the two codes will be subdivided into three separate workflows, as is shown in Fig. 2.9.

The first workflow is related to the fluids code. In the preprocessing step, the flow geometry with its accompanying mesh are generated, and the particle positions are generated (if the case under consideration uses manual injection, like in Fig. 2.5). Some more complicated cases might require more preprocessing steps, depending on the CFD package used. Immediately thereafter, the fluids code is executed, writing particle positions as a function of time to a series of files. First relatively big timesteps may be taken for the simulation to reach the desired initial fluid dynamics state. Then smaller timesteps may be taken to advance the particles on the timescale of interest for optics¹⁰; more details about the time-stepping process for a practical case will be given in Sec. 4.2.1.

The second workflow is independent of the first. First, the output of the fluids code is converted to an appropriate format. Then, an optics input file is generated, which specifies all parameters required for the optics code (e.g., the refractive indices). Finally, an external looper script loops over all particle position files and will repetitively call the optics code. The result is an intensity file for each timestep.

The third workflow is related to post-processing. Firstly, we convert the output of the optics code to a more pleasant format for post-processing. That is, the optics code can compute the intensity in arbitrary points in space, but it is convenient to define those arbitrary points as a 2D grid to represent a physical camera. The output of the optics code can then be converted to the format corresponding to this 2D grid to ease the post-processing process, such as creating speckle images in Chap. 4.

¹⁰The precise timescale of interest differs with the optical properties of the system, but typically you can think of $O(1 \mu\text{s})$, which is significantly shorter than $O(1 \text{ ms})$, as typically seen in CFD.

2.4. SUMMARY

This chapter described the developed optics code, the fluids code and how they are used in cohesion. These codes were developed to study the interferometric light scattering by flowing spherical particles.

The optics code uses Mie theory, which describes the scattering of a plane wave by a single spherical particle. It then assumes that the interparticle distance is sufficiently big that the scattered wave is a spherical wave by the time it reaches the next particle: a far-field assumption. Then it assumes that the particles are sufficiently small (or far away) for the spherical wave to be approximately a plane wave over the size of the particle. Now, since the scattered wave is again a plane wave incident on a single spherical particle, Mie theory may be applied to describe the scattered wave caused by the previous incoming wave. By continuing this process iteratively, all scattered waves may be collected at a camera, in which multiscattering has been taken into account.

For the fluid dynamics part of the problem, any existing computational fluid dynamics code may be used. OpenFOAM was used for the present research. Its task is to evolve the particles as a function of time within a flow. In the present research, the modelled fluid is a simplification of blood. It is modelled as a Newtonian fluid in which one-way coupled particles are suspended, which are spherical particles that represent red blood cells. The particles will be given a special radial number distribution, which represents the radial distribution of red blood cells in an artery.

The two codes are one-way coupled, because the optics code depends on the fluids code, but not the other way around. Hence, the fluids code will be used to output particle positions at all times of interest, and then the optics code will be executed for each time to compute the scattered intensity profile. Finally, separate post-processing codes will create figures and extract metrics from the intensity files that were output by the optics code.

Next, in Chap. 3 we will show a validation study for the optics code. Finally, in Chaps. 4-6 we will apply our code to practical situations with the goal of developing laser speckle imaging as a new quantitative non-invasive in-vivo measurement technique, specifically for biomedical applications. These three studies have the goal of extracting information from the simulated optical measurements, respectively: extract a heartbeat, extract the underlying flow's velocity, and study how atherosclerosis can be detected.

BIBLIOGRAPHY

1. Van As, K. *Interferometric Scattering of Light by an Ensemble of Flowing Spherical Particles: A Numerical Study* MA thesis (Delft University of Technology, 2015). <http://resolver.tudelft.nl/uuid:8dcdfd7c-d31d-4e70-a838-46441076bcb6>.
2. Bohren, C. F. & Huffman, D. R. *Absorption and Scattering of Light by Small Particles* Wiley Professional Paperback. ISBN: 0-471-05772-X (John Wiley & Sons, Inc., 1998).
3. Wiscombe, W. J. *Mie scattering calculations: advances in technique and fast, vector-speed computer codes* tech. rep. (National Center for Atmospheric Research, 1979).
4. Wiscombe, W. J. Improved Mie scattering algorithms. *Appl. Opt.* **19**, 1505–1509 (1980).
5. Barber, P. W. & Hill, S. C. *Light Scatter by Particles: Computational Methods* Wiley Professional Paperback. (Original work published 1990). ISBN: 9971-50-832-X (World Scientific Publishing Co. Pte. Ltd., 1998).
6. Lippmann, B. A. & Schwinger, J. Variational principles for scattering processes. I. *Physical Review* **79**, 469 (1950).
7. Born, M. Quantenmechanik der stoßvorgänge. *Zeitschrift für physik* **38**, 803–827 (1926).
8. Osnabrugge, G., Leedumrongwatthanakun, S. & Vellekoop, I. M. A convergent Born series for solving the inhomogeneous Helmholtz equation in arbitrarily large media. *Journal of computational physics* **322**, 113–124 (2016).
9. Lee, M., Hugonnet, H. & Park, Y. Inverse problem solver for multiple light scattering using modified Born series. *Optica* **9**, 177–182 (2022).
10. Nilsson, A. M. K., Alsholm, P., Karlsson, A. & Andersson-Engels, S. T-matrix computations of light scattering by red blood cells. *Appl. Opt.* **37**, 2735–2747 (1998).
11. Steinke, J. M. & Shepherd, A. P. Comparison of Mie theory and the light scattering of red blood cells. *Appl. Opt.* **27**, 4027–4033 (1988).
12. Vojir, D. J. & Michaelides, E. E. Effect of the History Term on the Motion of Rigid Spheres in a Viscous Fluid. *Int. J. Multiphase Flow* **20**, 547–556 (1994).
13. De Gruttola, S., Boomsma, K. & Poulikakos, D. Computational Simulation of a Non-Newtonian Model of the Blood Separation Process. *Artificial Organs* **29**, 949–959 (2005).
14. Brennen, C. E. *Fundamentals of multiphase flow* Reprint. ISBN: 9780521848046 (Cambridge Univ. Press, 2005).
15. Stuart, D. C. C. *The Development of a Discrete Particle Model for 3D Unstructured Grids: Application to Magnetic Drug Targeting* MSc Thesis (Delft, University of Technology, Apr. 2009).

16. Durst, F., Ray, S., Ünsal, B. & Bayoumi, O. A. The Development Lengths of Laminar Pipe and Channel Flows. *Journal of Fluids Engineering* **127**, 1154–1160 (2005).
17. Peirano, E. & Leckner, B. Fundamentals of gas-solid flows applied to circulating fluidized bed combustion. *Progress in Energy and Combustion Science* **24**, 259–296 (1996).
18. Issa, R. I. Solution of the Implicitly Discretised Fluid Flow Equations by Operator-Splitting. *Journal of Computational Physics* **62**, 40–65 (1985).
19. Ferziger, J. H. & Peric, M. *Computational Methods for Fluid Dynamics* 3rd. ISBN: 978-3-642-56026-2 (Springer-Verlag, 2002).

3

OPTICS CODE VALIDATION: THE FRAUNHOFER SOLUTION

The optics code was described in Chap. 2. Several simplifications had to be made, and their importance was discussed theoretically in Sec. 2.1.7. It is pivotal for a programmer to convince not only himself, but also the world that his code does what it says it does. Or, in our case, that our code makes accurate predictions of our physical reality.

To that end, in this chapter we mimic the classical [double-slit experiment](#) by aligning many spherical particles in two straight lines. We execute our optics code on these particles, and compute the resulting [intensity](#) profile. Although these particles do not truly form two slits, we do expect to obtain the same [interferometric](#) pattern, as an observer being very far away cannot see the individual particles. We then compare our results with the solution described by the far-field [Fraunhofer approximation](#) at various length scales.

It is found that our code produces the expected interferometric features at all length scales in which there are features to be expected: the length of an individual slit, the double slit experiment, at the [interparticle distance](#), and finally an [Airy pattern](#) at the length scale of the individual [scatterers](#). These scenarios provide evidence that our optics code does indeed have the correct interferometric behaviour.

This chapter is a rewritten version of a chapter previously published in: Van As, K. (2015). *Interferometric Scattering of Light by an Ensemble of Flowing Spherical Particles: A Numerical Study* [Master's Thesis, Delft University of Technology]. [1] Available online via <http://repository.tudelft.nl>.

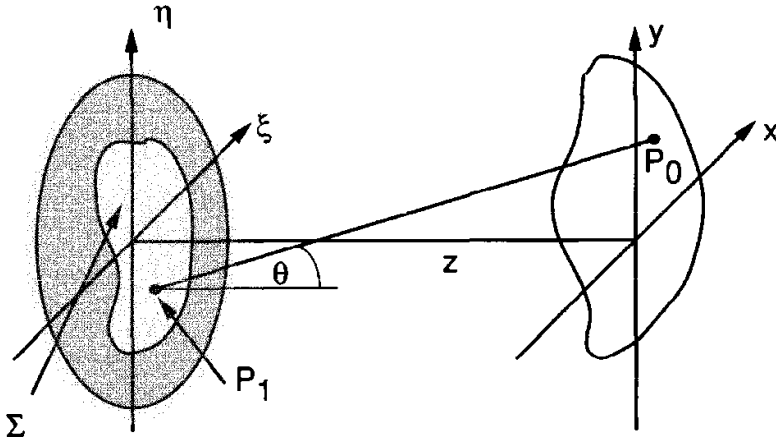


Figure 3.1: The **diffraction** geometry, reprinted from Goodman Fig. 4.1 (p65) [2]. θ_s is the **scattering angle**. P_0 is a point in the scattering plane, originating from point P_1 on the aperture, Σ . (ξ, η) are the **orthonormal** coordinates in the aperture plane, and (x, y) in the scattering plane respectively.

3.1. THEORY: THE FRAUNHOFER APPROXIMATION

One way to validate a code (to some extent) is to compare its output with known exact theoretical solutions. In the case of light scattering, we may use the **Fraunhofer diffraction** equation (which is a **Far-Field (FF)** approximation) on some well-known cases: a rectangular **aperture** and a double slit. In this section, the formalism of Goodman [2] is followed to arrive at the Fraunhofer equation, cf. Fig. 3.1.

The **Huygens-Fresnel principle** may be used to describe the response of an aperture to an **Incoming Plane Wave (IPW)**. It states that the scattered amplitude, $U(P_0)$, at some distant point P_0 behind the aperture, is given by:

$$U(P_0) = \frac{1}{i\lambda} \iint_{\Sigma} U(P_1) \frac{\exp(ikr_{01})}{r_{01}} \cos(\theta) d\sigma, \quad (3.1)$$

where r_{01} is the magnitude of \vec{r}_{01} , which is a vector pointing from P_1 to P_0 , θ is the angle between the aperture's outward normal \hat{n} and \vec{r}_{01} . λ is the wavelength and $k = \frac{2\pi}{\lambda}$ is the wave number. Σ is the aperture and $d\sigma$ is an infinitesimal surface element of the aperture. The Huygens-Fresnel Principle is arrived upon after having made two assumptions: (1) scalar wave theory must hold and (2) $r_{01} \gg \lambda$.

Fresnel approximated the Huygens-Fresnel Principle by making a near-axis assumption, i.e., $\theta \ll 1$. In this case, the zeroth order approximation is $r_{01} = z / \cos(\theta) \approx z$. For the phase factor, a second order approximation is made instead: $r_{01} \approx z \left(1 + \frac{(x-\xi)^2 + (y-\eta)^2}{2z} \right)$, where $\vec{P}_1 = \xi \hat{x} + \eta \hat{y}$ is the local coordinate in the aperture, while $\vec{P}_0 = x \hat{x} + y \hat{y}$ is the coordinate in the scattering plane. The resulting **Fresnel diffraction** integral is said to be valid in the aperture's near-field¹.

¹I consider the term 'near-field' for this purpose as very paradoxical, given the approximations made: near-axis and *far-field*, i.e., the term 'near-field' seems to contradict the actual far-field assumption.

The Fraunhofer approximation further approximates the Fresnel integral by only retaining the terms up to first order in the phase, i.e.,

$$z \gg \frac{k}{2} \max(\xi^2 + \eta^2), \quad (3.2)$$

which makes the Fraunhofer approximation valid in the **FF**. The resulting Fraunhofer diffraction integral then becomes:

$$U(x, y) = \frac{e^{ikz} e^{i\frac{k}{2z}(x^2+y^2)}}{i\lambda z} \iint_{\Sigma} U(\xi, \eta) \exp\left[-i\frac{2\pi}{\lambda z}(x\xi + y\eta)\right] d\xi d\eta. \quad (3.3)$$

3.1.1. SOLUTION 1: RECTANGULAR APERTURE

For a single rectangular aperture, the Fraunhofer diffraction integral in Eq. (3.3) predicts an intensity profile of the form

$$I(x, y) = \frac{A^2}{\lambda^2 z^2} \operatorname{sinc}^2\left(\frac{2w_X x}{\lambda z}\right) \operatorname{sinc}^2\left(\frac{2w_Y y}{\lambda z}\right), \quad (3.4)$$

where w_{X_i} is the *half*-width of the aperture in the \hat{x}_i direction, which denotes either \hat{x} or \hat{y} , and $A = 4w_X w_Y$ is the area of the aperture. This is a periodic, decaying function for any given z . The distance between two successive minima in one direction is given by:

$$\Delta x_i = \frac{\lambda z}{w_{X_i}}. \quad (3.5)$$

3.1.2. SOLUTION 2: DOUBLE SLIT

The solution for the double slit experiment is similar to that of a single rectangular slit, but involves a cosine instead of a sinc function. Eq. (3.5) applies as well, provided that we interpret w_{X_i} as the distance between the two slits in the \hat{x}_i direction.

3.1.3. SOLUTION 3: CIRCULAR APERTURE

A circular aperture will result in an Airy pattern of the form

$$I(r) = \left(\frac{A}{\lambda z}\right)^2 \left[2\frac{J_1(kwr/z)}{kwr/z}\right]^2, \quad (3.6)$$

where $r = \sqrt{x^2 + y^2}$ is the radius in the observation plane, w is the radius of the aperture and J_1 is the first **Bessel function** of the first kind.

The radial distance of the extrema of Eq. (3.6) may be found using

$$\Delta r_j = b_j \lambda z / 2w, \quad (3.7)$$

where b_j denotes the argument where $J_1^2(\pi b_j)$ has its j 'th extremum. Tab. 4.1 of Goodman (p.78) [2] gives b_j for the first few oscillations, e.g., $b_0 = 0$ (maximum), $b_1 = 1.220$ (minimum), and $b_2 = 1.635$ (maximum). For comparison, we will primarily be using b_2 to find the distance between the first two maxima, which have a relative intensity of 0.0175 according to Eq. (3.6).

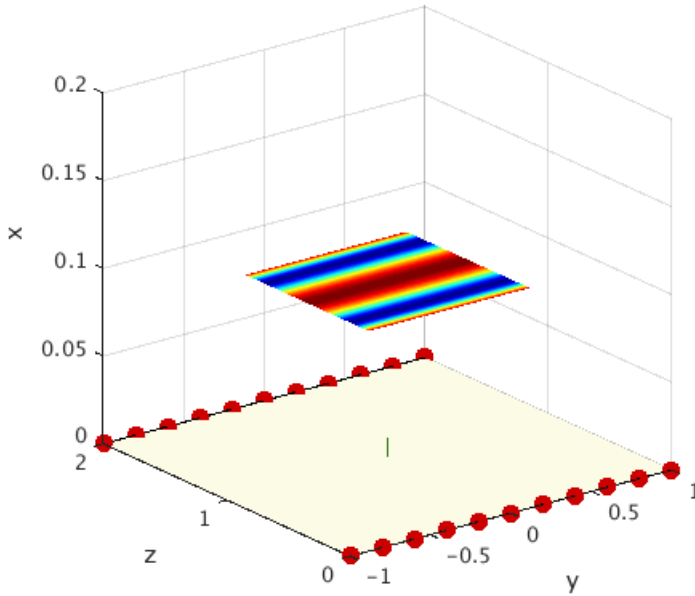


Figure 3.2: The used scattering geometry. An incoming **PW** is coming in from below with $\vec{k} = k\hat{x}$. The wave scatters off of each individual scatterer (red spheres), forming an interferometric pattern on the camera. Note that the figure is *not* to scale: a much larger L , much smaller particles, and many more particles were used in the actual simulations.

3.2. METHODS

3.2.1. GEOMETRY

Our code is not designed to work with apertures. Rather, it computes the field scattered by an ensemble of spherical scatterers. We may, however, arrange many spheres in a line and state that for an observer sufficiently far away this looks identical to a single slit (or, arranging particles in two lines will look like a double slit). We choose our scattering geometry as is shown in Fig. 3.2, using a square camera with its normal orthogonal to the **PW** incoming from the \hat{x} direction. We use 301 equidistant spherical particles for each slit. Since our setup comprises that many spherical particles, it is reasonable to assume that an Airy pattern² will be superimposed on the expected exact Fraunhofer solution.

3.2.2. NON-DIMENSIONALIZATION

In order to validate our code, we intend to compare the distance between interferometric **fringes** (i.e., the distance between local maxima and minima) with those predicted by the Fraunhofer solution. To that end, we first non-dimensionalize some quan-

²Our spherical particles have a circular frontal area. An Airy pattern is the expected interferometric pattern of scattering from a circular aperture.

Table 3.1: Parameters used in our Fraunhofer validation study. d is the characteristic size of the aperture. \hat{x}_i denotes the direction in which we theoretically expect to see the fringes. $|\vec{r}|$ is the camera's half-width (identical in both directions), as computed from Eqs. (3.8-3.9). Constant parameters: $\lambda = r_{\text{sph}} = 0.02$ and $L = 10^3$. All units are arbitrary units.

Case	d	\hat{x}_i	$ \vec{r} $	\tilde{L}
(a) Length of each individual slit	60	\hat{y}	1.667	$5.6 \cdot 10^{-3}$
(b) Distance between the two slits	2	\hat{z}	50	5
(c) Distance between two scatterers within a slit, \mathcal{Z}	0.2	\hat{y}	500	500
(d) Diameter of an individual scatterer	0.04	Airy	1362.5	$1.3 \cdot 10^4$

ties. We define $|\vec{r}_i|$ to be the half-width of the camera³. Next we non-dimensionalize $\Delta\tilde{x}_i = \Delta x_i / 2|\vec{r}_i|$, such that Eq. (3.5) becomes:

$$2|\vec{r}_i| = \frac{\lambda L}{d\Delta\tilde{x}_i}, \quad (3.8)$$

where $d = w_{X_i}$ is the 'characteristic size' of the aperture being studied, and L is the distance between the aperture plane and the camera. This equation permits us to redefine the non-dimensionalized camera size as 1x1, and choose $\Delta\tilde{x}_i = 0.1$, such that we expect to see exactly 10 fringes 0.1 apart in the \hat{x}_i direction on our camera if our code is valid, allowing for more easy comparison between different input parameters.

For the Airy pattern, a similar equation to Eq. (3.8) may be derived from Eq. (3.7):

$$2|\vec{r}| = \frac{b_j \lambda L}{d\Delta\tilde{r}}, \quad (3.9)$$

using the parameters of Sec. 3.1.3, and using $d = 2w$ as the 'characteristic size', which equals $2r_{\text{sph}}$ in our situation, where r_{sph} is the radius of each individual spherical particle. If we now demand that $\Delta\tilde{r}_2 = \Delta r_2 / 2|\vec{r}| = 0.3$, the hypothesis is that on the camera's virtual image the second maximum lies at a radius $\tilde{r}_2 = 0.3$, in analogy with $\Delta\tilde{x}_i = 0.1$ above.

3.2.3. PARAMETERS

To validate our code, we identify four distinct cases, as our geometry has four important length scales: length of a single slit, distance between slits, distance between scatterers, and the size of each individual scatterer. These are shown in Tab. 3.1. Constant parameters are listed in the table's caption, which are chosen quite arbitrarily for the purpose of this case study.

Important is that L is chosen such that the FF requirement of the Fraunhofer approximation, cf. Eq. (3.2) is satisfied:

$$\tilde{L} = \frac{L}{d^2/\lambda} \gg 1, \quad (3.10)$$

where \tilde{L} is the non-dimensionalized camera distance. Fig. 3.3 shows the evolution of an interference pattern as L is increased, while proportionally increasing the size of the

³Although we use a square camera, we write $|\vec{r}_i|$ rather than $|\vec{r}|$, since in the more general case the camera could be rectangular.

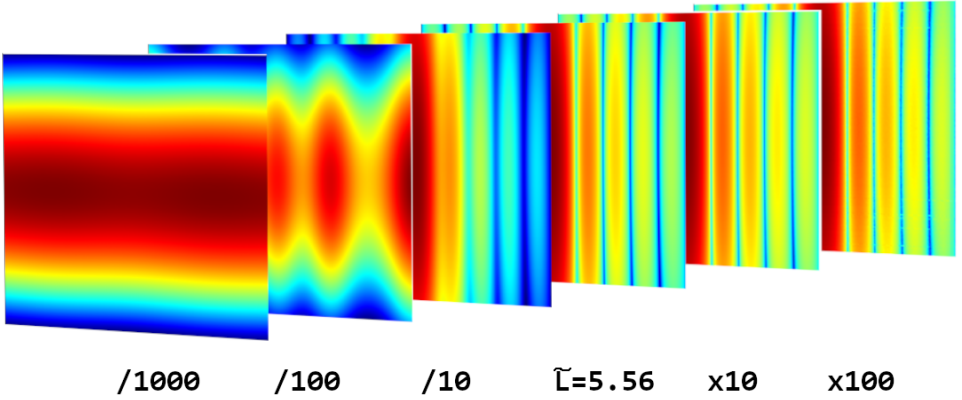


Figure 3.3: As the camera is placed further away (increasing L), the interference pattern develops towards the far-field solution. The colors show $\log(\text{intensity})$, and are not to scale between the images (i.e., that is impossible, because intensity decreases as L increases). Parameters used for these simulations: $\lambda = r_{\text{sph}} = 2$, $d = 60$, $L = 10^4$ with $|\vec{r}| = 1.667 \cdot 10^3$ (cf. Eq. (3.8)) for the $\tilde{L} = 5.56$ case, and the geometry as described in Sec. 3.2.1.

camera. Note that if L is sufficiently large, the interference pattern remains identical: the Fraunhofer solution.

However, a word of caution: if L is increased too far, the computer simulations run into numerical resolution problems, the first noisy effects of which can be seen in the rightmost image of Fig. 3.3. As the results in the next section will show, this was troublesome for case (a) of Tab. 3.1; therefore, to validate our code for the (a) case, we performed two additional simulations with a different λ that did not run into this numerical resolution problem, which are shown in Tab. 3.2.

3.3. RESULTS

The simulation results for our SSFF code are shown in Figs. 3.4. First note that the difference between (a)-(d) is merely the size of the camera used for the simulation. This means that the pattern shown in (a) is the very center of (b), (b) of (c), and (c) of (d), e.g., the area of (b) is the middle 1% of the area of (c).

In (b) we are observing at the length scale of the double slit experiment, which was the primary goal of this validation study. We find the expected squared cosine pattern with 0.1 distance between the fringes in the \hat{z} direction.

Table 3.2: Two alternative versions of Tab. 3.1(a), using different values of $\lambda = r_{\text{sph}}$.

ID	$\lambda = r_{\text{sph}}$	d	\hat{x}_i	$ \vec{r} $	L	\tilde{L}
(a ₁)	0.02	60	\hat{y}	$1.667 \cdot 10^0$	10^3	$5.56 \cdot 10^{-3}$
(a ₂)	0.2	60	\hat{y}	$1.667 \cdot 10^3$	10^5	5.56
(a ₃)	2	60	\hat{y}	$1.667 \cdot 10^4$	10^5	55.6

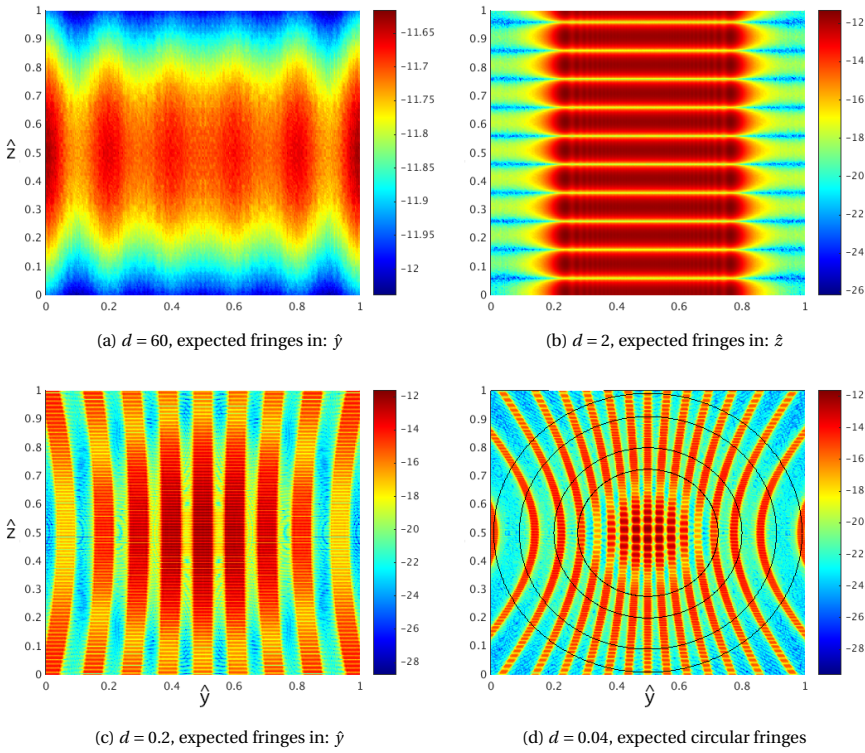


Figure 3.4: Simulated log(intensity) profile, cf. Tab. 3.1 ($\lambda = 0.02$), by the SSFF code. In (a) the FF assumption could not be satisfied. In (d) circles are drawn to illustrate the hypothesised extrema of the Airy pattern, which are from the middle outwards: max at $r = 0$, min, max at $r = 0.3$, min, max.

Similarly, (c) observes at the length scale of the distance between two individual particles within one slit. Although this is not the exact same as a double slit experiment, we still find a cosine-like pattern with the expected 0.1 distance between fringes in the \hat{y} direction. As we move further from the center, the distance between the fringes starts to increase, which seems to contradict the prediction. However, given that a FF observer does not actually see a rectangular aperture with the size equal to the interparticle distance, we should not expect to find an exact match for case (c): the order of magnitude is spot on.

Case (d) is observing at the length scale of the individual spherical particles. For these tiny circular apertures, we expect to see a large-scale Airy pattern. We find the first maximum to line up with the expected 0.3 radius quite well; however, the minima and more distant maxima do not line up precisely. The relative intensity of the first two maxima (at $r = 0$ and $r = 0.3$) is 0.0184, while from Sec. 3.1.3 we'd expect a value of 0.0175, which is accurate to a $\sim 5\%$ error. Given that a FF observer does not actually see one tiny circular aperture, we should not expect an exact match in either this value nor the precise location of all extrema: the order of magnitude is what we expect it to be.

Finally, in (a) we are observing at the length scale of a single long slit. Unfortunately,

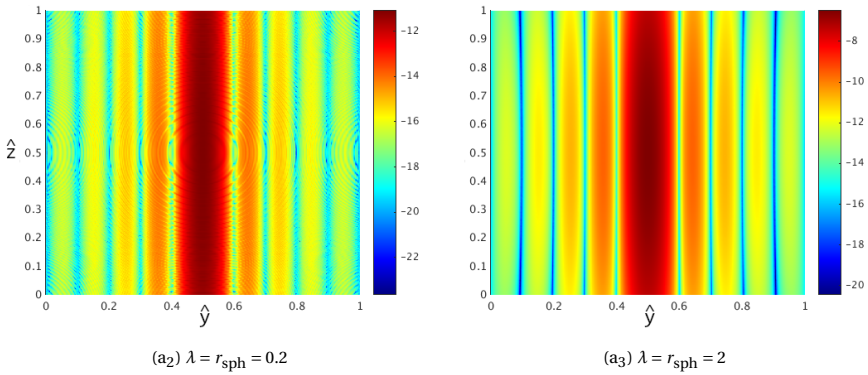


Figure 3.5: Like Fig. 3.4a, but using different values for λ and r_{sph} , cf. Tab. 3.2, to be able to more easily satisfy the FF requirement.

we were unable to produce the FF solution with $\tilde{L} \gg 1$, as these simulations ran into the aforementioned numerical resolution problem (see Sec. 3.2.3), before reaching the FF requirement. Therefore, (a) shows a near-field solution (compare with Fig. 3.3) with the same \tilde{L} as (b)-(d) instead, to show that it is the $\sim 0.1\%$ middle area of (b).

Instead, Figs. 3.5 show cases (a₂) and (a₃) to replace case (a₁) to study the length scale of a single long slit⁴. Here we find the expected 0.1 distance between fringes, with the sinc function's characteristic wide central band with a width of $2 \cdot 0.1$.

Interestingly, case (a₂) appears to show multiple superimposed Airy-like patterns that we had not expected. We'd expect the Airy pattern caused by the spherical particles to be a factor ~ 500 times larger than these circles. Since we are looking at a very small interference pattern, these Airy-like patterns should be caused by a very large spatial length scale. We do not know what caused them, but they do seem physical.

Finally, our MSFF code yielded the same conclusions as our SSFF code [1], with similar figures, which we omit here to keep it concise.

3.4. CONCLUSIONS

In this chapter it was shown that our optics code is able to produce the expected interferometric features at various length scales, cf. what we may expect from the exact (FF) Fraunhofer solution. The scattered profile from a single slit and a double slit were both produced correctly, and the expected Airy pattern was found at the length scale of the individual scatterers. Although this cannot prove the optics code to correctly compute the light scattering by an ensemble of spheres, this does provide evidence that the (interparticle) phase behavior of our optics code is correct.

A word of caution should be placed when studying cases in the extreme FF, as the optics code could run into numerical resolution problems due to rounding errors.

For future research, it would be interesting to study different cases for λ and r_{sph} , e.g., to find the origin of the very large Airy-like circles in Figs. 3.5.

⁴Cases (a₂) and (a₃) also run into numerical resolution problems as we kept increasing \tilde{L} even further, but for these cases we were still able to resolve the FF solution before reaching those problems.

BIBLIOGRAPHY

1. Van As, K. *Interferometric Scattering of Light by an Ensemble of Flowing Spherical Particles: A Numerical Study* MA thesis (Delft University of Technology, 2015). <http://resolver.tudelft.nl/uuid:8dcd7c-d31d-4e70-a838-46441076bcb6>.
2. Goodman, J. W. *Introduction to Fourier Optics* 2nd. ISBN: 0-07-024254-2 (The McGraw-Hill Companies, Inc., 1996).

4

DETECTING A HEARTBEAT USING LASER SPECKLE IMAGING

*Laser Speckle Imaging (LSI) can be used to study dynamic processes in **turbid media**, such as blood flow. However, it is presently still challenging to obtain meaningful quantitative information from **speckles**, mainly because speckle is the interferometric summation of **multiply scattered** light. Consequently, speckle represents a convolution of the local dynamics of the medium.*

*In this paper, we present a new computational model for simulating the **LSI** process, which we aim to use for improving our understanding of the underlying physics. Thereby reliable methods for extracting meaningful information from speckle may be developed.*

*To validate our code, we apply it to a case study resembling blood flow: a cylindrical fluid flow geometry seeded with small spherical particles, and modulated with a heartbeat signal. From the simulated speckle pattern, we successfully retrieve the main **frequency modes** of the original heartbeat signal. By comparing Poiseuille flow to plug flow, we show that **speckle boiling** causes a small amount of uniform spectral noise. Our results indicate that our computational model is capable of simulating **LSI**, and will therefore be useful in future studies for further developing **LSI** as a quantitative imaging tool.*

This chapter was published previously: Van As, K., Boterman, J., Kleijn, C. R., Kenjeres, S. & Bhattacharya, N. (2019). *Laser speckle imaging of flowing blood: A numerical study*. [Physical Review E](#), 100. This paper was selected as “*Editor’s Choice*”. In this chapter, minor clarifications were made compared to the published work.

4.1. INTRODUCTION

Using diffuse optics for studying dynamics in disordered media is slowly becoming the main enabler of **non-invasive** optical diagnostic devices [1], finding many applications in the study of biological tissue. These developments are also driven by the increasing demand for readily accessible health care to the rising world population. The main phenomena occurring when light propagates in tissue are absorption and scattering. Absorption of light is used for identifying the different molecular species present in a sample, and for determining their concentration. Light **scattering**, on the other hand, provides information about **scatterer** size and motion in the sample. In most cases, light is used to illuminate tissue, after which the scattered light is collected in either reflection or transmission.

4 Illuminating **diffusive media** with **coherent light** leads to a random **interference** pattern called **speckle**. The speckle is formed by the constructive and destructive interference resulting from path length variations of the light coming to the detector due to surface irregularities or different depths traversed in the media. To interpret such speckle images, physical models of light-tissue interaction are needed. Many different models have been used to study light propagation in tissue with the aim of gaining better insight into the underlying physics and quantifying the detected signals. These techniques range from approximating the light transport as a diffusive process [2–6], simulating a photon random walk using the **Monte Carlo method** [7–9], to modelling scattering from blood using the Mie-Percus-Yevick equations [10].

Any motion of, or inside, the sample causes the speckle pattern to change. The entire pattern could move (**‘translating speckle’**), maintaining speckle correlation, or the speckles could randomly appear or disappear (**‘speckle boiling’**) due to relative motion of the scatterers [11]. Since the speckle pattern contains information about the dynamics of the scatterers, speckle imaging is thus used in many applications, ranging from non-destructive testing, stellar interferometry [12], study of coatings [13, 14], to biomedical applications [15]. Therefore, using speckle decorrelation is very attractive for the study of flow behind **turbid media**, as is the case for many biological applications.

For the specific case of blood flow embedded in tissue, the reflection, absorption, and transmission properties of the different layers that the light travels through each have an impact on the detected light. The standardisation of parameters required for medical applications is very challenging, considering that properties of skin and tissue could vary from patient to patient, e.g., depending upon health, age and ethnicity of the subject. Although there is large variation in optical properties of the static scatterers contributing to the detected signal, the temporal dynamics of the flow or the moving scatterers is also imprinted in the temporal evolution of the speckle patterns. Thus underlying flow can be studied by observing the temporal statistics of speckle fluctuations [16, 17]. Using speckle patterns to study any phenomenon has the advantage that no **direct imaging** is necessary, which largely simplifies the required equipment. **In-vivo** blood flow monitoring has been studied quite extensively using speckle-based techniques. These techniques, such as **Laser Speckle Contrast Imaging (LSCI)** and complementary techniques like multi-exposure **LSCI**, along with relevant applications, have been described in detail in a recent review [18].

However, there presently is no agreement in the literature as to how to quantitatively

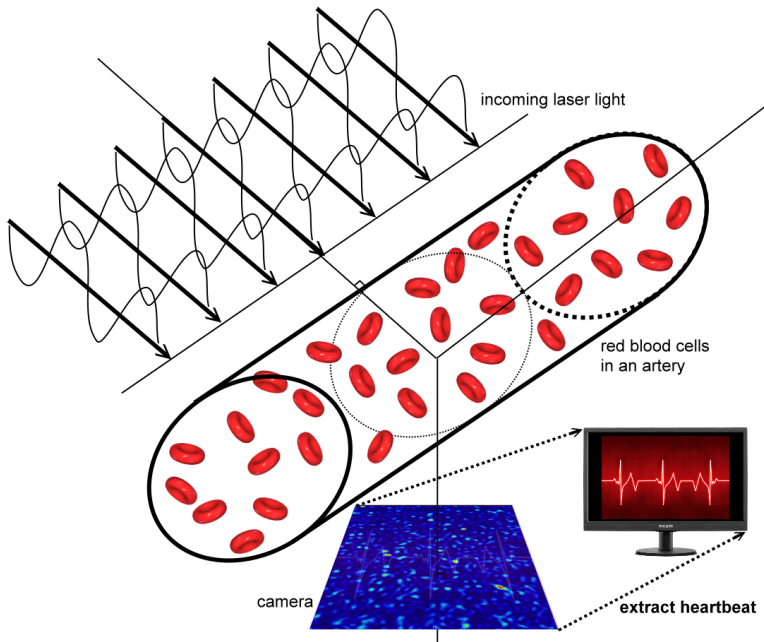


Figure 4.1: Sketch of Laser Speckle Imaging applied to an artery: a PW of coherent light enters the medium, multiply scatters on the particles, and is finally gathered at a camera set at a 90° angle with respect to the incoming light. The result is a noise-like interferometric pattern, known as a speckle pattern, from which we wish to obtain quantitative information.

deduce the material's dynamics from the speckle dynamics [19]. One metric for quantifying the speckle dynamics is the speckle contrast, which is the ratio of the intensity's standard deviation and its mean. Since the speckles are dynamic, they will blur when observed with a regular camera due to its finite exposure time, t_{int} . The speckle contrast of the blurred speckles depends on t_{int} and on the speckle decorrelation time, τ_c . It is widely accepted that τ_c is inversely proportional to the local velocity of the scatterers, but the proportionality constant is disagreed upon [19]. It was even shown theoretically that the velocity distribution affects how the speckle contrast depends on τ_c [20]. Therefore, in order to further develop LSI as a quantitative measurement technique, a thorough understanding of the scattering process must be acquired.

This may be achieved by using computer simulations, which have the major advantage that noise factors – which are always present in experiments – may be turned off one-by-one to quantify their effect. Therefore, we have developed an interferometric computational model which can simulate the LSI process: an incoming coherent Plane Wave (PW) is multiply scattered by an ensemble of randomly distributed particles – which represent RBCs in the present study – and is finally collected at a camera (see Fig. 4.1). The optics code is based on coherent Mie scattering with multiple scattering implemented iteratively, but simplified in order to make studying the temporal dynam-

ics computationally feasible. The particles are evolved using an existing **Computational Fluid Dynamics (CFD)** code, which we have coupled to our optics code. The result is a novel modular code, capable of simulating every aspect of the **LSI** process. Finally, note that the standard approach for simulating light scattering in turbid media is to use Monte Carlo techniques [7–9], in which light scattering is simulated as random-walks of photons. Our new approach explicitly tracks the position of each particle, allowing for accurately computing interference effects, and should thus lead to more realistic results.

As a first step towards quantitative **LSI**, and to validate our simulations, we mimic an experimental setup [21] which used a cylindrical **phantom** with a size characteristic to that of the **external carotid artery (ECA)** (radius ~ 1 mm). Spherical particles the size of **RBCs** (radius ~ 4 μm) were used as scatterers. The flow was given a mean velocity typical to blood in the **ECA** (~ 1 m/s), modulated with a realistic heartbeat. We study the effect of a realistic flow profile by comparing it with **plug flow**. Using our code, we have simulated the resulting dynamic speckle images of the moving particles. Finally, we have retrieved the frequency spectrum of the modulated heartbeat from the speckles, which also compares well with that from the experimental setup. These results show the capability of our code to simulate the **LSI** process. In future work, we aim to include the effect of more parameters to develop a quantitative understanding of their influence on speckle dynamics (e.g., the effect of a surrounding static scattering medium: skin and tissue).

4.2. APPROACH

In this section, we first outline the principle of **LSI**. Then we discuss the underlying theory of our optics code: Mie theory. We proceed by discussing the geometry and the fluid dynamics of our simple case study. Finally, we discuss some relevant notes for obtaining accurate simulation results.

4.2.1. SPECKLE IMAGING

When **phase-coherent** light scatters on a surface that is rough at optically-relevant scales, a speckle pattern is formed. This is the result of a random interferometric summation caused by the different path lengths the light has travelled as it originates from different spots of the scattering surface. One metric that can be used to extract information from speckle is the **speckle contrast** [22, 23]:

$$K \equiv \frac{\sigma_I}{\langle I \rangle}, \quad (4.1)$$

where $\langle I \rangle$ is the mean **intensity** and σ_I is its standard deviation. We speak of **fully-developed speckle** when the phases become uniformly distributed over $[0, 2\pi]$ radians after **diffusing**/scattering (i.e., no **specular** component remains) [24]. Then, the intensity becomes Gaussian-distributed [25]: $\sigma_I = \langle I \rangle$, and thus $K = 1$. However, when the light **depolarises** due to multiple scattering, a value below one may be expected [26].

When both the illumination and the **scatterers** remain the same, the speckles will also remain unchanged. When the scatterers move without relative motion, the speckles will simply translate at the same rate. However, if there is relative motion between the scatterers, the path length differences will change, which causes speckles to randomly

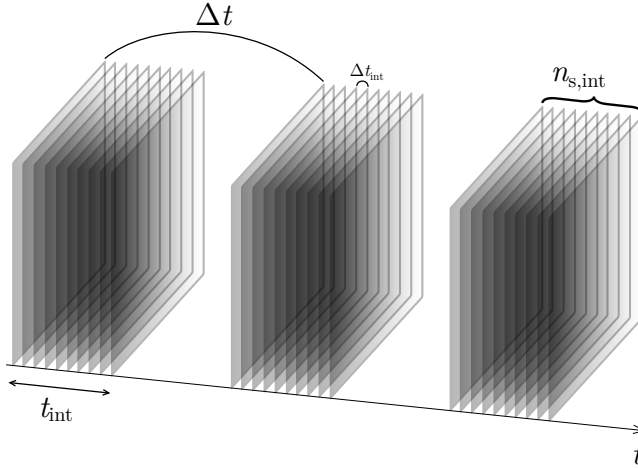


Figure 4.2: We sample instantaneous data rapidly (interval Δt_{int}) to mimic a real camera's integration time t_{int} , and repeat this at distant intervals (Δt apart) to gather temporal data.

appear and disappear. This is called ‘speckle boiling’ [11, 27], which is a source of noise in LSI.

Provided that the effect of speckle boiling is sufficiently small, we can use translating speckle to study the collective dynamics of the scatterers [22, 28], although non-translational speckle could also be used [11]. When translating speckle is imaged with a camera, a blurred speckle image will be measured due to the finite camera integration time. Since blurring decreases σ_I , but does not affect $\langle I \rangle$, the result is a lower K . Therefore, through the camera integration time, the speckle contrast depends on the amount of blurring and thus also on velocity [19]. Our research group has applied this principle previously to experimentally study pulsatile flow in a patient-specific carotid artery [21, 29].

In the present work, we introduce a code capable of simulating the whole LSI process. The optics code uses Mie theory to propagate a coherent PW to all scatterers, computes how the light diffracts of each of them, and then propagates all scattered waves to a simulated camera. The resulting image is an interferometric scattering pattern: a speckle pattern. In addition to scattering directly to the camera (i.e., single scattering), multiple scattering is implemented iteratively (see Sec. 4.3.2). A separate fluid dynamics code is used for computing the motion of the scatterers, after which the optics code is used to calculate the instantaneous scattering. We mimic the aforementioned blurring effect of a real camera by time-averaging many independent instantaneous simulations in rapid succession with timestep Δt_{int} , as can be seen in Fig. 4.2. This is accurate provided that $n_{\text{s,int}}$ is sufficiently large. We then repeat this process Δt later to obtain temporal data: $K(t)$.

4.2.2. MIE THEORY

For simulating the electromagnetic scattering of light by the scatterers, our code makes use of Mie theory, which describes the scattering of a **PW** by a single sphere [30–33]. The electric field must satisfy the vector wave equation, $\nabla^2 \vec{E} + k^2 \vec{E} = \vec{0}$, where k is the **wave number**. (The same applies to the magnetic field (\vec{H}), but we will leave \vec{H} out of the discussion, because it may always be derived from \vec{E} by taking the curl: $i\omega\mu\vec{H} = \nabla \times \vec{E}$, where ω is the wave frequency and μ is the (magnetic) **permeability**.) A complete set of orthogonal basis functions that solve the vector wave equation, are the **Vector Spherical Harmonic (VSH)**: \vec{N}_{pmn} and \vec{M}_{pmn} . Given an incident field travelling in the \hat{z} direction and polarised in the \hat{x} direction, $\vec{E}_i = E_0 e^{ikz} \hat{x}$, the scattered field may be expanded in terms of the **VSHs**:

$$\vec{E}_s(\vec{r}) = \sum_{n=1}^{\infty} E_n \left(ia_n \vec{N}_{e1n}^{(3)}(\vec{r}) - b_n \vec{M}_{o1n}^{(3)}(\vec{r}) \right), \quad (4.2)$$

where $E_n = E_0 i^n (2n+1) / n(n+1)$ is just a prefactor, \vec{r} denotes that the functions depend on position, the superscript “(3)” denotes the usage of the **spherical Bessel function** of the third kind, and a_n and b_n are the Mie scattering coefficients. μ can be neglected, as its influence is minor for most media: $\mu_{\text{sphere}} \approx \mu_{\text{surroundings}} \approx \mu_0$.

When a **Far-Field (FF)** approximation is made, the infinite sum in Eq. (4.2) reduces to a single term, and the scattered field becomes an outgoing spherical wave:

$$\begin{bmatrix} E_{s\parallel} \\ E_{s\perp} \end{bmatrix} = \frac{e^{ik(r-z)}}{-ikr} \begin{bmatrix} S_2 & 0 \\ 0 & S_1 \end{bmatrix} \begin{bmatrix} E_{i\parallel} \\ E_{i\perp} \end{bmatrix}, \quad (4.3)$$

where E_{\parallel} and E_{\perp} are the component parallel and orthogonal to the scattering plane respectively, $[S]$ is the **amplitude scattering matrix** which for spherical particles only depends on the **scattering angle** θ_S and properties of the spherical particle, and r is the radial coordinate (i.e., the distance from the scatterer).

4.2.3. FLUID DYNAMICS

In the present work, we use a simple time-dependent flow in a cylindrical geometry:

$$u(r, t) = v(r)F(t), \quad (4.4)$$

where u is the axial velocity, $v(r)$ is the radial velocity profile and $F(t)$ is a dimensionless temporal modulation with a mean of 1.

To study an actual heartbeat, $F(t)$ will be read from a lookup table which contains the shape of a realistic heartbeat, with the same peak-to-peak amplitude (0.75) as in Baker et al. [34]. For the simpler sinusoidal case, we take $F(t) = A \sin(2\pi f t) + 1$, with $2A = 0.75$. The particle positions are integrated in time using the Euler forward scheme with dimensionless timestep $\Delta t^* = f\Delta t = 5 \cdot 10^{-4}$, which yields a maximum relative discretisation error of 0.1%.

The exact solution for the radial velocity profile in a cylinder is **Hagen-Poiseuille flow**,

$$v(r) = 2\langle v \rangle \left(1 - \left(\frac{r}{R} \right)^2 \right), \quad (4.5)$$

where $\langle v \rangle$ is the mean velocity, and R is the radius of the cylinder. For this realistic flow profile, there will be relative motion between the scatterers and there will therefore be

speckle boiling. To investigate its influence, we will compare the results with plug flow: $\nu(r) = \langle \nu \rangle$.

4.2.4. DATA ANALYSIS

To extract useful information from our simulated speckle images, three factors in particular are important: (1) speckle boiling causes temporal noise, (2) the camera should be sufficiently big with a sufficient resolution, and (3) for a large camera the speckle contrast should be calculated using [windowing](#).

First, speckle boiling is a physical noise factor caused by the relative motion of the scatterers [11], such as is the case in a fluid. In this work, we will study flow with and without speckle boiling, as was discussed in the previous section, which enables us to determine its influence.

Second, to mitigate [statistical noise](#), a sufficient number of speckles must be captured, and a sufficient number of pixels should be used to represent each speckle (i.e., resolution). The first ensures that the speckle space is well-represented, and thus that the data samples are uncorrelated; the latter ensures that speckles are not smoothed over the finite area of a pixel, because that artificially reduces the measured K for which needs to be corrected [35, 36]. For a real camera of 1024^2 pixels, it was found that about 4^2 pixels per speckle suffices for obtaining a good result [36, 37]. For our simulated camera, however, we are realistically limited to about 256^2 pixels by computational constraints¹. Using 256^2 pixels with 4^2 pixels per speckle, we obtained merely a noise signal for K , which indicates bad statistics.

To overcome this, we instead have our simulated camera [underresolve](#) the speckles, typically using merely $(1/5)^2$ pixels for each speckle in this paper. One cannot do this with a real camera, as this would artificially reduce K , because of spatial averaging over the finite pixel size. However, our simulated pixels are infinitesimal points in space. Thus the underresolving in our simulations is equivalent to using infinitesimal pixels whose separation is much greater than the typical speckle size, as is recommended by Skipetrov et al. [35]. In that manner, the simulated camera effectively samples an area 400x larger than it could possibly have for resolved speckle². Therefore, by underresolving the speckles, we retain all intensity fluctuations, while increasing our statistical sample size.

Third, since the amplitude scattering matrix of a sphere in Eq. (4.3) depends on the scattering angle, $\langle I \rangle$ will generally not be constant across an image, which artificially increases σ_I . Therefore, applying Eq. (4.1) directly will give a larger value for K than it should have been. This is especially true for a large camera, such as our simulated camera. If the system is sufficiently dense (i.e., high particle concentration), singly scattered light will be negligible compared to multiply scattered light. For multiply scattered light, the light is incident from random directions, resulting in a randomly distributed θ_s and thereby averaging out the effect of $[S](\theta_s)$.

¹With our settings, 32841 instantaneous optics simulations are performed for each simulation. Using 32 cores of a 2.4 GHz AMD Opteron 6234 processor, the simulation time for 256^2 pixels is 180 hours. The runtime scales linearly with the number of pixels (so 512^2 pixels would take four times longer), and scales perfectly with the number of computing cores (so using merely 1 core would take 32 times longer).

²As was discussed in the previous paragraph, using 4^2 pixels per speckle suffices for resolved speckle. We use $(1/5)^2$, which means that with the same total number of pixels, we observe a $5^2 \cdot 4^2 = 400$ times larger area.

However, for relatively dilute experiments, such as studied in our simulations due to computational constraints, single scattering contributes significantly. To overcome the issue at hand, we use local speckle contrast analysis [38], in which K is calculated through windowing, and then averaged to obtain the (average) speckle contrast of the whole image:

$$K = \frac{1}{M_x M_y} \sum_{x=0}^{M_x-1} \sum_{y=0}^{M_y-1} K_{x,y}, \quad (4.6)$$

where $M_{x/y}$ is the number of pixels in the x/y -direction of the camera. We will discuss the required window size in Sec. 4.4.1.

4.3. CODE DESCRIPTION

Our code³ comprises three parts: first CFD is used to evolve the particles in time, then the particle positions are extracted from the fluid simulation and processed to be used as the input for the optics code, and lastly a Mie-based optics code is used to compute the scattering of an incoming PW by the collection of particles.

4.3.1. COMPUTATIONAL FLUID DYNAMICS (CFD)

To obtain the flow field and particle movements, one can readily apply CFD, in which the discretized Navier-Stokes equations describing fluid momentum and mass conservation are solved numerically. Particles are typically simulated using Lagrangian particle tracking. However, since the flow considered in this paper is rather simple, we use the exact solution of the Navier-Stokes equations for the velocity of the particles instead (see Sec. 4.2.3). When a particle leaves the cylinder, it is teleported back to the entrance at the same radial and polar position (i.e., cyclic boundary conditions).

Regardless, our code is designed to be compatible with any existing CFD code (e.g., OpenFOAM). This is possible, because the speed of light is very large. Therefore, the particles cannot move a fraction of λ in the time δt it takes the light to scatter off of all particles (i.e., $v\delta t \ll \lambda$ results in $v \ll 2 \cdot 10^2$ m/s for the case of our interest, whereas $v \sim 1$ m/s). Consequently, CFD and the optics code are one-way coupled: CFD does not depend on the optics code, but its output serves as the input of the optics code.

4.3.2. OPTICS

Our optics code uses the Mie FF solution, Eq. (4.3), to compute the scattered light of each particle separately, while explicitly keeping track of the phase. The required Mie scattering coefficients in Eq. (4.2) are computed using the *bhmie.f90* script from the book of Bohren & Huffman [31], using the cutoff index n_C as was found empirically by Wiscombe [39]. Computing the Mie solution for all of space is very computationally demanding, but luckily it only needs to be evaluated at the points of interest, being the individual points of our virtual camera (i.e., pixels of zero area), and at the positions of every particle for multiple scattering.

Multiple scattering is implemented iteratively. In the first iteration, the incident laser

³Our code (see Chap. 2) has been published open-source, see the [List of Publications](#) on page 137.

light is scattered via each particle l to each of the $N - 1$ other particles $i \neq l$:

$$\vec{E}_{il}^0 = \text{scatter}_{l \rightarrow i}(\vec{E}_{\text{incident}}), \quad (4.7)$$

where the “scatter” operation refers to Eq. (4.3). In successive iterations p , every particle i then has $N - 1$ incoming waves from source particles $l \neq i$, which it should scatter to all $N - 1$ other particles $j \neq i$:

$$\vec{E}_{ji}^p = \sum_{l \neq i} \vec{E}_{jil}^p, \quad (4.8)$$

$$\vec{E}_{jil}^p = \text{scatter}_{i \rightarrow j}(\vec{E}_{il}^{p-1}). \quad (4.9)$$

This process includes **backscattering** (i.e., $j = l \neq i$). The iterative process is repeated until the maximum of the magnitudes of all scattered electric fields \vec{E}_{ji}^p , is a factor 10^8 smaller than the incident light, which for our simulations results in about 6-7 iterations. Subsequently, all (multiply) scattered fields \vec{E}_{ji}^p are scattered to each of the M camera pixels c :

$$\vec{E}_{ci} = \sum_{l \neq i} \text{scatter}_{i \rightarrow c} \left(\sum_p \vec{E}_{il}^p \right). \quad (4.10)$$

Finally, the intensity at each pixel K can be computed:

$$I_c = \left| \sum_i \vec{E}_{ci} \right|^2. \quad (4.11)$$

The **(computational) complexity** of the resulting algorithm is $N^2(N + M)$, to be repeated for each timestep. The code is perfectly parallel (i.e., using x cores is x times faster), because a great number of independent instantaneous simulations are performed.

Through our iterative process, two implicit (and arguably too strong) assumptions / simplifications are made. Firstly and most strongly, we use the Mie **FF** solution Eq. (4.3) at the length scale of the **interparticle distance**. It is clear that this assumption is easily violated: for particle radius $a = 4 \mu\text{m}$ and $\lambda = 600 \text{ nm}$, the interparticle distance should be $\mathcal{L} \gg 0.1 \text{ mm}$ to satisfy the assumption. However, blood has a **hematocrit** of $\sim 50\%$, meaning the typical distance between adjacent **RBCs** is of the order of the particle radius. Although this assumption is not satisfied for true blood, it is still satisfied in our simulations for 95% of the interparticle distances ($\langle \mathcal{L} \rangle = 3.45 \text{ mm}$), because we are limited to relatively few particles due to computational constraints. Therefore, this assumption does not affect our results at present. The second assumption is that Mie theory requires an incoming **PW**; therefore, we approximate the outgoing spherical wave Eq. (4.3) of the first particle as a **PW** at the position of the second particle:

$$\Psi(r) = \frac{e^{ikr}}{kr} \approx \Psi(z) = e^{ikz} \frac{e^{ikrcurs}}{k\mathcal{L}} \left(1 - \frac{z}{\mathcal{L}} \right). \quad (4.12)$$

This is a **PW** provided that $a \ll \mathcal{L}$, which is much more easily satisfied than the previous assumption.

The scattering matrix must be computed $N^2(N + M)$ times, comprising over 90% of the computational effort of the code. Since we had made a **FF** assumption, the scattering matrix only depends on the scattering angle. Therefore, we precompute it with 100 samples per degree, allowing for accurate interpolation, and yielding a speedup of a factor ~ 10 . In conclusion, despite some assumptions being arguably too simplifying, they enable us to simulate time-dependent laser speckle imaging within a feasible computational effort.

As an alternative to our approach, one could instead use more sophisticated methods such as the **T-matrix method**. With some adaptations, existing T-matrix codes – such as GMM [40] or FaSTMM [41] – could be implemented within our combined fluids and optics framework by replacing the core calculation routines of our optics code. Using the T-matrix method, the above **FF** assumption is eliminated: the calculated multiply scattered field is exact. It would even become possible to study non-spherical particles. The FaSTMM method uses a multipole expansion to accelerate the T-matrix method. It was developed after we had first developed our code, and has a computational complexity of $O(f(N) \cdot N \cdot \log N)$ [42], while our code has $O(\sim N^3)$. Here, $f(N)$ is the number of iterations needed for their iterative matrix inversion, which depends on N in an unknown complicated manner. While benchmarks are not given, and we cannot compare the complexities due to the unknown $f(N)$ parameter, the FaSTMM was used on a supercomputer to compute the instantaneous scattering intensity of a cluster of up to $N = 10^5$ particles [42], which is very promising. However, a single (temporal) simulation of ours requires $O(10^4)$ individual scattering simulations (cf. Fig. 4.2), and will furthermore need to be repeated for each pixel of the simulated camera. Therefore, we had currently settled on less particles, and some assumptions to make our simulations computationally feasible. Furthermore, we will argue in the following section that our simulations are already sufficiently accurate for our purposes. Nevertheless, future work should investigate the present capabilities of the FaSTMM method.

4.4. RESULTS

All simulation parameters are summarised in Tab. 4.1 for reference.

Figs. 4.3 show several speckle figures. Instantaneous (i.e., no camera integration) speckle is shown in Fig. 4.3a. In this figure, the typical speckle is 4 ± 1 by 5 ± 1 pixels in size, which translates to $16 \pm 3.9 \mu\text{m}$ by $78 \pm 16 \mu\text{m}$. Theoretically, the speckle size should correspond roughly to the characteristic width of the **point-spread function (PSF)** of the **aperture** [19]:

$$d_{\text{speckle}} \sim \frac{\lambda z}{D}, \quad (4.13)$$

where z is the distance between the object and image plane, and D is the aperture diameter. Note that in our simulations the ‘aperture’ is the cylinder’s frontal area: 1 cm by 2 mm. Since our aperture has an aspect ratio of 5, the speckles have aspect ratio 1/5. That is why we chose our camera to be rectangular with aspect ratio 4, as to measure (almost) circular speckles. Using the settings in Tab. 4.1, Eq. (4.13) results in $13 \mu\text{m}$ by $67 \mu\text{m}$. Especially since we only compare a ‘characteristic’ width, our results correspond well with

Table 4.1: Simulation Parameters

Optics	Refractive index	$n_{\text{sphere}} = 1.52$
		$n_{\text{medium}} = 1$
	Wavelength	$\lambda = 532 \text{ nm}$
Flow System	Fluid mean velocity	$\langle v \rangle = 1 \text{ m/s}$
	Flow signal frequency	$f_{\text{sinusoidal}} = 1 \text{ Hz}$
		$f_{\text{heartbeat}} = 1.20 \text{ Hz}$
	Particle radius	$a = 4 \text{ }\mu\text{m}$
	Number of particles	$N = 100$
	Radius cylinder	$R = 1 \text{ mm}$
	Length cylinder	$L = 1 \text{ cm}$
Camera	Number of pixels	$M = 128 \times 128$
	Physical size ^a	$1.25 \text{ cm} \times 5.0 \text{ cm}$
	Distance from cylinder	25 cm
Simulation	Camera integration time	$\Delta t_{\text{int}} = 100 \text{ }\mu\text{s}$
	# integration samples	$n_{\text{s,int}} = 40$
	Total simulation time	$T = 40 \text{ periods}$
	Data sampling rate	$20 \text{ samples/period}$

^aNote that our simulated camera size is without any lenses.

theory, which validates the interferometric behaviour of our code⁴.

Fig. 4.3b shows the corresponding time-integrated speckle image. For our settings, the speckles blur over $\sim 10\%$ of the camera's width, in the direction of motion. Note, however, that these resolved speckle figures were created with a 1 mm by 4 mm camera for the sake of visualization, whereas the following results use unresolved speckle (as was discussed in Sec. 4.2.4), such as is shown in Fig. 4.3c.

4.4.1. CONVERGENCE

To obtain accurate results, several factors are important, which we will now discuss. Firstly, it is important to have a sufficient number of pixels (M) (i.e., spatial resolution) in combination with a sufficiently large camera (to sample enough of speckle space to obtain statistical significance). Secondly, a sufficient number of camera integration samples ($n_{\text{s,int}}$) (i.e., temporal resolution) is required to mimic a real camera. Thirdly, an appropriate camera integration time (Δt_{int}) should be used, depending on the characteristic velocity ($\langle v \rangle$). We will not discuss the latter in this paper, other than noting that $\Delta t_{\text{int}} = 100 \text{ }\mu\text{s}$ is appropriate for $\langle v \rangle = 1 \text{ m/s}$, given that we obtain good results (whereas we have found that either a too large or a too small Δt_{int} results in noise).

Fig. 4.4a shows the effect of the number of pixels (M), and the used windowing size (cf. Eq. (4.6)) on the speckle contrast of an instantaneous simulation. As was discussed in Sec. 4.2.1, we may expect $K = 1$ for fully-developed speckle, but since we have a minor ($\sim 10\%$) contribution of multiple scattering, a value slightly below 1.0 may be expected. The figure shows that when no windowing is used, the computed K is significantly too

⁴For further optics code validation, see Chap. 3.

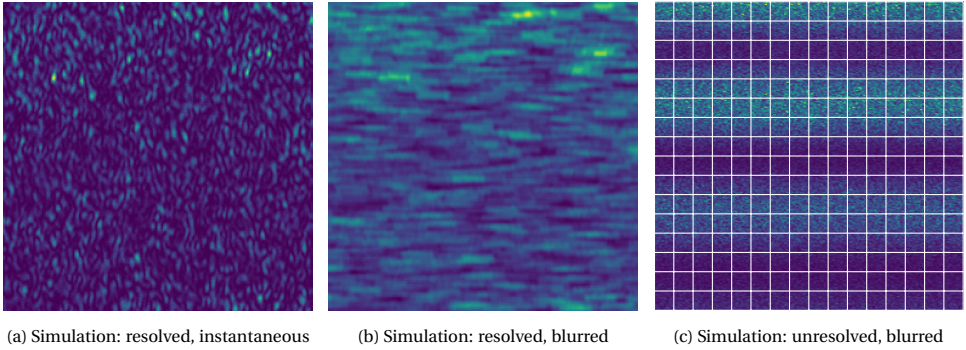


Figure 4.3: A few characteristic speckle figures: the influence of the camera integration time, and resolved versus unresolved speckle. (b) is the temporally blurred version of (a). Note that the color ranges differ: absolute values are meaningless, and the blurred image (b) has a factor 10 lower intensity range than (a), which would have caused (b) to appear mostly dark blue. The 16×16 grid used for local speckle contrast analysis is additionally shown in (c). Deviations from Tab. 4.1: the camera size in (a) and (b) is $1 \text{ mm} \times 4 \text{ mm}$, and all three figures use 256^2 pixels.

4

high. The reason for obtaining $K > 1$ is that our camera is sufficiently large for interferometric fringes to be visible (see Fig. 4.3c), the cause of which was discussed in the third point of Sec. 4.2.4. The fringes increase σ_I , and thus also K cf. Eq. (4.1). By using an increasing number of smaller windows, we find that K decreases. This happens because we effectively zoom-in on the fringes, leaving only the speckles to be seen (see the grid drawn on Fig. 4.3c). Therefore, windowing with sufficiently small windows is a good thing. This is evidenced by the convergence to a value just below $K = 1.0$, up to “grid 64^2 ”.

However, as we use increasingly small windows for “grid 128^2 – 512^2 ”, K starts to become increasingly underestimated. The same effect is seen in the bottom-left part of the figure. This happens because we then effectively zoom-in on the speckles, which results in a reduced σ_I and therefore a reduced K , and will eventually result in $K = 0$ (i.e., in the limit of infinitely small windows). Additionally, the point at which windows become too small is relative to the speckle size, because a sufficient number of speckles should be visible in a window to accurately calculate K . For example, at 4096^2 (2^{12}) pixels, speckles are about 6.4^2 pixels in size; thus using windows of 8^2 pixels (as is the case for “grid 512^2 ”) is clearly too small. The figure shows that this effect begins roughly at “grid 128^2 ”, corresponding to a window-size-to-speckle-size ratio of 5. Therefore, we conclude that this ratio should be larger than ~ 5 to obtain quantitative results. Furthermore, all lines are consistently satisfyingly close to their asymptotic value when windows of at least 8^2 pixels are used, which is consistent with the experimental heuristic of using 5^2 – 7^2 pixels as a compromise between spatial resolution (i.e., small windows) and sufficient statistics (i.e., large windows) [20] to obtain qualitative results.

Consequently, a balance between these two opposing effects is required. The windows corresponding to “grid 64^2 ” and “grid 32^2 ” differ by merely $\sim 1.2\%$, and “grid 16^2 ” deviates by merely $\sim 3.1\%$ from “grid 64^2 ”, which indicates convergence in that middle range. Given the computational constraints, we decided to go for 128^2 (2^7) pixels, for

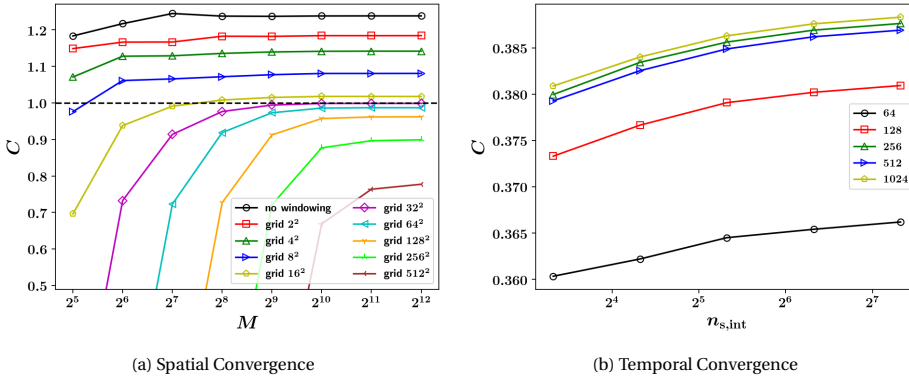


Figure 4.4: The effect of the spatial (number of pixels, M) and temporal resolution (number of sampling points, $n_{s,int}$), during the constant camera integration time, cf. Tab. 4.1), and the effect of windowing on the computed speckle contrast (K). The notation “grid 16^2 ” denotes subdividing the image in a 16×16 grid of calculation windows (i.e., windows of 8^2 pixels for 128^2 (2^7) total pixels), as is illustrated in Fig. 4.3c.

which a 16×16 grid (i.e., 8×8 -pixels windows) is most appropriate with a $\sim 2.6\%$ error with respect to its value at 4096^2 (2^{12}) pixels, and $\sim 0.4\%$ with respect to the asymptote of “grid 64^2 ”.

In Fig. 4.4b the effect of the number of camera integration samples ($n_{s,int}$) on K for a temporal simulation may be seen. For the sake of completeness, the result is also shown for a varying number of pixels. The first thing to note is that the convergence behaviour is independent of M , indicating that spatial and temporal convergence may be studied independently. The 128^2 pixels case deviates merely $\sim 1.2\%$ from those with more pixels, indicating that 128^2 pixels is also appropriate for a temporal simulation. For $n_{s,int} = 10$, we have a $\sim 2\%$ error relative to the $n_{s,int} = 160$ case, which reduces to $\sim 0.5\%$ for $n_{s,int} = 40$. As a general rule of thumb, we found that one needs a higher $n_{s,int}$ for a smaller camera. For our present camera, $n_{s,int} = 10$ would suffice, but in line with our simulations with a smaller camera, we went for $n_{s,int} = 40$ in the present work as well.

4.4.2. EXTRACTING A HEARTBEAT

As was discussed in Sec. 4.2.3, we study four distinct cases: sinusoidal plug flow, sinusoidal Poiseuille flow, heartbeat plug flow, and heartbeat Poiseuille flow. Tracer particles suspended in each flow were simulated, after which our LSI code was used to simulate speckle.

Figs. 4.5 show $K(t)$ and the frequency spectra for the sinusoidal cases. For plug flow (Fig. 4.5b), we obtain a perfectly periodic signal. This happens because we obtain the very same particle positions for successive cycles due to our cyclic BCs. For Poiseuille flow (Fig. 4.5c) on the other hand, we retrieve a periodic signal, with some noise. Most of that noise may be attributed to speckle boiling. In the frequency spectra it may be seen that the main frequency peak of the input signal is easily reconstructed, for plug flow and Poiseuille flow alike. It may be seen that the effect of speckle boiling on the frequency spectrum is minor noise with roughly the same amplitude at all frequencies, which is

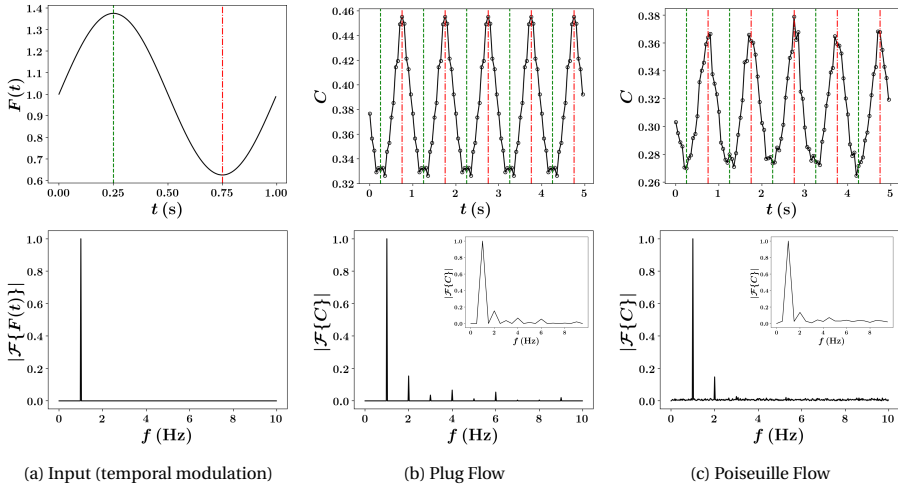


Figure 4.5: Simulation results for the sinusoidally modulated flow. Top: obtained speckle contrast time series, shown for five simulated periods. Bottom: its frequency spectrum obtained from forty simulated periods. Insets on bottom: the frequency spectrum as obtained from merely two simulated periods.

easy to filter out if we would want to.

Unlike the input signal, the output signal also shows a frequency peak at twice the main frequency. This is caused by the fact that $K(t)$ is broad at its troughs, but narrow at its crests. This widening and narrowing effect may be created by superimposing a cosine of twice the sine's frequency. $K(t)$ shows this behaviour, unlike the input signal, because K does not simply scale linearly with velocity (u) [19]. Hence we may not expect $K(t)$ to be identically proportional to u . More specifically, for low velocities, K drops sharply from 1, whereas for high velocities K approaches the asymptotic value of 0 slowly. Thus changes at a low velocity (troughs of u ; crests of K) result in large changes in K , whereas changes at a high velocity (crests of u ; troughs of K) result in a smaller change in K . Therefore, the crests of K should theoretically be more narrow than its troughs – as is also observed.

The results for the heartbeat-modulated cases are shown in Figs. 4.6. Just like for the sinusoidal cases, $K(t)$ shows the same features as the input signal. That is, there is a clear mapping between all local minima and maxima, and crests of u again correspond to troughs of K and vice versa. For plug flow (Fig. 4.6b), the signal is nicely periodic with little noise. In the frequency spectrum it may be seen that the original main frequency is found, and the characteristic higher order frequencies are also retrieved. The relative peak heights are not identical as those of the input signal, but – as was also concluded for the sinusoidal case – they should not be, because K does not scale linearly with u . The little noise that is present, is caused by the different particle positions for each cycle, as with a period of 0.835 s the cyclic BCs do not result in identical particle positions in the next cycle, as had been the case for the sinusoidal modulation with a period of precisely 1 s.

For Poiseuille flow (Fig. 4.6c), we once again obtain a signal which is more noisy than

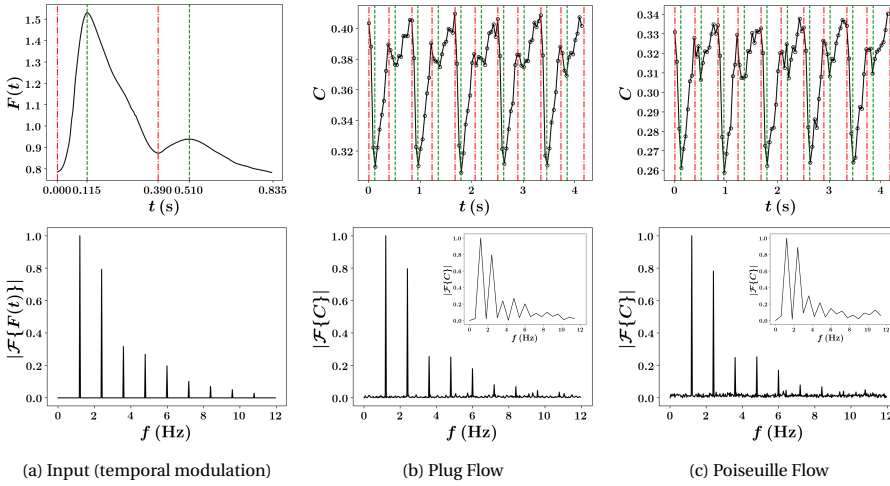


Figure 4.6: Simulation results, like Fig. 4.5 above, but now for a heartbeat-modulated flow.

plug flow, which may again be fully attributed to the speckle boiling associated with the Poiseuille flow profile. Taking the frequency spectrum of plug flow as a reference, it may be concluded that the effect of speckle boiling is to apply **spectral noise** independent of frequency, as was also observed for sinusoidal flow. The relative peak heights are within 2% of those of plug flow – so within our convergence errors – proving that speckle boiling has no significant effect on our ability to use **LSI** for studying the dynamics of a flow system.

Our group has previously applied the principles outlined in this paper to extract the heartbeat in an experimental setup [21]. The heartbeat was also measured in-vivo using this technique [29]. Our simulations compare well with those experimental results.

4.4.3. FUTURE WORK

The results presented thus far show the capability of our code to simulate **LSI**. As merely the first step, we have applied our **LSI** code to extract a heartbeat from a simulated flow, and studied the effect of (the noise induced by) speckle boiling. Clearly, simpler techniques such as light-absorption techniques are already able to do this, as only a (qualitative) sensitivity to fluctuations in blood density is required. The real power of **LSI** is that it is based on light scattering, which is sensitive to many more parameters, and may thus be developed to become a truly versatile measurement technique.

Quantitative local velocity measurements that can non-invasively monitor (opaque) turbid media might be possible, because speckles are primarily sensitive to the transverse direction of motion, and the speckle contrast (amongst other speckle metrics) is sensitive to the magnitude of velocity [19, 22]. When combined with regional laser Doppler techniques [20], which are sensitive to the longitudinal direction of motion, a three-dimensional flowmetry technique for turbid media might be developed. Light scattering is also sensitive to the **refractive index** of the **RBCs**, which yields information about their oxygen content. **LSI** may also be used as a cheap technique for **blood perfu-**

sion measurements [38]. Further possibilities include, but are not limited to: premature detection of [atherosclerosis](#), measuring the dynamic [morphology](#) of [RBCs](#), and distinguishing between different depths in complex flow networks. The primary benefit of our new code is that we can enable/disable and vary parameters at will, allowing us to study their effect. For future work, our new code may thereby be used to study and develop said applications.

4.5. CONCLUSIONS

In this paper, we have developed and applied a computational model for simulating the interference of multiply-scattered coherent light by moving particles. The model's purpose is to help us further develop [Laser Speckle Imaging \(LSI\)](#) as a quantitative imaging technique. The model is based on Mie theory, which provides an exact solution for the scattering of a [PW](#) by a single sphere. The fields of all particles are gathered at the pixels of our simulated camera by adding them vectorially, and then squaring them to obtain the intensity. To incorporate multiple scattering, we devised an iterative process in which each particle not only scatters to every pixel, but also to every other particle. The process is repeated until successive scattering orders become negligible. Simplifying assumptions were made to make the process computationally feasible: we assumed that particles are sufficiently far apart (i.e., in each other's [FF](#)) and sufficiently small, so that they see scattered fields approximately as incoming [PWs](#). Although these assumptions affect the [speckle pattern](#), they do not restrict us from obtaining meaningful results.

To show that our simplifications are not limiting, we have applied our model to a case study resembling blood flow: spherical particles of several micrometer moving in a cylindrical geometry with 1 m/s mean velocity. The flow system was modulated with a 1 Hz sinusoidal signal, and a 1.20 Hz heartbeat signal. Using speckle blurring with a camera integration time of 100 μ s, we have successfully retrieved the main frequency modes of the input signal from the speckles. We have studied the influence of speckle boiling on the quality of the result by comparing plug flow with a Poiseuille flow profile, and found that speckle boiling applies uniform spectral noise to the signal. For our present case, its effect was of the same order as our measurement uncertainty, $\sim 2\%$, and thus speckle boiling was not found to be detrimental for the result. Our results prove that our numerical model is capable of simulating the whole [LSI](#) process, and is therefore a useful new tool for improving [LSI](#) as a quantitative [indirect imaging](#) technique.

BIBLIOGRAPHY

1. Tuchin, V. *Tissue Optics: Light Scattering Methods and Instruments for Medical Diagnosis* (SPIE press Bellingham, 2007).
2. Boas, D. A., Campbell, L. E. & Yodh, A. G. Scattering and Imaging with Diffusing Temporal Field Correlations. *Physical Review Letters* **75**, 1855 (1995).
3. O’leary, M. A., Boas, D. A., Chance, B. & Yodh, A. G. Refraction of Diffuse Photon Density Waves. *Physical Review Letters* **69**, 2658 (1992).
4. Pine, D. J., Weitz, D. A., Chaikin, P. M. & Herbolzheimer, E. Diffusing-Wave Spectroscopy. *Physical Review Letters* **60**, 1134 (1988).
5. Stephen, M. J. Temporal fluctuations in wave propagation in random media. *Physical Review B* **37**, 1 (1988).
6. Durduran, T., Choe, R., Baker, W. B. & Yodh, A. G. Diffuse Optics for Tissue Monitoring and Tomography. *Reports on Progress in Physics* **73**, 076701 (2010).
7. Welch, A. J., van Gemert, M. J. C., *et al.* *Optical-Thermal Response of Laser-Irradiated Tissue* (Springer, 2011).
8. Sassaroli, A. & Martelli, F. Equivalence of four Monte Carlo methods for photon migration in turbid media. *JOSA A* **29**, 2110–2117 (2012).
9. Davis, M. A. & Dunn, A. K. Dynamic light scattering Monte Carlo: a method for simulating time-varying dynamics for ordered motion in heterogeneous media. *Optics Express* **23**, 17145–17155 (2015).
10. Bosschaart, N., Edelman, G. J., Aalders, M. C. G., van Leeuwen, T. G. & Faber, D. J. A Literature Review and Novel Theoretical Approach on the Optical Properties of Whole Blood. *Lasers in Medical Science* **29**, 453–479 (2014).
11. Asakura, T. & Takai, N. Dynamic laser speckles and their application to velocity measurements of the diffuse object. *Applied Physics* **25**, 179–194 (1981).
12. Dainty, J. C. in *Topics in Applied Physics* 9 (Springer, Berlin, Heidelberg, 1975).
13. Van der Kooij, H. M. & Sprakel, J. Watching paint dry; more exciting than it seems. *Soft Matter* **11**, 6353–6359 (2015).
14. Van der Kooij, H. M., Fokkink, R., van der Gucht, J. & Sprakel, J. Quantitative imaging of heterogeneous dynamics in drying and aging paints. *Scientific Reports* **6**, 34383 (2016).
15. Boas, D. A. & Dunn, A. K. Laser speckle contrast imaging in biomedical optics. *Journal of Biomedical Optics* **15**, 011109 (2010).
16. Zakharov, P. *et al.* Dynamic laser speckle imaging of cerebral blood flow. *Optics Express* **17**, 13904–13917 (2009).

17. Heckmeier, M., Skipetrov, S. E., Maret, G. & Maynard, R. Imaging of dynamic heterogeneities in multiple-scattering media. *JOSA A* **14**, 185–191 (1997).
18. Dunn, A. K. Laser speckle contrast imaging of cerebral blood flow. *Annals of Biomedical Engineering* **40**, 367–377 (2012).
19. Duncan, D. D. & Kirkpatrick, S. J. Can laser speckle flowmetry be made a quantitative tool? *J. Opt. Soc. Am. A* **25**, 2088–2094 (2008).
20. Briers, D. *et al.* Laser speckle contrast imaging: theoretical and practical limitations. *Journal of Biomedical Optics* **18**, 066018 (2013).
21. Nemati, M. *et al.* Application of full field optical studies for pulsatile flow in a carotid artery phantom. *Biomedical optics express* **6**, 4037–4050 (2015).
22. Fercher, A. F. & Briers, J. D. Flow visualization by means of single-exposure speckle photography. *Optics Communications* **37**, 326–330 (1981).
23. Briers, J. D. & Webster, S. Laser speckle contrast analysis (LASCA): a non-scanning, full-field technique for monitoring capillary blood flow. *Journal of Biomedical Optics* **1**, 174–180 (1996).
24. Pedersen, H. M. The roughness dependence of partially developed, monochromatic speckle patterns. *Optics Communications* **12**, 156–159 (1974).
25. Goodman, J. W. in *Laser Speckle and Related Phenomena* 9–75 (Springer, 1975).
26. Li, J., Yao, G. & Wang, L. V. Degree of polarization in laser speckles from turbid media: Implications in tissue optics. *Journal of Biomedical Optics* **7**, 307–312 (2002).
27. Yoshimura, T. Statistical Properties of Dynamic Speckles. *JOSA A* **3**, 1032–1054 (1986).
28. Bandyopadhyay, R., Gittings, A. S., Suh, S. S., Dixon, P. K. & Durian, D. J. Speckle-visibility spectroscopy: A tool to study time-varying dynamics. *Review of Scientific Instruments* **76**, 093110 (2005).
29. Nemati, M., Kenjeres, S., Urbach, H. P. & Bhattacharya, N. Fractality of pulsatile flow in speckle images. *Journal of Applied Physics* **119**, 174902 (2016).
30. Mie, G. Beiträge zur Optik trüber Medien, speziell kolloidaler Metallösungen. *Annalen der Physik* **330**, 377–445 (1908).
31. Bohren, C. F. & Huffman, D. R. *Absorption and Scattering of Light by Small Particles* (John Wiley & Sons, 2008).
32. Stratton, J. A. *Electromagnetic Theory* (John Wiley & Sons, 2007).
33. Hulst, H. C. *Light Scattering by Small Particles* (Courier Corporation, 1981).
34. Baker, W. B. *et al.* Noninvasive optical monitoring of critical closing pressure and arteriole compliance in human subjects. *Journal of Cerebral Blood Flow & Metabolism* **37**, 2691–2705 (2017).
35. Skipetrov, S. E. *et al.* Noise in laser speckle correlation and imaging techniques. *Opt. Express* **18**, 14519–14534 (2010).
36. Thompson, O., Andrews, M. & Hirst, E. Correction for spatial averaging in laser speckle contrast analysis. *Biomedical Optics Express* **2**, 1021–1029 (2011).

37. Kirkpatrick, S. J., Duncan, D. D. & Wells-Gray, E. M. Detrimental effects of speckle-pixel size matching in laser speckle contrast imaging. *Optics Letters* **33**, 2886–2888 (2008).
38. Draijer, M., Hondebrink, E., van Leeuwen, T. & Steenbergen, W. Review of laser speckle contrast techniques for visualizing tissue perfusion. *Lasers in Medical Science* **24**, 639 (2009).
39. Wiscombe, W. J. Improved Mie scattering algorithms. *Applied Optics* **19**, 1505–1509 (1980).
40. Xu, Y.-L. & Gustafson, B. Å. S. A generalized multiparticle Mie-solution: further experimental verification. *Journal of Quantitative Spectroscopy and Radiative Transfer* **70**, 395–419. <https://scattport.org/files/xu/codes.htm> (2001).
41. Markkanen, J. & Yuffa, A. J. Fast superposition T-matrix solution for clusters with arbitrarily-shaped constituent particles. *Journal of Quantitative Spectroscopy and Radiative Transfer* **189**, 181–188. https://bitbucket.org/planetarysystemresearch/fastmm_v1.0 (2017).
42. Penttilä, A. *et al.* How much is enough? The convergence of finite sample scattering properties to those of infinite media. *Journal of Quantitative Spectroscopy and Radiative Transfer* **262**, 107524 (2021).

5

HOW VELOCITY AFFECTS THE SPECKLE CONTRAST

We study how the [speckle contrast](#) depends on scatterer velocity, with the goal of further developing [Laser Speckle Imaging \(LSI\)](#) as a quantitative measurement technique. To that end, we perform interferometric computer simulations on a dilute plug flow. The results of our numerical experiment, that we compare with known analytical expressions to confirm their veracity, match well at low velocities with the Gaussian expression. Finally, we address the issue of how velocity depends on [speckle decorrelation time](#), and show that the imaging-system-dependent speckle size is most likely the relevant connecting length scale.

This chapter was published previously: Van As, K., Simons, B. A., Boterman, J., Kleijn, C. R., Kenjeres, S. & Bhattacharya, N. (2022). *The dependence of speckle contrast on velocity: a numerical study*. [J. Eur. Opt. Society-Rapid Publ.](#) 2022, 18(2), 11.

5.1. INTRODUCTION

Laser Speckle Contrast Imaging (LSCI) is a promising technique for the **non-invasive** measurement of dynamic systems (i.e., **velocimetry**), such as blood flow [1–6]. When **coherent light scatters** off of particles, a **speckle image** is formed. When those particles are in motion, the speckles will be dynamic as well. The result is both speckle translation and speckle boiling [7, 8], with a characteristic speckle decorrelation time τ_c . When imaged with a camera with **exposure time** T , the resulting speckle image will undergo blurring, the amount of which depends on the particles' velocities. The blurring is quantified using the speckle contrast, K , thus providing a metric for velocity, V [9]. At present, this makes LSCI useful for relative velocity mapping [1]. Due to its simplicity, high spatial resolution, and low cost, LSCI has already been widely adopted [10–14].

However, quantitative measurements with LSCI have been elusive due to the lack of a method for quantitatively determining the velocity from K , which prevents us from making quantitative measurements with LSCI. Another optical technique for velocimetry is **Particle Image Velocimetry (PIV)**, which, although established, has the disadvantage that direct imaging is required and is thus invasive in nature. In a recent paper, the velocity profile was quantitatively reconstructed with the new optical speckle image velocimetry technique [15] that combines LSCI with PIV, but their technique relies on negligible speckle boiling, which is only attainable with invasive measurements. The sidestream dark field LSCI technique [16] still requires some direct imaging of the flow as well. Efforts have been made to overcome these problems for non-invasive measurements, such as improvements to the analytical relationship between K and τ_c [17, 18], studying the effect of the temporal correlation function of light [5, 19, 20], and using multiple exposure times [21, 22] or multiple wavelengths [23]. Although LSCI is promising, much work is still required to make it a fully quantitative measurement technique.

In this work, we continue the work of Duncan and Kirkpatrick [17] by investigating how K depends on τ_c and τ_c in turn on V . Once we accurately know these relationships and what they depend on, we can convert a measured K into the velocity of the scattering system, thus enabling us to make quantitative measurements with LSCI. To obtain those relationships, we perform computer simulations using our new in-house code [24].

5.2. SIMULATION

5.2.1. APPROACH

Our code (see Chap. 2) is based on **Mie theory**, which describes the scattering of a linearly polarised **plane wave** by a single homogeneous spherical particle. Using a **Far-Field (FF)** approximation, the plane wave that was scattered by a particle locally becomes a plane wave again. In that manner, **multiscattering** between particles is implemented iteratively, in which each particle scatters to each other particle, including **backscattering**, until successive **scattering orders** become negligible. Finally, all scattered fields are gathered at a two-dimensional grid of infinitesimal points (i.e., our “simulated camera”), at which the **intensity** I is calculated. Using a separate **CFD** code, we then evolve the particles in time. The instantaneous light scattering calculation is repeated at n_{int} rapid time intervals and then averaged over to mimic the finite **integration time** T of a camera. The result is a fully **interferometric** code, capable of simulating dynamic **speckle**.

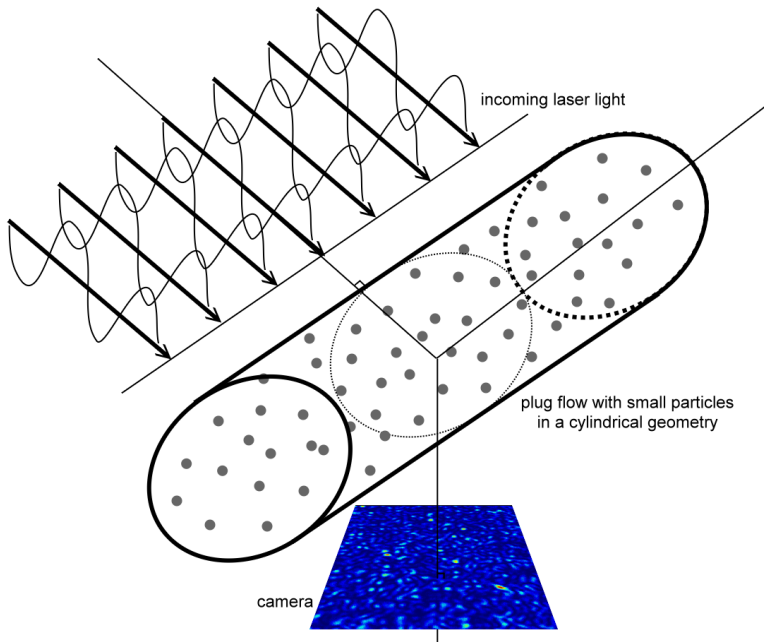


Figure 5.1: Simulation setup: a plane wave is incident on a cylindrical geometry filled with tiny spherical particles in motion. A ‘camera’, placed at a right angle, measures the resulting dynamic interferometric speckle pattern over time. Figure not to scale.

We do not simulate any kind of imaging system such as lenses. Consequently, we study **objective speckle** – as opposed to the **subjective speckle** that forms in the imaging plane of a lens. Since both types of speckle have similar dynamics, simulating lenses is irrelevant to our simulation.

Several simplifications were made that enable us to study dynamic systems within a reasonable computational time. The strongest is the aforementioned **FF** approximation in Mie theory. This is easily violated, as this requires an **interparticle distance** of $\vec{\lambda} \gg 0.1 \text{ mm}$ (i.e., for our parameters outlined below). The second part of the **FF** approximation is that the particle size should be $\ll \vec{\lambda}$, which is much more easily satisfied than the previous assumption. However, although these assumptions are not valid for, e.g., real blood flow ($\vec{\lambda} \sim 10^{-5} \text{ m}$), they are still satisfied in our simulations, because we are limited to relatively few particles by computational constraints. Thus strictly speaking our model is only applicable to sufficiently dilute flow, but it may be expected that the results on dynamic speckle imaging are more widely applicable nonetheless. More details about our code and the assumptions may be found in our previous paper [24].

To study how $K \equiv \sigma_I / \langle I \rangle$ depends on V , we use a simple cylindrical geometry with **plug flow** (i.e., a uniform constant velocity profile). The cylinder is 1 cm long with a 1 mm radius, which is characteristic for the **external carotid artery (ECA)**¹. The camera and the

¹LSCI until now has mostly been used to study blood perfusion from capillary beds [1], but the **ECA** is also a good candidate for this technique [25]

laser are placed at right angles, and also orthogonal to the cylinder's axis (see Fig. 5.1). 100 tracer particles with radius $4\ \mu\text{m}$ are randomly distributed over the geometry. When a particle leaves the cylinder, it is reinserted at the entrance at the same radial and polar position (i.e., cyclic BCs). Although our code is capable of simulating more complex geometries and flow profiles, we chose this simple setup as a first step to minimize the effect of **speckle boiling**. Effects of using a different flow profile on the noise induced by the associated increase in speckle boiling was studied in Chap. 4.

On the optics side of the code, we use a real **refractive index** of 1.52 for the spheres and 1.00 for the surrounding medium. The wavelength of illumination is 532 nm. The camera is placed at a distance of 25 cm from the cylinder, and is given a size of 1.25 cm by 5.00 cm with 128^2 pixels². With these settings speckles are underresolved, on average using merely 1 pixel for every 25 speckles (i.e., 0.2^2 pixels per typical speckle). Whereas an experiment should satisfy the **Nyquist criterion** as to prevent an artificial reduction of K due to spatial averaging over the finite size of a pixel [26], our simulation uses infinitesimal point pixels and thus does not have this problem. Consequently, we can use fewer pixels that are separated by multiple speckle sizes to obtain a better statistical representation of the speckle space while retaining all intensity fluctuations [24]. Finally, from the obtained speckle pattern, the **speckle contrast** is calculated using local speckle contrast analysis [20, 24] with windows of 8×8 pixels (see Sec. 4.2.4).

5.2.2. RESULTS

A study of the effect of velocity V and camera integration time T on the speckle contrast K is shown in Fig. 5.2. The simulations were performed with 10 different sets of random initial particle positions, which allowed us to calculate the systematic error caused by fluctuations in the precise particle positions that will always be present in experiments and simulations alike³. The data points in the figure are the resulting mean speckle contrasts, and the error bars show the resulting standard deviations. Additional errors are not incorporated into these error bars, such as due to spatial and temporal discretization (which are $\sim 2\%$ each [24]). The figure nicely shows that $K \approx 1$ at zero velocity, which is the expected value for **fully-developed static speckle** [27]. Actually, K is slightly ($\sim 1.2\%$) less than unity [24], but this is not substantial when compared to the uncertainties of discretization and of the random particle instantiations.

As either V or T is increased, K decreases because more motion is captured. Generally speaking, the error is also lower for higher V and T , presumably because for those situations averaging occurs over a larger range of particle positions, which renders the random particle instantiations less relevant.

We hypothesize that the relevant parameter should in fact be $d = VT$, which is the physical distance the particles have travelled during the camera integration time. Fig. 5.3 shows the same data as Fig. 5.2, but rescaled using d . Clearly, all data points nicely collapse onto a single master curve. In fact, in a simulation with the same initial particle instantiations, doubling either V or T gives precisely identical particle positions and thus identical speckle and K .

²We require a very large camera to capture objective speckle, as there are no lenses to converge the light.

³However, we do not yet know what parameters this error depends on. Thus we cannot assume that this error has the same magnitude for all simulation parameters, let alone in all experiments.

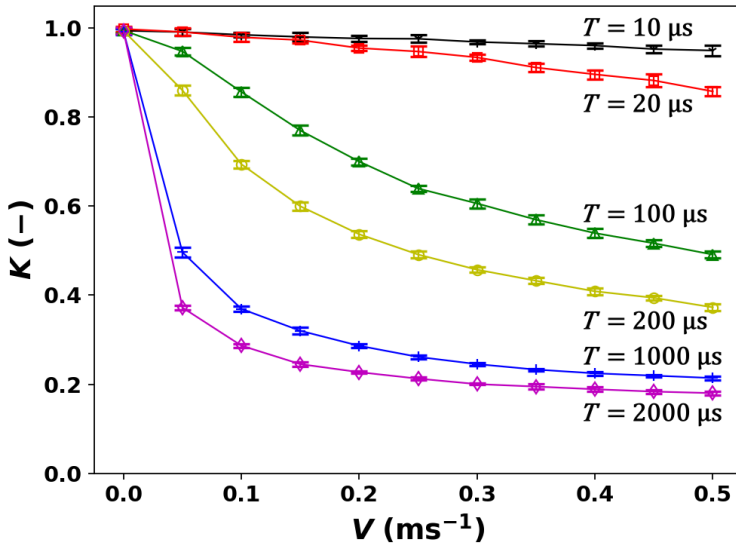


Figure 5.2: Speckle contrast K dependence on scatterer velocity V for various camera integration times T . The error bars show the spread (standard deviation) caused by 10 different sets of random initial particle positions.

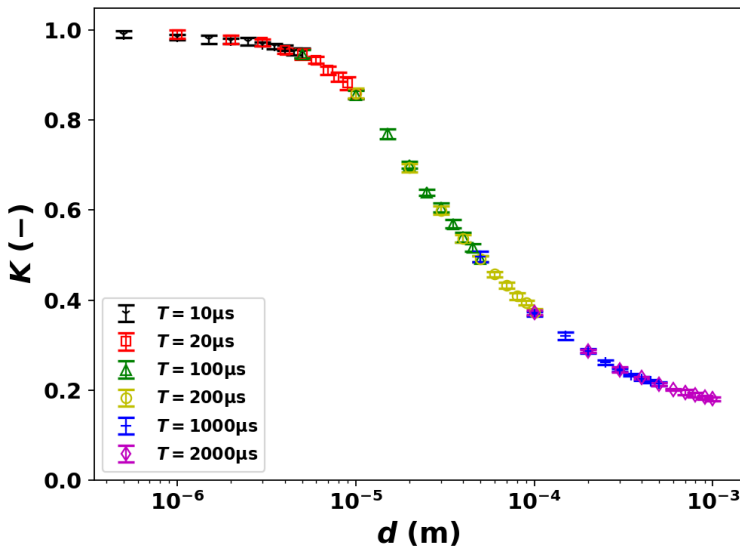


Figure 5.3: Speckle contrast K dependence on scatterer “distance travelled”, $d = VT$. The data points are from Fig. 5.2, and are shown to collapse onto a single master curve.

5.3. THEORETICAL COMPARISON

Several analytical expressions for K are already well-known [17, 19, 20]. As a numerical experiment, we compare our simulations with these analytical models as to confirm/determine their applicability. Whereas physical experiments are good at measuring at large integration times, our simulations can be used for very small integration times not yet approachable in experiments. More generally, simulations can be used for circumstances that are difficult to reach experimentally, and thereby compliment experimental results.

5.3.1. THEORY

SPECKLE CONTRAST DEPENDENCE ON DECORRELATION TIME

The analytical expressions are derived from the temporal fluctuation statistics of the speckles caused by the motion of the scatterers. Using the **autocovariance** of the temporal fluctuations $C_t^{(2)}(\tau)$, it is possible to integrate over a time period T to obtain the spatial variance σ_I of time-integrated speckle [20, 28], and thus also K :

$$\sigma_I^2(T) = \frac{2}{T} \int_0^T \left(1 - \frac{\tau}{T}\right) C_t^{(2)}(\tau) d\tau. \quad (5.1)$$

However, the difficulty in deriving an analytical expression is that the motion of the scatterers is usually a priori unknown or too complicated; therefore, $C_t^{(2)}(\tau)$ caused by said motion must be assumed.

When a Lorentzian **covariance** is assumed, the speckle contrast is:

$$K^2 = \beta \frac{\tau_c}{2T} \left[2 - \frac{\tau_c}{T} (1 - e^{-2T/\tau_c}) \right], \quad (5.2)$$

where β is a factor that corrects for the loss of correlation due to the ratio of pixel size to speckle size [20], with $\beta = 1$ for infinitesimal pixels. Analogously, for an assumed Gaussian covariance, it holds that:

$$K^2 = \beta \frac{\tau_c}{2T} \left[\sqrt{2\pi} \operatorname{erf} \left(\frac{\sqrt{2}T}{\tau_c} \right) - \frac{\tau_c}{T} (1 - e^{-2(T/\tau_c)^2}) \right]. \quad (5.3)$$

The Lorentzian equation is valid for unordered (**Brownian motion**), whereas the Gaussian equation is more appropriate for ordered motion. Since those two types of motion are statistically independent, reality is likely somewhere between these two limits [19].

However, it is not yet clear whether these relationships are truly applicable in practice. An arguably more appropriate relationship for blood flow was derived while assuming a constant velocity [29]:

$$K^2 = \beta \frac{\tau_c}{3.83T} \int_0^{3.83T/\tau_c} \left(\frac{2J_1(x)}{x} \right)^2 dx, \quad (5.4)$$

where $J_1(x)$ is the **Bessel function** of the first kind. The number 3.83 was introduced to define τ_c in Eq. (5.1) as the time τ after which $J_1(x) = 0$ for the first time. This curve follows the Gaussian curve closely for small T/τ_c , whereas it follows the Lorentzian for large

T/τ_c . This is sensible, because for small T/τ_c the motion is very ordered (\sim Gaussian), whereas for large T/τ_c the blurring caused by the accumulated speckle blurring is so large that we might as well have been looking at speckle boiling caused by unordered motion (\sim Lorentzian).

SCALING OF THE DECORRELATION TIME WITH VELOCITY

These expressions all give K as a function of τ_c , whereas the goal is to measure V . To that end, an expression for $\tau_c(V)$ is needed. It was postulated that τ_c scales inversely with V : [17]

$$\tau_c = \frac{w}{V}, \quad (5.5)$$

where the proportionality constant w should be a characteristic length scale; however, its value is still being disagreed upon by two orders of magnitude [5]. The first proposal simply used the wavelength, $w_\lambda = \lambda/2\pi$, although without any derivation [1, 17]. Recent experimental research on speckle dynamics still uses this relation [30]. Later it was suggested that w should be the speckle size [17, 19],

$$w_{\text{speckle}} = \frac{\lambda z}{D}, \quad (5.6)$$

where z is the distance between the object and image planes, and D is the imaging aperture⁴. This expression makes sense physically, because in the time period w_{speckle}/V the speckles have first translated a relevant distance to start decorrelating, which is precisely what the time τ_c describes. Since there are no lenses in our numerical setup, our 'aperture' (D) is the illuminated area, which is our entire cylinder.

5.3.2. RESULTS

We may compare our results with these expressions by first noting that all expressions for K in Eqs. (5.2)-(5.4) depend only on the ratio τ_c/T . Upon substituting Eq. (5.5), we see that the analytical results for K all depend on the quantity w/VT . This is consistent with our independent finding that $d = VT$ is the relevant parameter for studying $K(V)$, as was evidenced by Fig. 5.3. We view this finding as evidence that τ_c does indeed scale inversely with V , cf. Eq. (5.5).

SPECKLE CONTRAST DEPENDENCE ON DECORRELATION TIME

Having written $K(\tau_c/T)$ as $K(w/d)$, Eqs. (5.2)-(5.4) may be used to fit our simulation results with fitting parameters w and β . Fig. 5.4 shows the same data as shown in Figs. 5.2-5.3, but now with the x-axis rescaled to $(\tau_c/T)/w = d^{-1}$. This scale was chosen to resemble the usual τ_c/T scale [17, 20], but deviates because we used w to fit our data with known V . Consequently, τ_c in Eq. (5.5) is not well-defined, as it differs for each fit (by up to a factor two). For the fit of Eq. (5.4) we have used the exact solution of the integral. For the fit of the Lorentzian model $\beta = 1$ is used, because the fit would result in $\beta > 1$, resulting in non-physical $K > 1$ at low velocities. Finally, all three models would

⁴Note that the speckle size is determined fully by the imaging system, and *not* by the scattering system being observed (e.g., inter-particle distance) [20].

have been bad if we had fit them across the whole domain; therefore, only the region of large τ_c/T contributes to the fit.

From the figure, we note that the Lorentzian model describes our results poorly, whereas the other models do an excellent job for large $\tau_c/T \sim d^{-1}$ (low V). This is consistent with the fact that we have flow at a constant velocity, whereas the Lorentzian model is more appropriate for Brownian motion [17]. The Gaussian and constant-velocity models resemble each other more closely, as they are both for ordered motion.

However, β describes the reduction of K due to the finite pixel size, whereas we have infinitesimal pixels. Therefore, we may not use β as a fitting parameter, and actually should just take $\beta = 1$, as is shown in Fig. 5.5. Note that β has a negligible influence at small $\tau_c/T \sim d^{-1}$ (high V), and mostly results in a vertical shift at large d^{-1} (low V). The main difference here is that the analytical models have their asymptote at $K = 1$, whereas our simulations yield a value slightly below one. The reason is that our simulations implement multiscattering, which reduces K . However, in our rather dilute simulations, single scattering still contributes significantly ($\sim 90\%$), resulting in only a slightly lower value for K . The analytical models do not incorporate this effect, and thus β provides a first order approximation to including multiscattering analytically.

Next, it may be seen that the Gaussian model performs slightly better across the whole domain than the constant-velocity model, although our simulations do have a constant velocity. A possible explanation could have been that particles move in and out of the laser's view, which results in a small amount of speckle boiling. However, simulations without cyclic BCs (in which we have purely [translating speckle](#)) have revealed a less than 1% difference in the results; thus speckle boiling is not the cause.

Related to that, all models describe the results at small $\tau_c/T \sim d^{-1}$ (high V) poorly, as K seems to saturate in the simulations, which is why the fits were made for large d^{-1} . However, fitting the models at small d^{-1} instead does not yield a good fit (not shown); therefore, the models cannot describe the simulations in this regime. In an experiment, the effect of static scatterers would be to increase the minimum contrast value [20], which is precisely the effect we observe. However, the simulations do not have any static scatterers. Hypotheses for the difference are effects of single versus multiscattering, and related thereto the diluteness of our flow. More specifically, the theoretical models do not incorporate multiscattering, but its contribution to the simulated intensity is still minor in the present simulations regardless. Therefore, a more likely explanation is the diluteness of our simulations in combination with the major contribution from singly scattered light. The combination causes interferometric fringes to appear on our camera. Although local contrast analysis (i.e., windowing) diminishes their influence, they do have the effect of increasing K and are not affected by the blurring at high velocities (low d^{-1}) [24]. Alternatively, it could also well be that the theoretical models are inadequate in this regime, as they, too, make assumptions on the scattered field's statistics. Future research will need to point out which of the above hypotheses is the case. Nevertheless, our results are meaningful at large d^{-1} , which is the regime that is most difficult to study experimentally due to requiring a camera with a small integration time.

SCALING OF THE DECORRELATION TIME WITH VELOCITY

Finally, it is of prime interest to study the obtained value for the fitted w , as there exists disagreement in the literature. The hypothesised expressions for w in and just above of

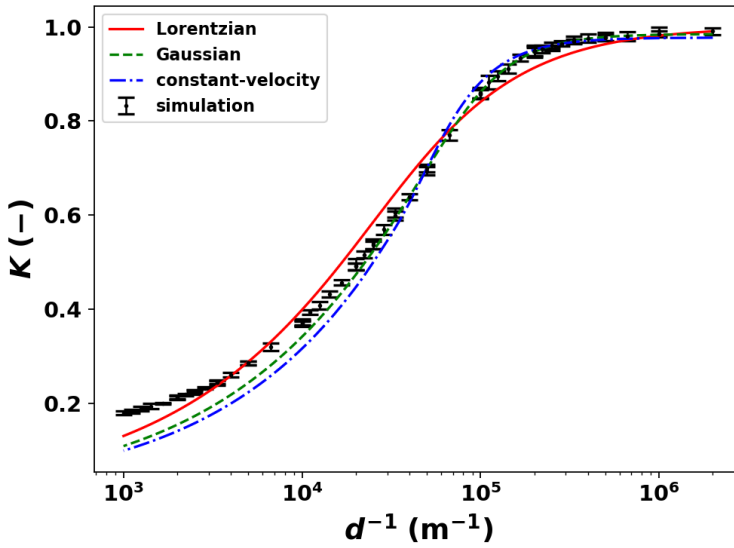


Figure 5.4: Speckle contrast versus $(\tau_c/T)/w = d^{-1}$. The data points are the same as in Fig. 5.3. The values of w and β of models (5.2)-(5.4) are fit (exception: in the Lorentzian model $\beta = 1$ is used), using only the data points with $d^{-1} \geq 3 \cdot 10^4$.

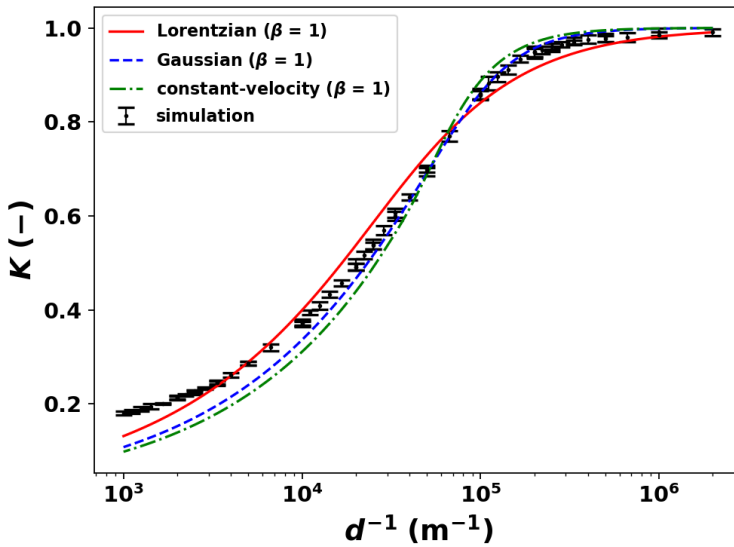


Figure 5.5: Speckle contrast versus $(\tau_c/T)/w = d^{-1}$. The data points are the same as in Fig. 5.3. The value of w of models (5.2)-(5.4) are fit, using only the data points with $d^{-1} \geq 3 \cdot 10^4$, and using $\beta = 1$.

Table 5.1: Used fit parameters of models (5.2)-(5.4).

Model	used in Fig. 5.4		used in Fig. 5.5
	w (μm)	β (-)	w ($\beta = 1$) (μm)
Lorentzian	-	-	17.5 ± 0.2
Gaussian	12.6 ± 0.2	0.970 ± 0.004	11.8 ± 0.1
const. vel.	23.8 ± 0.3	0.955 ± 0.004	21.8 ± 0.2

Eq. (5.6) yield: $w_\lambda = 0.0847 \mu\text{m}$ and $w_{\text{speckle}} = 13.3 \mu\text{m} \times 65.5 \mu\text{m}$. w_{speckle} is given two values, as our aperture⁵ is rectangular with aspect ratio 5, and thus our speckles, too, are rectangular with aspect ratio 1/5. [24] However, in the direction of motion the speckles have width $w_{\text{speckle}} = 13.3 \mu\text{m}$, which is the only relevant length scale for decorrelating speckles due to translational speckle in that direction.

Tab. 5.1 shows the obtained values of w and β from the fits in Figs. 5.4–5.5, with which we can compare w_λ and w_{speckle} . It is clear that w_λ is off by several orders of magnitude, and thus is inadequate. w_{speckle} , on the other hand, is strikingly close to our results, and in particular to the Gaussian, being also the best fit. Thus $w \approx 1.06 w_{\text{speckle}}$ in combination with the Gaussian model best describes our simulation results⁶. Although this does not prove the correctness of Eq. (5.6), for which future research should investigate the influence of λ , z and D , it does make w_{speckle} an extremely likely candidate.

5

5.4. CONCLUSIONS

In summary, we have presented results of our new computer code, which simulates how a plane wave of coherent light scatters off of a collection of moving particles using Mie theory to form a dynamic interferometric speckle pattern (i.e., LSI). By mimicking the finite integration time T of a real camera, we have shown how the speckle contrast K depends on particle velocity V and on T . Existing theoretical models describe how K depends on the speckle decorrelation time τ_c and on T , and it is believed that $\tau_c = w/V$; although the value of w is still disagreed upon in the literature. We provide evidence that τ_c does indeed scale inversely with V , and that $w_{\text{speckle}} = \lambda z/D$ (multiplied by an $O(1)$ constant) is a very likely candidate for w . The Gaussian correlation model does an excellent job at describing our simulation results for large τ_c/T (low V), but deviates considerably for low τ_c/T (high V), for which we provide several hypotheses for future research. However, the Lorentzian model is unsuitable for ordered flow (i.e., advection). Other optical scattering techniques, which use photon correlation, also have the continuing discussion about decomposing flow into advection and Brownian motion [31].

The strength of numerical experiments, once validated, is that *all* circumstances may be simulated and studied. Future research should study the effect of all relevant parameters – and in particular those that are difficult to reach experimentally – which our code can provide. These results will help develop LSI as a quantitative non-invasive measurement technique for velocimetry in **turbid media** (e.g., blood flow⁷).

⁵Our aperture is the illuminated area on the cylinder, as was discussed below Eq. (5.6).

⁶But the scaling factor is bound to depend on many parameters that should still be studied.

⁷Although, patient-specific calibration might always remain necessary [20].

BIBLIOGRAPHY

1. Briers, J. D. & Webster, S. Laser speckle contrast analysis (LASCA): a non-scanning, full-field technique for monitoring capillary blood flow. *Journal of Biomedical Optics* **1**, 174–180 (1996).
2. Boas, D. A. & Dunn, A. K. Laser speckle contrast imaging in biomedical optics. *Journal of Biomedical Optics* **15**, 011109 (2010).
3. Dunn, A. K. Laser speckle contrast imaging of cerebral blood flow. *Annals of Biomedical Engineering* **40**, 367–377 (2012).
4. Stern, M. In vivo evaluation of microcirculation by coherent light scattering. *Nature* **254**, 56 (1975).
5. Draijer, M., Hondebrink, E., van Leeuwen, T. & Steenbergen, W. Review of laser speckle contrast techniques for visualizing tissue perfusion. *Lasers in Medical Science* **24**, 639 (2009).
6. Basak, K., Manjunatha, M. & Dutta, P. K. Review of laser speckle-based analysis in medical imaging. *Medical & Biological Engineering & Computing* **50**, 547–558 (2012).
7. Yoshimura, T. Statistical Properties of Dynamic Speckles. *JOSA A* **3**, 1032–1054 (1986).
8. Asakura, T. & Takai, N. Dynamic laser speckles and their application to velocity measurements of the diffuse object. *Applied Physics* **25**, 179–194 (1981).
9. Fercher, A. F. & Briers, J. D. Flow visualization by means of single-exposure speckle photography. *Optics Communications* **37**, 326–330 (1981).
10. Wang, Y., Lv, W., Chen, X., Lu, J. & Li, P. Improving the sensitivity of velocity measurements in laser speckle contrast imaging using a noise correction method. *Optics Letters* **42**, 4655–4658 (2017).
11. Rosen, J. & Abookasis, D. Noninvasive optical imaging by speckle ensemble. *Optics Letters* **29**, 253–255 (2004).
12. Shinohara, Y. *et al.* Evaluation of Fundus Blood Flow in Normal Individuals and Patients with Internal Carotid Artery Obstruction Using Laser Speckle Flowgraphy. *PloS ONE* **12**, e0169596 (2017).
13. Lambrecht, V. *et al.* Reliability of the quantitative assessment of peripheral blood perfusion by laser speckle contrast analysis in a systemic sclerosis cohort. *Annals of the Rheumatic Diseases* **75**, 1263–1264 (2016).
14. Tuchin, V. *Tissue Optics: Light Scattering Methods and Instruments for Medical Diagnosis* (SPIE press Bellingham, 2007).
15. Qureshi, M. M. *et al.* Quantitative blood flow estimation in vivo by optical speckle image velocimetry. *Optica* **8**, 1092–1101 (Aug. 2021).

16. Nadort, A., Kalkman, K., Van Leeuwen, T. G. & Faber, D. J. Quantitative blood flow velocity imaging using laser speckle flowmetry. *Scientific reports* **6**, 1–10 (2016).
17. Duncan, D. D. & Kirkpatrick, S. J. Can laser speckle flowmetry be made a quantitative tool? *J. Opt. Soc. Am. A* **25**, 2088–2094 (2008).
18. Bandyopadhyay, R., Gittings, A. S., Suh, S. S., Dixon, P. K. & Durian, D. J. Speckle-visibility spectroscopy: A tool to study time-varying dynamics. *Review of Scientific Instruments* **76**, 093110 (2005).
19. Duncan, D. D., Kirkpatrick, S. J. & Gladish, J. C. *What is the proper statistical model for laser speckle flowmetry?* in *Complex Dynamics and Fluctuations in Biomedical Photonics V* **6855** (2008), 685502.
20. Briers, D. *et al.* Laser speckle contrast imaging: theoretical and practical limitations. *Journal of Biomedical Optics* **18**, 066018 (2013).
21. Thompson, O. B. & Andrews, M. K. Tissue perfusion measurements: multiple-exposure laser speckle analysis generates laser Doppler-like spectra. *Journal of Biomedical Optics* **15**, 027015 (2010).
22. Parthasarathy, A. B., Tom, W. J., Gopal, A., Zhang, X. & Dunn, A. K. Robust flow measurement with multi-exposure speckle imaging. *Optics Express* **16**, 1975–1989 (2008).
23. Wang, J. *et al.* Dual-wavelength laser speckle imaging to simultaneously access blood flow, blood volume, and oxygenation using a color CCD camera. *Optics Letters* **38**, 3690–3692 (2013).
24. Van As, K., Boterman, J., Kleijn, C. R., Kenjeres, S. & Bhattacharya, N. Laser speckle imaging of flowing blood: A numerical study. *Physical Review E* **100**, 033317 (2019).
25. Nemati, M., Kenjeres, S., Urbach, H. P. & Bhattacharya, N. Fractality of pulsatile flow in speckle images. *Journal of Applied Physics* **119**, 174902 (2016).
26. Kirkpatrick, S. J., Duncan, D. D. & Wells-Gray, E. M. Detrimental effects of speckle-pixel size matching in laser speckle contrast imaging. *Optics Letters* **33**, 2886–2888 (2008).
27. Goodman, J. W. in *Laser Speckle and Related Phenomena* 9–75 (Springer, 1975).
28. Goodman, J. W. *Statistical Optics* (John Wiley & Sons, New Jersey, 2015).
29. Briers, J. & Fercher, A. *Laser speckle technique for the visualization of retinal blood flow* in *Max Born Centenary Conf* **369** (1983), 22–29.
30. Wang, C. *et al.* Robust quantitative single-exposure laser speckle imaging with true flow speckle contrast in the temporal and spatial domains. *Biomedical optics express* **10**. and references therein, 4097–4114 (2019).
31. Le, V. N. D. & Srinivasan, V. J. Beyond diffuse correlations: deciphering random flow in time-of-flight resolved light dynamics. *Opt. Express* **28**, 11191–11214 (Apr. 2020).

6

TOWARDS DETECTING ATHEROSCLEROSIS

The disease *atherosclerosis* causes *stenosis* inside the patient's arteries, which often eventually turns lethal. Our goal is to detect a stenosis in a non-invasive manner, preferably in an early stage. To that end, we study whether and how *Laser Speckle Contrast Imaging (LSCI)* can be deployed. We start out by using computational fluid dynamics on a patient-specific stenosed *carotid artery* to reveal the flow profile in the region surrounding the stenosis, which compares well with particle image velocimetry experiments. We then use our own fully interferometric dynamic light scattering routines, to simulate the process of *LSCI* of the carotid artery. Our approach offers an advantage over the established Monte Carlo techniques, because they cannot incorporate dynamics. From the simulated *speckle* images, we extract a speckle contrast time series at different sites inside the artery, of which we then compute the frequency spectrum. We observe an increase in speckle boiling in sites where the flow profile is more complex, e.g., containing regions of backflow. In the region surrounding the stenosis the measured speckle contrast is considerably lower due to the higher local velocity, and the frequency signature becomes notably different with prominent higher-order frequency modes that were absent in the other sites. Although future work is still required to make our new approach more quantitative and more applicable in practice, we have provided a first insight into how a stenosis might be detected *in-vivo* using *LSCI*.

This chapter was published previously: Van As, K., Dellevoet, S. F. L. J., Boterman, J., Kleijn, C. R., Bhattacharya, N. & Kenjeres, S. (2022). *Toward detecting atherosclerosis using dynamic laser speckle contrast imaging: A numerical study*. *Journal of Applied Physics*, 131(18), 184902.

6.1. INTRODUCTION

The prevalence of **atherosclerosis** in the human species has been recorded right from pre-agricultural hunter-gatherer populations. The presence of atherosclerotic **plaque (arterial)** inside the **carotid artery**, causes **stenosis**, which increases the risk factor for ischemic stroke or transient ischemic attacks. The common **non-invasive** ways of examining a patient for carotid artery stenosis are **Magnetic Resonance Angiography (MRA)** and computed tomographic angiography [1], which require expensive equipment. Ultrasound techniques, like duplex ultrasonography [1] and photoacoustic imaging [2] may also be used; although being non-invasive, they offer different levels of discomfort to the patient. One optical technique that shows promise in providing an alternate way to screen patients is laser-speckle-based blood flow monitoring.

Speckle is the random **interference** pattern which arises when **coherent light** illuminates diffuse media and meets at the detector plane with varying path-length differences due to different trajectories traversed in the media. The speckle pattern contains useful information about the dynamics of the **scatterers**, because any motion of, or inside, a medium affects the speckle pattern. Speckle correlation is maintained when all scatterers have the same vectorial velocity and thus maintaining all **interparticle distances** (“**translating speckle**”), but decorrelates due to the relative motion of the scatterers (“**speckle boiling**”) [3].

Specifically for blood flow embedded in tissue, each of the layers that the light travels through affect the detected light by the varying transmission, reflection and absorption properties. Furthermore, each patient will be different, e.g., depending upon health, age and ethnicity of the patient. All these different scattering properties yield a static contribution to the measured speckle patterns. However, the temporal dynamics of the underlying flow or the moving scatterers will be imprinted in the temporal evolution of the speckle patterns, which may subsequently be studied [4, 5]. A recent paper has used optical speckle image **velocimetry** to quantitatively reconstruct the velocity profile in blood vessels [6], but their work is still invasive in nature. However, when using speckle patterns no invasive imaging is necessary for the specific case of the carotid artery [7], largely simplifying the required equipment. The latter makes speckle decorrelation a promising candidate as a technique to study the flow of **turbid media** [8–10], such as blood [11]. However, to be able to derive useful information from speckle images, the physical process of light-tissue interaction needs to be studied first.

To that end, many different models have previously been used to study light propagation in tissue, such as simulating a photon random walk using the **Monte Carlo technique** [12–14], approximating the light transport as a diffusive process [15–19], or using the Mie-Percus-Yevick equations to model the scattering from blood [20]. For *in-vivo* blood flow monitoring, there have been numerous studies based on speckle-based techniques, such as **Laser Speckle Contrast Imaging (LSCI)** and complementary techniques like multi-exposure **LSCI** [7, 21]. In applications where direct imaging is possible, such as surface microvasculature, methods based on motion history image (MHI) analysis [22, 23] or laser speckle optical flow imaging (LSOFI) [24] may be used. In principle, one should be able to quantitatively derive properties of the underlying flow from the measured speckle patterns (e.g., the velocity), even in cases where direct imaging is not possible such as deeper embedded vessels (e.g., the carotid artery). One metric that is

affected by the speckle dynamics is the **speckle contrast** K that is simply the ratio of the intensity's standard deviation to its mean. Although it is now widely accepted in literature that K scales inversely with velocity, the exact quantitative relationship still remains elusive [25–28] (see Chap. 5). Consequently, quantitative measurements still rely on combining multiple measurement techniques [6]. Nevertheless, with our goal of detecting atherosclerosis, we may bypass these challenges and use **LSCI** to qualitatively describe features of the underlying (blood) flow.

In our previous work, we had developed a new numerical procedure to simulate how a plane wave of monochromatic coherent light (i.e., a laser) scatters off of an ensemble of particles [29] (see Chap. 2). Our algorithm is based on **Mie theory**, which gives the exact solution to how light scatters off of a sphere, that we have then adapted to include **multiscattering**. Although simplifications were made to make this approach computationally feasible, the advantage of our new approach is that we carefully track the **phases**. Consequently, we can simulate instantaneous speckle images containing all the **interferometric** information an experimental speckle pattern would also contain, allowing us to simulate the temporal dynamics, whereas the popular Monte Carlo approach yields statistical averages [12]. Using our new code, we had performed simulations using a sinusoidal- and a real heartbeat-modulated flow on both plug flow and Poiseuille flow in a cylinder (see Chap. 4). From the results, we have first shown that we could reconstruct the original heartbeat frequency from the dynamic speckle patterns. Then we proceeded to show the effect of speckle boiling on the **frequency spectrum** of the speckles: speckle boiling caused by particles entering and leaving the laser beam and speckle boiling caused by the flow profile (i.e., Poiseuille flow) both have the effect of adding **white noise**¹ to the frequency spectra. When both origins of speckle boiling were present, their individual white noise effects added cumulatively. This is the primary advantage of performing simulations: we were able to simulate precise conditions that are unattainable in experiments, which allowed us to study the physics of speckle boiling in detail. The speckle boiling did not interfere with our ability to extract the original heartbeat frequency from the dynamic speckle, as we had obtained a **signal-to-noise ratio** of about 50.

In this work we proceed to apply our computer model to the geometry of a carotid artery of a patient who suffers from atherosclerosis, i.e., there is a stenosis in the **internal carotid artery (ICA)**. To that end, we have first coupled our light scattering code to an existing **Computational Fluid Dynamics (CFD)** code: OpenFOAM [30]. We then simulated the flow inside the artery, and have compared our results to simulations performed in Ansys Fluent [31–33] and experimental results based on **Particle Image Velocimetry (PIV)** [32, 34]. Finally, we simulated the light scattering in five different regions in the artery and we use **LSCI** and spectral analysis to study how we can detect a stenosis.

6.2. GENERIC APPROACH

The goal is to study **atherosclerosis** using **LSCI**. In **LSCI**, an object is illuminated by a laser (i.e., a **plane wave** of **coherent monochromatic** light), as is illustrated in Fig. 6.1a. The light scatters off of all particles it encounters, and the scattered light is measured with

¹That is, it is frequency-independent noise that may be filtered using Fourier analysis and a threshold filter.

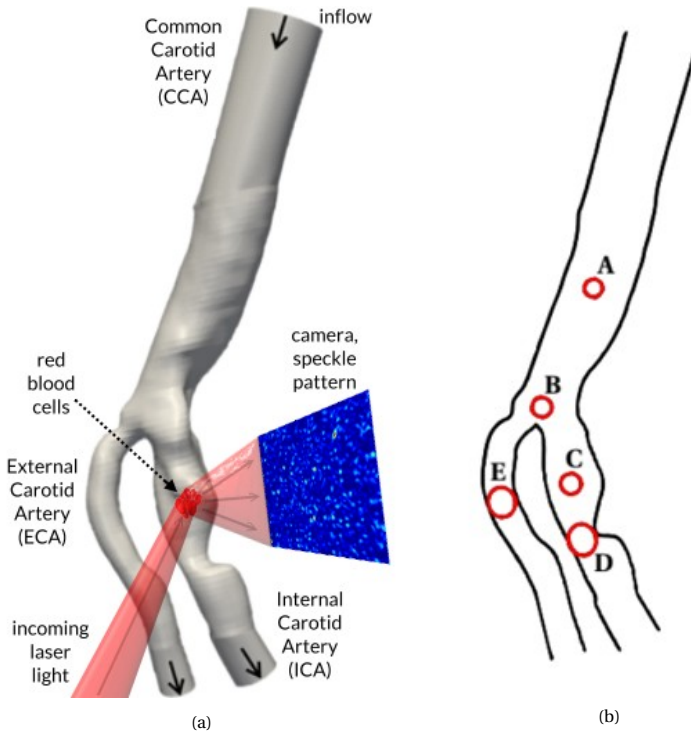


Figure 6.1: (a) Sketch of the laser speckle imaging process. Laser light hits an artery locally, scatters off of the flowing red blood cells, and forms a dynamic speckle pattern at a camera. The artery is a 3D model of a stenosed carotid artery. (b) The chosen sites on which we perform our numerical LSCI experiments.

a camera. Due to the interference of the scattered light with itself, a dynamic random interference pattern is formed as a result: a dynamic **speckle pattern**. Information about the underlying flow system is contained in the dynamics of the speckle pattern.

We model this setup numerically, such that we can perform numerical experiments. We use a CT-scanned 3D model of an atherosclerosis patient's carotid artery [35] as our geometry (see Fig. 6.1a). We use a CFD code to simulate the motion of tiny particles that represent red blood cells. A separate optics code simulates how the laser's light scatters off of these dynamic particles, and mimics the measurement of a camera that has been placed at a right angle relative to the incoming light. Details of these two codes are discussed in Secs. 6.3 and 6.5.

We perform numerical experiments on the artery at five different locations. These five sites are shaped cylindrically (i.e., the shape of the illuminated volume of a laser beam shining through), and they are at the following locations (see Fig. 6.1b): nearby the inlet (A), right before the **bifurcation** (B), right before the sclerosed region in the ICA (C), inside the **sclerosed** region (D), and opposite of site C in the ECA (E). The red circles in the figure show the location of the sites, as well as the size of the laser spot used. Details of this process are discussed in Sec. 6.4.

6.3. COMPUTATIONAL FLUID DYNAMICS (CFD)

6.3.1. APPROACH

The fluid flow inside the artery is computed using a CFD code. For our simulations, we have used the open source software [OpenFOAM v2.4](#), and we validate our results to simulations performed in the proprietary CFD code [Ansys Fluent \[31–33\]](#) and experimental stereoscopic [PIV](#) results [32, 34]. The arterial geometry is discretized using a tetrahedral mesh of 3.5 million cells. In these cells, the [incompressible Navier-Stokes equations](#) are solved for the velocity and pressure fields using the finite volume method. These equations are combined using OpenFOAM's implementation of the PIMPLE algorithm with an iterative predictor-corrector method [36]. The convective terms are discretized using a second-order accurate linear upwind differencing scheme (LUDS), while the other spatial terms use a second-order accurate central differencing scheme (CDS). For the temporal discretization, the first-order Euler forward method is used with timestep $\Delta t = 0.067$ s.

Many small (radius 4 μm) spherical particles are injected in the inlet to represent red blood cells. They are injected at a rate of 10^4 particles per second. Their motion in the computed fluid flow is calculated using [LPT](#) (see Sec. 1.4), in which we consider the small particles as perfect tracer spheres that do not affect the underlying flow. All physical parameters used in our CFD simulations are listed in Tab. 6.1.

At the two outlets we impose a fixed flow rate boundary condition for the velocity field, in which the flow rate at the two outlets is enforced to have the same ratio (60:40) as the outlet areas. At the arterial wall we impose a no-slip condition for the velocity and a zero normal gradient for the pressure. At the inlet of the common carotid artery we impose a time-dependent flow rate $Q(t)$, such that the velocity u at the inlet is:

$$\vec{u}(\vec{r}, t)|_{\text{inlet}} = -\frac{Q(t)}{A|_{\text{inlet}}} \nu(\vec{r}) \hat{n}|_{\text{inlet}}, \quad (6.1)$$

where $A|_{\text{inlet}}$ is the surface area of the inlet and \hat{n} is the unit vector pointing outwards orthogonal to the surface area. At the inlet, we use the exact solution for flow inside an infinite cylinder (i.e., [Poiseuille flow](#)), $\nu(\vec{r}) = c(1 - r^2/R^2)$, which is a parabolic profile. R is the mean radius of the nearly-circular inlet, and the normalization constant c is chosen such that $\nu(\vec{r})$ integrates to unity over the inlet's surface area.

Table 6.1: Summary of the parameters relevant to CFD.

Kinematic viscosity fluid	$\nu = 8.28 \cdot 10^{-6} \text{ m}^2/\text{s}$
Density fluid	$\rho = 1157.2 \text{ kg} \cdot \text{m}^{-3}$
Mean radius arterial inlet	$R _{\text{inlet}} = 9 \text{ mm}$
Frontal area arterial inlet	$A _{\text{inlet}} = 2.63 \text{ cm}^2$
Reynolds number at inlet	$\text{Re} _{\text{inlet}} = 2\bar{u}R/\nu = 331.1$
Flow period	$T = 1.34 \text{ s}$
Womersley number at inlet	$\alpha _{\text{inlet}} = 6.77$
Particle radius	$a = 4.00 \text{ }\mu\text{m}$

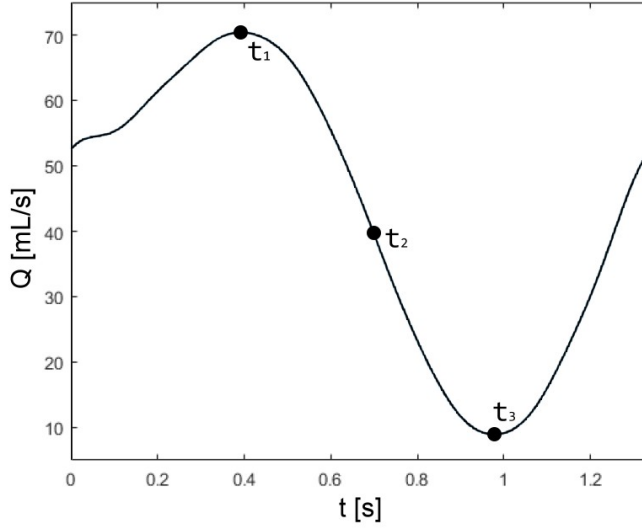


Figure 6.2: The imposed flow rate at the arterial inlet, representing a simplified heart-beat signal. In this paper, we present flow results at the three labeled times, being at the maximum (t_1), the average (t_2) and the minimum (t_3) input flow rate.

The input signal, $Q(t)$, and the extraction times² that we have used, is shown in Fig. 6.2. The signal is the same as the one used in the experiments that we compare our results in this section with. By the experimental limitations of the pump, the signal is not an exact heartbeat signal, but it does have the same distinct features such as a major oscillation followed by a minor oscillation.

Initially, we start with a zero velocity inside the entire artery. Several flow periods are needed for the entire flow to adapt to the inflow before a temporal equilibrium is reached, which takes a time of the order of the [flow-through time](#) for incompressible flow. To be on the safe side, we first simulate the flow for 10 periods before we start gathering any data for our simulations.

Although real blood behaves as a [non-Newtonian fluid](#) due to the large particle density and the corresponding particle interactions, we use an incompressible Newtonian model to better match the experimental situation [35]. These experiments use [PIV](#) to obtain the velocity field inside the arterial geometry. The experimental artery was created by 3D-printing the arterial model, followed by casting a plastic phantom out of it. The scale compared to a real artery is approximately 21:10. The fluid was an aqueous glycerol solution seeded with hollow [refractive-index-matched](#) glass particles, varying in size between 2 and 20 μm diameter.

²The precise extraction time of the OpenFOAM simulation data differs slightly from Fluent and PIV due to OpenFOAM's dynamic timestepping, but this difference is insignificant for the comparison of the flow profiles.

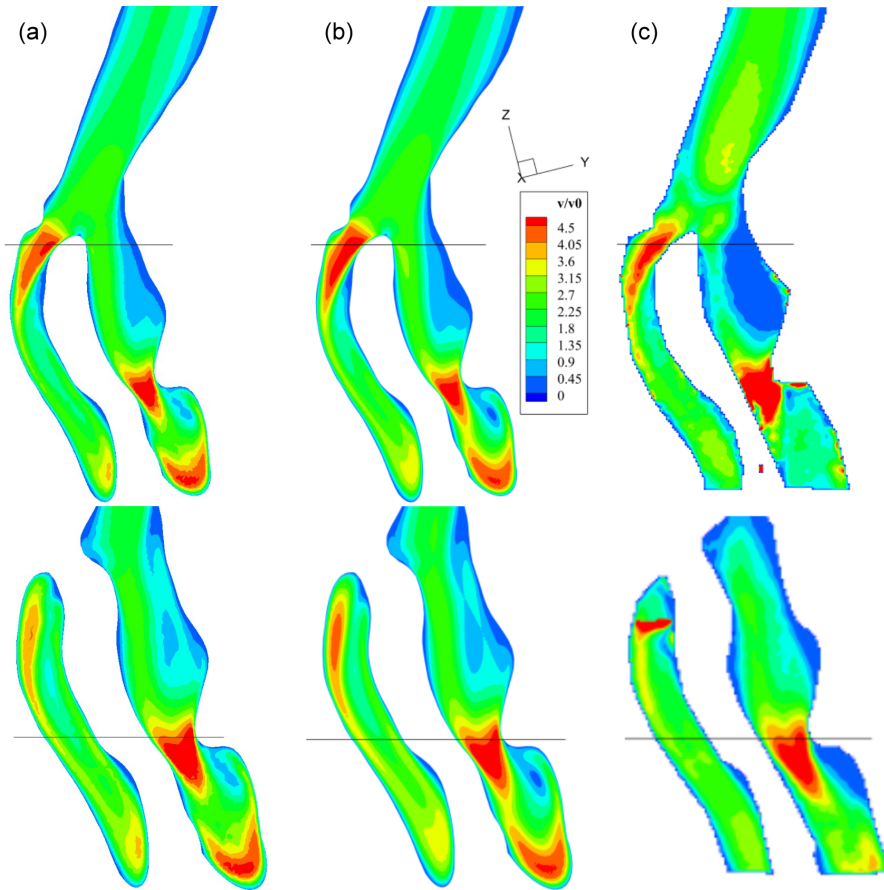


Figure 6.3: Normalised flow profiles of the planar velocity V/V_0 at two different slices at maximum inlet velocity ($t = t_1$ in Fig. 6.2). Comparison between OpenFOAM simulations (a), Fluent simulations (b) and PIV experiments (c).

6.3.2. RESULTS

The simulated flow profile at time $t = t_1$ (when the inlet velocity is maximum) is shown in Fig. 6.3a for two different slices³. The colour scale indicates the velocity relative to the inlet velocity. There is a small **stagnation point** right above the bifurcation. The narrowing of the **ECA** results locally in a twice as high velocity. The same is true for the narrow stenosis in the **ICA**. Right before the stenosis is a region in which the velocity is lower, and in which a local **circulation** forms, which is a characteristic flow pattern for detecting a stenosis.

³The top slice has origin (0.201, 0.1453, 0.3902) and normal vector (100, -0.5415, 0.3794). The bottom slice has origin (0.2054, 0.1389, 0.3455) and normal vector (-100, 1.3, -0.119). Note that these slices are basically just YZ-planes, but rotated ever so slightly to better correspond with the experimental orientation of the artery. TecPlot360X-2017 was used to extract the slices and plot the contours.

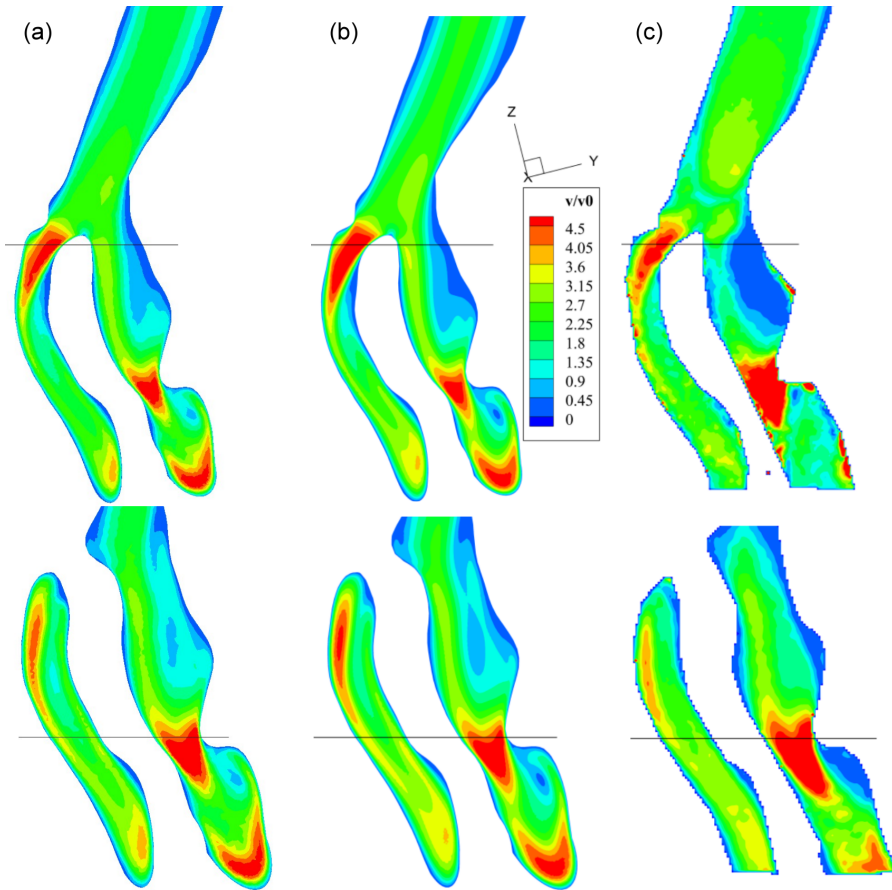


Figure 6.4: Normalised flow profiles of the planar velocity V/V_0 at two different slices at average inlet velocity ($t = t_2$ in Fig. 6.2). Comparison between OpenFOAM simulations (a), Fluent simulations (b) and PIV experiments (c).

At an average inlet velocity, such as is shown in Fig. 6.4a, not much changes. The velocity relative to the inlet velocity is everywhere very similar. At the left side of the ICA, a streak starts to form, which becomes much more prominent at the lowest inlet velocity in Fig. 6.5a. We presume that this is caused by the inertial forces of the preceding circulation (i.e., the circular flow in the region right before the stenosis). That is, as the inlet velocity (V_0) decreases, the velocity (V) decreases everywhere, but the ratio V/V_0 does not decrease as fast directly adjacent to the circulation.

A comparison with Ansys Fluent simulations and PIV measurements is shown in (b) and (c) of Figs. 6.3-6.5. Both simulations show the same flow features, both qualitatively and quantitatively. Although the resolution of the PIV measurements is less than that of the simulations, we can still see the same distinct flow features and a mostly quantitatively matching velocity. Fig. 6.6 shows a more quantitative comparison along one

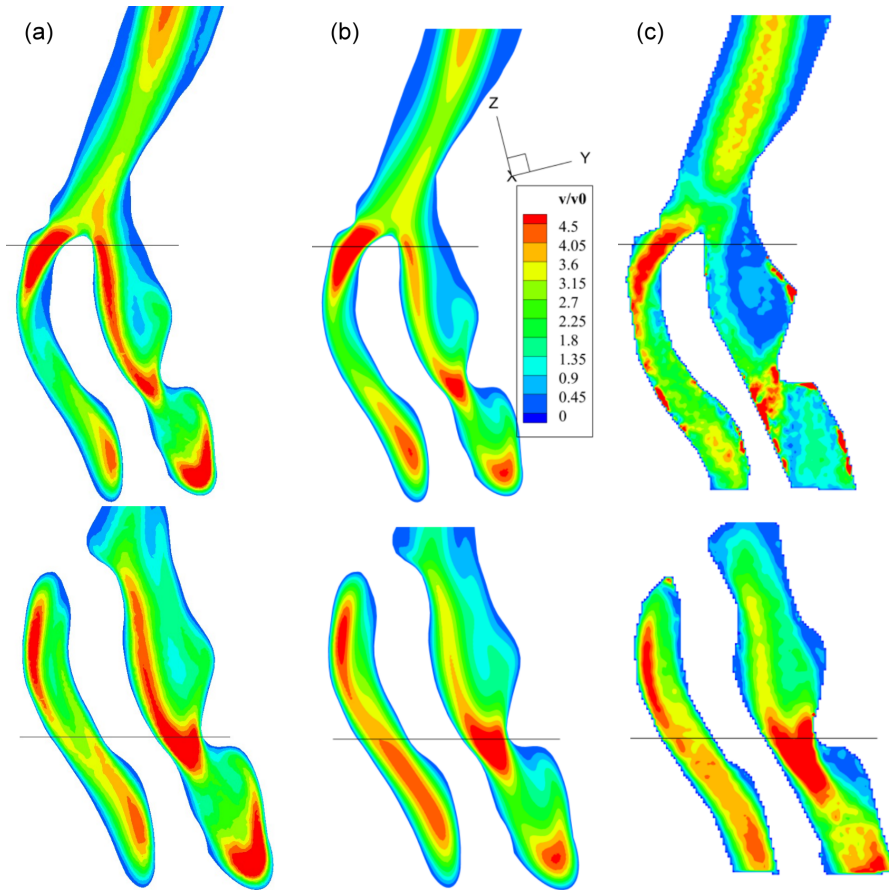


Figure 6.5: Normalised flow profiles of the planar velocity V/V_0 at two different slices at minimum inlet velocity ($t = t_3$ in Fig. 6.2). Comparison between OpenFOAM simulations (a), Fluent simulations (b) and PIV experiments (c).

cross-sectional line⁴, just after the bifurcation. In those figures, y^* is the zero-centered spatial coordinate along the line, normalised by the mean diameter of the arterial inlet. When comparing the **ECA** (i.e., $y^* < 0$ in Fig. 6.6), both simulations compare reasonably well with the **PIV** experiments; Fluent seems to perform better at a higher velocity ($t = t_1$), whereas OpenFOAM does so at lower velocities ($t = t_3$). In the **ICA** ($y^* > 0$), the **PIV** measurements deviate considerably. More specifically, the planar velocity inside the circulation is lower in the **PIV** measurements and/or its circulation region is larger. Since a circulation is rather sensitive to the local geometry, this may well be explained by manufacturing imperfections of the mold used by the **PIV** experiments. Nevertheless, we expect that our fluid simulations are adequate for our **LSI** conclusions in Sec. 6.5.

⁴The cross-sectional line is the intersection of the top slice (see the previous footnote) with the plane with origin (0.2007, 0.1407, 0.3690) and normal vector (0, -21.45, -97.67).

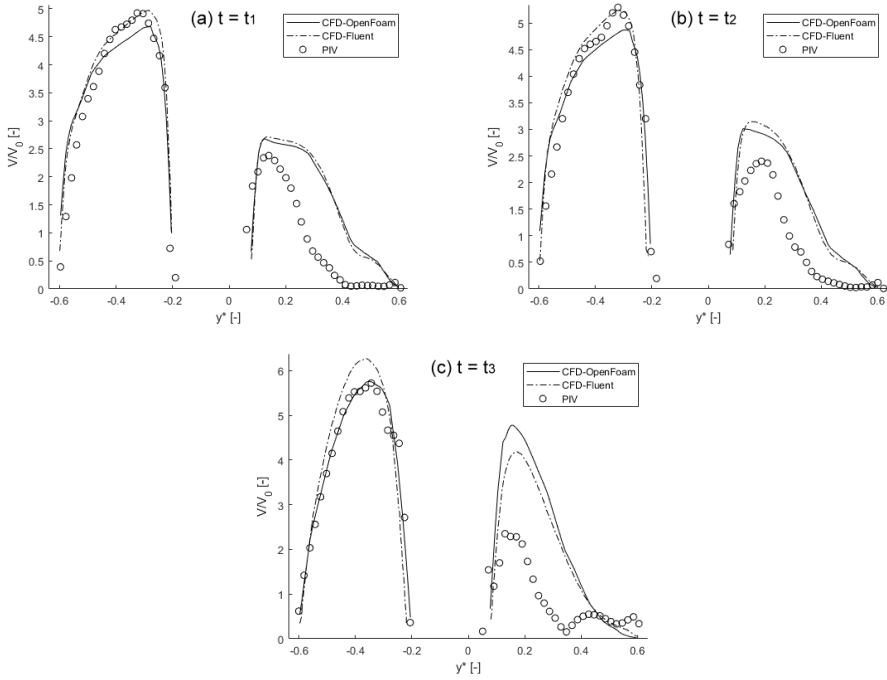


Figure 6.6: Velocity profile along the cross-sectional line shown in the top figures of Figs. 6.3-6.5. y^* is the zero-centered spatial coordinate along the line, normalised by the mean diameter of the arterial inlet. The profiles are shown at maximum inlet velocity (a), at average inlet velocity (b) and at minimum inlet velocity (c).

6.4. COUPLING FLUIDS TO OPTICS

To study **LSCI**, we need to simulate how coherent light scatters off of the particles of which we calculated the motion in the previous section. This task will be performed by a separate optics code, which will be discussed in the next section. The advantage of using two separate codes, is that they are mutually independent: the optics code can use a set of particle positions as its input data, originating from any source – from any **CFD** simulation or experiment. However, the two codes will need to be coupled.

To that end, we extract the particle positions from our **CFD** simulations in the sites discussed in Sec. 6.2. These sites are cylindrically shaped, to mimic a laser beam illuminating a subset of the total number of particles. The laser spot size was chosen such that there are on average approximately 100 particles within the illuminated volume. In that manner, a similar scattered light intensity may be expected on the camera for each numerical experiment. The extracted particle positions are then converted to the input format required by the optics code.

Only the particles that are directly inside the illuminated volume are extracted, and thus only they contribute to the **(multiply) scattered light** in our simulations. This only includes the small dynamic particles that were injected into the flow. In practice one

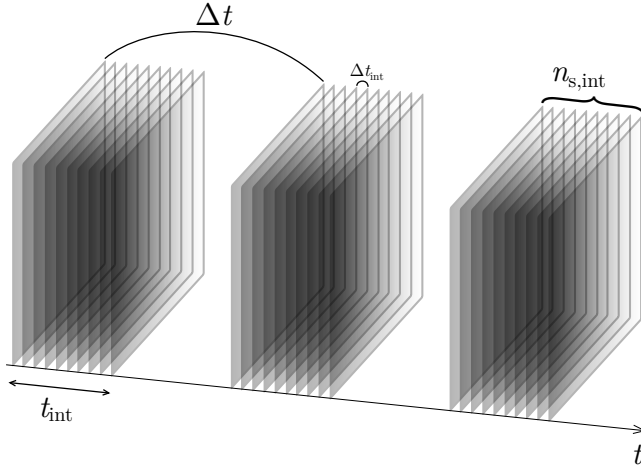


Figure 6.7: To mimic the integration time of a camera, we sample instantaneous data at a short interval Δt_{int} . This process is repeated at distant intervals (Δt apart) to obtain temporal data. (Figure reprinted from our previous paper [29].)

may expect a contribution by static scatterers inside the arterial wall and inside the tissue around it as well. When this will be incorporated in the future, one may expect the speckle dynamics to become more complex, manifesting in having additional [frequency modes](#) in the [Fourier spectra](#) [37].

To study *dynamic* speckle imaging numerically, we deploy a trick. Each execution of the optics code is instantaneous, meaning we take the scatterers to be static while the light [diffracts](#) (i.e., the speed of light is “infinite” compared to that of the blood flow). To mimic the finite integration time t_{int} of a camera, which is a relevant parameter in dynamic [LSCI](#) [25, 26], we perform $n_{s,\text{int}}$ of such scattering simulations in very rapid succession [29]. This process is illustrated in Fig. 6.7. Finally, all simulated intensities are summed to obtain one single (blurred) speckle image. We call this process [microstepping](#). This process is then repeated a short while (Δt) later repetitively at the data sampling rate, $f_s = 1/\Delta t$, in order to obtain temporal data. All settings (as are summarised in Tab. 6.2) were chosen based on our previous results: the speckle contrast (see Eq. (6.2)) is sensitive to changes in scatterer velocity at our chosen [camera integration time](#) [28], and the number of integration samples is a compromise between computational time and an $\sim 1\%$ numerical integration error [29]. Altogether, 400 scattering simulations are performed for each flow period.

However, to perform the microstepping we must first acquire the particle positions at each of the short Δt_{int} intervals, required by the optics code. The timestep in the [CFD](#) simulations was chosen such that the flow data is available at precisely the required rate (f_s). Then, for each time (Δt apart), the [CFD](#) simulation is restarted to simulate mere microseconds of flow progression with a timestep $\Delta t_{\text{int}} = 2.5 \mu\text{s}$ for a time period of t_{int} . Finally, all particle positions are extracted, and the optics code is executed repetitively.

6.5. SPECKLE IMAGING

6.5.1. APPROACH: OPTICS CODE DESCRIPTION

Our in-house optics code, which has been previously described in detail in Sec. 2.1 [29], is fully interferometric, includes **multiscattering**, and is based on Mie theory. Mie theory describes the **scattering** of a **monochromatic plane wave** by a single homogeneous spherical particle [38–41]. Using a far-field assumption, the scattered wave of each scatterer behaves locally in a distant region as a plane wave again. This is valid in a sufficiently dilute system, or in a system containing sufficiently small particles [29]. Although this assumption is not satisfied for true blood flow, it does enable us to incorporate multiple scattering, which otherwise would have been computationally infeasible due to its $O(N^3)$ **numerical complexity**, where N is the number of particles in the illuminated volume. During multiple scattering each particle iteratively scatters to each other particle, including **backscattering**, until successive **scattering orders** contribute negligibly to the final result. Finally, all scattered light is added interferometrically at a two-dimensional grid of infinitesimal points (i.e., at our “camera”), and the intensity is computed by squaring the electromagnetic field. Note that no imaging system (such as lenses) is being simulated, as that is unnecessary to numerically obtain (dynamic) speckle images.

The assumptions made, allow us to simulate dynamic laser speckle within a reasonable amount of time, while incorporating as much of the physics as possible. There exist alternative methods to our Mie calculation routine, such as the **T-matrix method** [42] which yield an exact result to the multiple scattering problem. However, since our dynamic simulations require $\mathcal{O}(10^4)$ instantaneous simulations, this is presently not practical with the available computational resources. Much more details about our code and its validity were presented in all previous chapters. The optics simulation parameters of the current work are summarised in Tab. 6.3.

6.5.2. APPROACH: POST-PROCESSING SPECKLE

An example of an instantaneous (simulated) **speckle image** is shown inside Fig. 6.1a. Within such speckle images, information about the underlying scatterers is contained. One metric for quantifying that information is the **speckle contrast** [27, 43]:

$$K = \frac{\sigma_I}{\langle I \rangle}, \quad (6.2)$$

where I is the intensity, σ_I denotes its (spatial) standard deviation, and $\langle I \rangle$ is the mean (spatial) intensity. For fully developed (instantaneous) speckle, the speckle contrast is

Table 6.2: Summary of the simulation parameters relevant to data acquisition.

Total simulation time	35 periods
Data sampling rate - corresponding frame rate (FPS)	$f_s = 20$ samples/period ≈ 26.8 Hz
Camera integration/exposure time	$\Delta t_{\text{int}} = 50 \mu\text{s}$
No. integration samples	$n_{\text{s,int}} = 25$
Velocity of extracted particles	range: 0 - 1.2 m/s

theoretically precisely [44] $K = 1$. However, when light **depolarizes** due to multiple scattering such as is the case in tissue, K will become less than one [45].

However, as the scatterers move, we do not obtain instantaneous speckle, but rather slightly blurred speckle patterns due to the finite **integration time of the camera** (see Sec. 6.4). The blurring causes σ_I to decrease, while not affecting $\langle I \rangle$, yielding a speckle contrast value $K < 1$. The amount of blurring is directly correlated with the velocity of the scatterers; thus introducing a dependency of K on the velocity of the underlying flow system, which makes K a useful metric for studying a flow system using dynamic speckle imaging.

Unfortunately, a truly quantitative relation between K and the velocity remains elusive [25, 46]. In ideal situations, the model that assumes Gaussian statistics for the **auto-covariance** of the temporal speckle fluctuations seems to perform well [25, 28]. However, in realistic situations K is affected by disturbances, such as the **speckle boiling** caused by the scatterers entering/leaving the imaging plane (i.e., out-of-plane motion) and entering/leaving the illuminated volume. The speckle contrast is also bound to a minimum value due to the influence of static scatterers [26], and the influence of multiple scattering. Therefore, any quantitative measurement with laser speckle contrast imaging currently requires calibration [26]. Fortunately, K is still very useful for relative measurements: i.e., we might not know the precise velocity, but we can observe changes and differences, which gives us information about the underlying flow.

To that end, we should first obtain accurate values of K . Due to the existence of large-scale interferometric **fringes**, we cannot simply compute K over the entire image, as those fringes arbitrarily increase σ_I and therefore K . These fringes are the consequence of our rather dilute simulations [29], but the following has been reported to be relevant for experiments just as well [47]. The solution is to use *local* speckle contrast analysis (LSCA), in which the image is first subdivided in a total of $N_x \times N_y$ tiny square **windows**, then $K_{i,j}$ is computed in each subdivision, and finally K is simply the average of all $K_{i,j}$:

$$K = \frac{1}{N_x N_y} \sum_{i=0}^{N_y-1} \sum_{j=0}^{N_x-1} K_{i,j}. \quad (6.3)$$

We had found previously that for our simulated 128×128 pixels camera [see Tab. 6.3], windows of about 8×8 pixels each yielded the best results for our simulations, with a maximum **convergence** error of $\sim 2.6\%$ [29].

Table 6.3: Summary of the optics parameters.

Refractive index	$n_{\text{sphere}} = 1.52$ $n_{\text{medium}} = 1$
Wavelength	$\lambda = 532 \text{ nm}$
Particle radius	$a = 4.00 \text{ }\mu\text{m}$
No. of pixels (camera)	$M = 128 \times 128$
Physical size of the camera “chip”	$1.5 \text{ mm} \times 1.5 \text{ mm}$
Distance artery \leftrightarrow camera	25 cm

Finally, we study *dynamic* speckle patterns, meaning we can compute K at our data sampling rate f_s [see Tab. 6.2]. The result is a time series $K(t)$ which contains information about the flow dynamics. Since we study flow in the carotid artery, it is prevalent that the periodicity of the heartbeat should reflect in the $K(t)$ signal as well. Therefore, it is also useful to calculate the **frequency spectrum** of $K(t)$ using the FFT; however, it should be noted that the frequency spectrum of $K(t)$ will not equal the frequency spectrum of the underlying velocity, since $K(t)$ does not scale linearly with velocity [25, 28]. Rather, the frequency spectrum of $K(t)$ will have roughly the same major (i.e., first-order and second-order) **frequency modes** as the frequency spectrum of the velocity, but it will have additional higher-order frequency modes due to the non-linearity of the relationship [29].

6.5.3. RESULTS

The **speckle contrast** K was computed in each of the five sites (see Sec. 6.4) over the course of 35 flow periods (see Tab. 6.2). The resulting **frequency spectra** are shown in Figs. 6.8 for each site, with the original speckle contrast time series shown in the inset of each figure. For quick reference, the input signal (**flow rate** Q versus time t) is shown in the Fig. 6.8a, together with an inset showing the location of each of the five sites.

Site A (see Fig. 6.8b) is just a little **downstream** of the inlet. In this region, the flow is still behaving nicely as there are no physical obstructions. Therefore, you would expect a rather clean signal that closely represents the inflow function, $Q(t)$.

However, speckle contrast K does not scale linearly with velocity v and thus not linearly with flow rate Q either. Rather, a low K corresponds with a low standard deviation of the intensity pattern σ_I , which implies that over the course of the **camera integration time** Δt_{int} much blurring occurs. In turn, this implies a high velocity v ; therefore, a high v corresponds to a low K . Consequently, the time series (shown in the insets) paint an upside-down image of the local mean velocity.

When a Gaussian autocovariance of the temporal fluctuations is assumed, an equation for the relation between K and the speckle decorrelation time τ_c may be derived [25] that compares reasonably well with our previous simulations in Chap. 5 [28]. However, there is no agreement in literature how to convert τ_c into velocity v , making the exact relationship elusive [25, 46]. Regardless, we have found in Chap. 4 from simulating a sine input signal (which is just a single peak in the frequency spectrum) that the frequency spectrum of the speckle contrast time series has higher-order peaks at multiples of the dominant frequency [29]. These higher-order frequencies are caused by the non-linear relationship between K and velocity v that manifests in the broadening of the troughs and narrowing of the crests of $K(t)$ relative to the input signal. Consequently, it is not useful to directly compare the frequency spectra of K to the frequency spectrum of the input signal⁵. Instead, we will compare all sites with site A, as site A is located just a little downstream of the inlet, where the flow is not yet disturbed.

In the frequency spectrum of site A (see Fig. 6.8b), the dominant frequency peak is at 0.75 Hz, which corresponds to the flow period (see Tab. 6.1). There are also higher-order frequency peaks at multiples of the main frequency, partly due to the complex input signal and partly due to the non-linear relationship between K and velocity v . There is an

⁵For this reason we omit showing the input's frequency spectrum to prevent confusion.

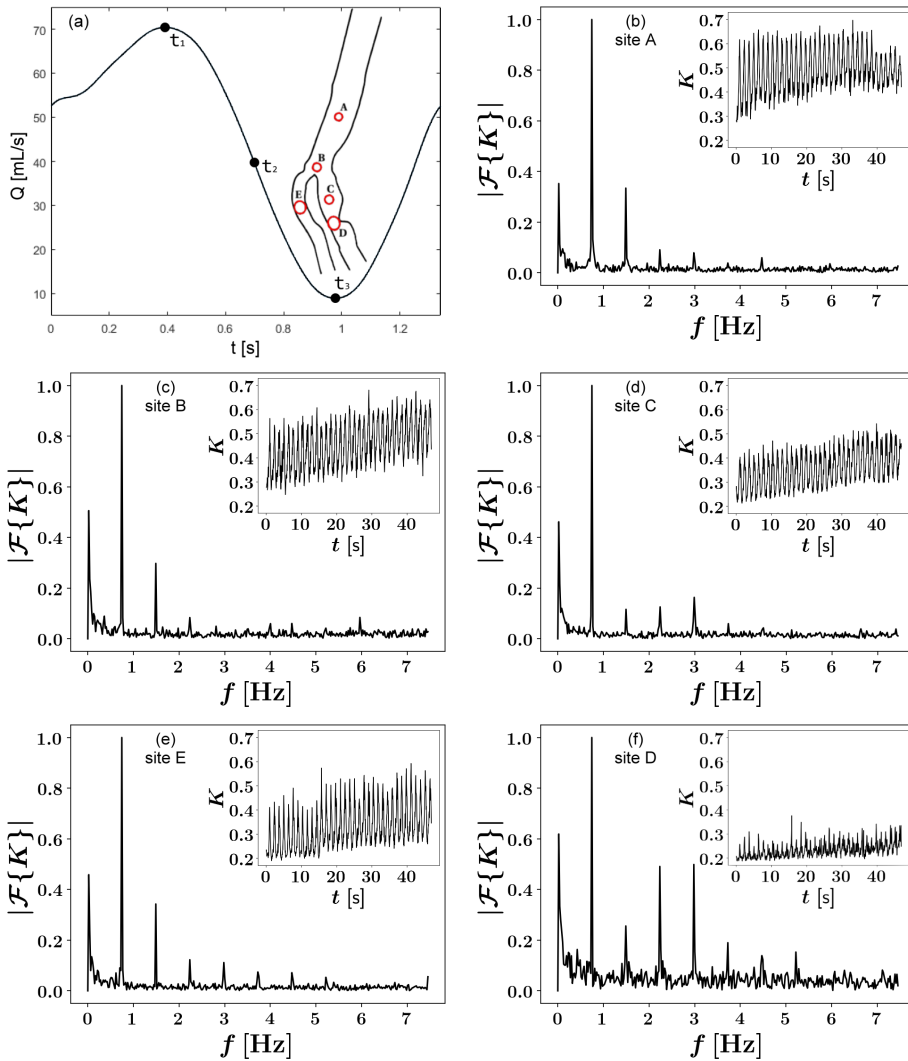


Figure 6.8: Speckle contrast time series (inset) and its frequency spectrum (main figure) for each of the five sites. In (a), the (0.75 Hz) input signal of Fig. 6.2 and the location of the five sites in its inset from Fig. 6.1b is reproduced for quick reference. In (b)-(f), the five frequency spectra are ordered according to their location in the artery.

additional peak at the near-zero frequency, which is also present for all other sites. This is merely a simulation artefact in OpenFOAM caused by particles getting stuck inside the walls (thereby slowly increasing the number of particles inside the illuminated volume), and should thus be ignored when studying the dynamic evolution of speckle. Finally, between all peaks there is noise that is not present in the input signal. In Chap. 4 [29], we have proven that this noise is fully caused by **speckle boiling** due to the relative motion between the particles (i.e., the flow profile inside an artery is more like **Poiseuille flow** than **plug flow**), and particles entering and leaving the illuminated volume. In the present work, there is an additional third cause of speckle boiling, being out-of-plane motion of particles.

Site B (see Fig. 6.8c) is located at the **bifurcation** of the artery. In this region one would expect additional speckle boiling as there is more relative motion between the particles: some go left, and some go right. Relative to site A, this manifests as more noise that is mostly visible at the higher frequencies. In site B there is also a larger particle buildup than in any other site due to the bifurcation (and the earlier-mentioned simulation artefact), but the sole effect is a larger peak at the near-zero frequency. In general, the signature of site B's frequency spectrum is very similar to that of site A: the ratio between the first-, second- and third-order peaks is very close. The only indication that the flow at site B is different (i.e., it is a bifurcation) is the increased amount of noise due to speckle boiling.

Site E (see Fig. 6.8e) is in the **ECA**. From the fluid dynamics results, it can be seen that the flow in this region is fairly normal: there is a Poiseuille-like flow profile without **vortices** and **backflow**. As a consequence, the signature of site E's frequency spectrum is very similar to that of site A as well: the main frequency mode is well-represented, and the higher-order frequency modes have the same relative peak height. Relative to site A, the velocity is higher at site E, which also nicely follows from the optics since a lower mean K is measured in site E. Therefore, the speckle measurement can detect the increased velocity and the normal flow profile in site E.

Site C (see Fig. 6.8d) is the equivalent of site E, but in the **ICA**. The mean velocity in site C is similar to that in site E (see Figs. 6.3-6.5), which results in similar values for K . Like in site E, the main frequency mode is also well-represented. However, there are clear differences in the frequency signatures. The higher-order frequency modes are suppressed in site C, because its $K(t)$ does not have the expected broad **troughs** and narrow **crests** as much as the $K(t)$ of site E does have. This implies less extreme temporal velocity fluctuations in site C. From Figs. 6.3-6.5 it can be seen that there is a **circulation** region (with backflow) in site C. The circulating flow's inertia acts as a buffer when the inflow velocity decreases, thus smoothing the crests of $K(t)$. Finally, the amount of noise (caused by speckle boiling) is similar in sites C, A and E, which indicates a flow profile that behaves 'nicely'. Therefore, the same amount of noise in combination with the suppression of the second-order frequency mode might be characteristic for flow regions containing vortices/backflow.

Finally, site D (see Fig. 6.8f) is located inside the **stenosis**. Firstly, the measured values of $K(t)$ are considerably lower than those in the other sites, which makes sense, because the center velocity in this region is roughly 4.5 times greater than the mean inflow velocity (see Figs. 6.3-6.5), which is roughly double the center velocity of the other sites.

Secondly, the main frequency mode is still prominently visible, but the [signal-to-noise ratio](#) went down considerably. This is caused by the measured K being rather low, in which the sensitivity to changes in velocity v is low [25, 28]. A better measurement may be performed by using a lower camera integration time Δt_{int} ; however, we did not want to do that as we were interested in seeing what a (medical) device would measure when it would ‘scan’ the artery without changing the device parameters. Thirdly, the [frequency signature](#) is considerably different than in all other sites. As for the preceding site C, the second-order frequency mode is suppressed. Unique to site D is that the higher-order frequency modes actually became much more prominent, at least relative to the main frequency mode, as has also been found previously in experimental work [35]. Presumably, this is a downstream effect of the preceding unsteady flow region, which introduces flow features with a higher frequency as the unsteadiness causes the flow to no longer follow the input signal precisely. Therefore, characteristic for the stenosis are a lower K , more noise, a slightly suppressed second-order frequency mode, and more prominent higher-order frequency modes (relative to the main frequency mode).

6.6. SUMMARY AND CONCLUSIONS

In this work we set out to study [atherosclerosis](#) using dynamic [Laser Speckle Contrast Imaging \(LSCI\)](#), which should eventually result in the development of new medical measurement devices. To that end, we have developed a fully-modular numerical routine to simulate dynamic [LSCI](#) of any flow system, comprising a separate fluid dynamics and a separate optics code that are subsequently coupled. The fluid dynamics code⁶ simulates the flow and injected particles in an arbitrary geometry. The optics code is based on Mie theory and uses the particle positions as its input to simulate how a coherent plane wave (i.e., a laser beam) scatters off of the ensemble of particles, including multiple scattering. The finite camera integration time of a real camera is mimicked by averaging over many instantaneous simulations at a short interval, thus providing us with blurred speckle that yields information about the dynamics of the underlying flow system. All speckle images are processed by computing the [speckle contrast](#) (for a duration of 35 flow periods) and its frequency spectrum, which we then study: “*If this was an actual measurement of a (medical) device, can we detect specific flow features?*”

We have applied our whole numerical routine to the case of a [carotid artery](#) suffering from atherosclerosis in the [internal carotid artery \(ICA\)](#), to which a heartbeat-like input signal was applied. Our fluid dynamics simulations compare well with experiments. The velocity is higher in narrow regions, such as the [stenosis](#). Directly downstream and upstream of the stenosis there is a flow region with [circulation](#). Depending on the present input flow rate during the heartbeat cycle, the circulation varies in strength. At the bifurcation of the artery there is a stagnation point. In other parts of the artery, the flow behaves ‘nicely’, with a Poiseuille-like flow profile.

We then used our optics code on five sites in the artery: (A) near the inlet, (B) at the bifurcation, (C) inside the circulation and (D) in the stenosis in the [ICA](#), and (E) in the [external carotid artery \(ECA\)](#). By comparing sites B and E to site A, we found virtually the same [frequency signature](#), with just some more noise in site B caused by the bifurca-

⁶In our work we have used OpenFOAM [30], but in principle *any* CFD code may be used.

tion. In sites C and D, however, the frequency signature was different. Before the stenosis (site C), the noise remains unchanged, but the second-order **frequency mode** gets suppressed, presumably by the inertia of the circulating flow. Inside the stenosis (site D), the speckle contrast decreases rapidly due to the higher velocity, and the frequency signature changes considerably: there is much more noise, and the higher-order frequency modes become more prominent while the second-order frequency mode is slightly suppressed. In other words, the signal is much more complex than in other regions in the artery due to the upstream circulation before the stenosis, which **spectral analysis** of the speckle contrast is able to detect.

In conclusion, we have shown that more complex flow characteristics are reflected in the speckle contrast time series as obtained from dynamic **LSCI**. Therefore, spectral analysis of the speckle contrast can distinguish regions with complex flow. Consequently, the stenosis – and thus the disease atherosclerosis – *can* be detected with dynamic **LSCI**.

We are confident that our approach should be adaptable to **in-vivo** situations, as we have previously used speckle imaging for an in-vivo carotid artery [7]. To that end, future work should definitely study the region around the stenosis in more detail: what does the transition in frequency signature from upstream to all the way downstream of the stenosis look like precisely? Can we also detect the early stages of atherosclerosis in which the stenosis is not yet as large? Will the angle of measurement influence the results? And how will the patient's skin (i.e., static scatterers) affect the measurements? Finally, given the success of dynamic **LSCI** to detect flow features in our present context, it would be interesting to study many different kinds of flow to determine what other applications dynamic **LSCI** might have to study in particular flow systems that are currently difficult to measure, e.g., due to the opaque nature of said flow.

BIBLIOGRAPHY

1. Meschia, J. F., Klaas, J. P., Brown Jr, R. D. & Brott, T. G. Evaluation and management of atherosclerotic carotid stenosis. *Mayo Clinic Proceedings* **92**, 1144–1157 (2017).
2. Kruizinga, P. *et al.* Photoacoustic imaging of carotid artery atherosclerosis. *Journal of Biomedical Optics* **19**, 1–3 (2014).
3. Asakura, T. & Takai, N. Dynamic laser speckles and their application to velocity measurements of the diffuse object. *Applied Physics* **25**, 179–194 (1981).
4. Zakharov, P. *et al.* Dynamic laser speckle imaging of cerebral blood flow. *Optics Express* **17**, 13904–13917 (2009).
5. Heckmeier, M., Skipetrov, S. E., Maret, G. & Maynard, R. Imaging of dynamic heterogeneities in multiple-scattering media. *JOSA A* **14**, 185–191 (1997).
6. Qureshi, M. M. *et al.* Quantitative blood flow estimation in vivo by optical speckle image velocimetry. *Optica* **8**, 1092–1101 (Aug. 2021).
7. Nemati, M., Kenjeres, S., Urbach, H. P. & Bhattacharya, N. Fractality of pulsatile flow in speckle images. *Journal of Applied Physics* **119**, 174902 (2016).
8. Dainty, J. C. in *Topics in Applied Physics* 9 (Springer, Berlin, Heidelberg, 1975).
9. Van der Kooij, H. M. & Sprakel, J. Watching paint dry; more exciting than it seems. *Soft Matter* **11**, 6353–6359 (2015).
10. Van der Kooij, H. M., Fokink, R., van der Gucht, J. & Sprakel, J. Quantitative imaging of heterogeneous dynamics in drying and aging paints. *Scientific Reports* **6**, 34383 (2016).
11. Boas, D. A. & Dunn, A. K. Laser speckle contrast imaging in biomedical optics. *Journal of Biomedical Optics* **15**, 011109 (2010).
12. Welch, A. J., van Gemert, M. J. C., *et al.* *Optical-Thermal Response of Laser-Irradiated Tissue* (Springer, 2011).
13. Sassaroli, A. & Martelli, F. Equivalence of four Monte Carlo methods for photon migration in turbid media. *JOSA A* **29**, 2110–2117 (2012).
14. Davis, M. A. & Dunn, A. K. Dynamic light scattering Monte Carlo: a method for simulating time-varying dynamics for ordered motion in heterogeneous media. *Optics Express* **23**, 17145–17155 (2015).
15. Boas, D. A., Campbell, L. E. & Yodh, A. G. Scattering and Imaging with Diffusing Temporal Field Correlations. *Physical Review Letters* **75**, 1855 (1995).
16. O’leary, M. A., Boas, D. A., Chance, B. & Yodh, A. G. Refraction of Diffuse Photon Density Waves. *Physical Review Letters* **69**, 2658 (1992).

17. Pine, D. J., Weitz, D. A., Chaikin, P. M. & Herbolzheimer, E. Diffusing-Wave Spectroscopy. *Physical Review Letters* **60**, 1134 (1988).
18. Stephen, M. J. Temporal fluctuations in wave propagation in random media. *Physical Review B* **37**, 1 (1988).
19. Durduran, T., Choe, R., Baker, W. B. & Yodh, A. G. Diffuse Optics for Tissue Monitoring and Tomography. *Reports on Progress in Physics* **73**, 076701 (2010).
20. Bosschaart, N., Edelman, G. J., Aalders, M. C. G., van Leeuwen, T. G. & Faber, D. J. A Literature Review and Novel Theoretical Approach on the Optical Properties of Whole Blood. *Lasers in Medical Science* **29**, 453–479 (2014).
21. Dunn, A. K. Laser speckle contrast imaging of cerebral blood flow. *Annals of Biomedical Engineering* **40**, 367–377 (2012).
22. Visualization of perfusion changes with laser speckle contrast imaging using the method of motion history image. *Microvascular Research* **107**, 106–109. ISSN: 0026-2862 (2016).
23. Ansari, M. Z. & Mujeeb, A. Application of motion history image (MHI) on dynamic fluorescent imaging for monitoring cerebral ischemia induced by occlusion of middle cerebral artery (MCA) in mouse brain. *Biomedical Spectroscopy and Imaging* **6**, 135–142 (2017).
24. Aminfar, A., Davoodzadeh, N., Aguilar, G. & Princevac, M. Application of optical flow algorithms to laser speckle imaging. *Microvascular Research* **122**, 52–59. ISSN: 0026-2862 (2019).
25. Duncan, D. D. & Kirkpatrick, S. J. Can laser speckle flowmetry be made a quantitative tool? *J. Opt. Soc. Am. A* **25**, 2088–2094 (2008).
26. Briers, D. *et al.* Laser speckle contrast imaging: theoretical and practical limitations. *Journal of Biomedical Optics* **18**, 066018 (2013).
27. Fercher, A. F. & Briers, J. D. Flow visualization by means of single-exposure speckle photography. *Optics Communications* **37**, 326–330 (1981).
28. Van As, K., Simons, B. A., Kleijn, C. R., Kenjeres, S. & Bhattacharya, N. The Dependence of Speckle Contrast on Velocity: A Numerical Study. *Journal of the European Optical Society* **18** (2022).
29. Van As, K., Boterman, J., Kleijn, C. R., Kenjeres, S. & Bhattacharya, N. Laser speckle imaging of flowing blood: A numerical study. *Physical Review E* **100**, 033317 (2019).
30. *The OpenFOAM Foundation* (<http://www.openfoam.org/>) 2018. <http://www.openfoam.org/>.
31. *Ansys Fluent* (<https://www.ansys.com/products/fluids/ansys-fluent>) 2018. <https://www.ansys.com/products/fluids/ansys-fluent>.
32. Kenjereš, S. On recent progress in modelling and simulations of multi-scale transfer of mass, momentum and particles in bio-medical applications. *Flow, Turbulence and Combustion* **96**, 837–860 (2016).

33. Li, R. *Computational Fluid Dynamics Methodology for Simulation of Blood Flow in Patient-Specific Carotid Artery: Validation of Two-Dimensional Three-Components (2D3C) PIV* MA thesis (TUDelft, Department of Chemical Engineering, 2017).
34. Muralidharan, A. *In-Vitro Validation of Cardiovascular Flows using Particle Imaging Velocimetry: A patient-specific validation study* MA thesis (TUDelft, Department of Chemical Engineering, 2017).
35. Nemati, M. *et al.* Application of full field optical studies for pulsatile flow in a carotid artery phantom. *Biomedical optics express* **6**, 4037–4050 (2015).
36. Ferziger, J. H., Perić, M. & Street, R. L. *Computational methods for fluid dynamics* (Springer, 2002).
37. Nemati, M., Presura, C. N., Urbach, H. P. & Bhattacharya, N. Dynamic light scattering from pulsatile flow in the presence of induced motion artifacts. *Biomed. Opt. Express* **5**, 2145–2156 (2014).
38. Mie, G. Beiträge zur Optik trüber Medien, speziell kolloidaler Metallösungen. *Annalen der Physik* **330**, 377–445 (1908).
39. Bohren, C. F. & Huffman, D. R. *Absorption and Scattering of Light by Small Particles* (John Wiley & Sons, 2008).
40. Stratton, J. A. *Electromagnetic Theory* (John Wiley & Sons, 2007).
41. Hulst, H. C. *Light Scattering by Small Particles* (Courier Corporation, 1981).
42. Mishchenko, M. I., Travis, L. D. & Mackowski, D. W. T-matrix computations of light scattering by nonspherical particles: A review. *Journal of Quantitative Spectroscopy and Radiative Transfer* **55**, 535–575 (1996).
43. Briers, J. D. & Webster, S. Laser speckle contrast analysis (LASCA): a non-scanning, full-field technique for monitoring capillary blood flow. *Journal of Biomedical Optics* **1**, 174–180 (1996).
44. Goodman, J. W. in *Laser Speckle and Related Phenomena* 9–75 (Springer, 1975).
45. Li, J., Yao, G. & Wang, L. V. Degree of polarization in laser speckles from turbid media: Implications in tissue optics. *Journal of Biomedical Optics* **7**, 307–312 (2002).
46. Bandyopadhyay, R., Gittings, A. S., Suh, S. S., Dixon, P. K. & Durian, D. J. Speckle-visibility spectroscopy: A tool to study time-varying dynamics. *Review of Scientific Instruments* **76**, 093110 (2005).
47. Draijer, M., Hondebrink, E., van Leeuwen, T. & Steenbergen, W. Review of laser speckle contrast techniques for visualizing tissue perfusion. *Lasers in Medical Science* **24**, 639 (2009).

7

CONCLUSIONS AND OUTLOOK

In this research thesis, we set out to investigate means in which light may be used as a technique for medical diagnosis applications, particularly focusing on diagnosis of blood flow related diseases. Prime advantages of light measurement techniques are that they are **non-invasive**, usable **in-vivo** and **real-time**, potentially accurate, and all while being cheap as well. These are all very desirable properties for medical measurement techniques.

Light is already used for medical diagnosis – e.g., to measure a heartbeat using **Photoplethysmography (PPG)** – but it yields much greater potential than is currently being used. For example, performing velocimetry measurements may in the future yield more than just the signature of a heartbeat: it may potentially be used to detect a **sclerosed** artery prematurely, enabling the timely treatment of diseases like **atherosclerosis**. Our research question is:

Can we perform velocimetry measurements using light scattered by in-vivo flowing blood for medical diagnosis purposes?

To that end, we have studied the interferometric scattering of light by an ensemble of dynamic spherical particles, which represent red blood cells flowing through an artery. We take a numerical simulation approach, as this enables us to vary input parameters easily at will. By performing **numerical experiments** – i.e., generating an output for each set of input parameters – we are able to find relationships between input and output, and thus able to tell what a certain output implies about the underlying system being measured.

We have developed a multi-physics computer code in Chap. 2: (i) the **Computational Fluid Dynamics (CFD)** code is able to simulate the movement of tracer particles in any flow, including complex arterial flows; (ii) the optics code is based on **Mie theory**. It takes the particle positions from the **CFD** code, and computes the instantaneous scattering of a plane wave of coherent light¹, including **multiscattering**, and computes the intensity

¹I.e., of a laser beam.

as would be measured by a physical camera. The result is a **speckle pattern**, which is characteristic for interferometric scattering by randomly distributed **scatterers**.

In order to study real measurements of dynamic systems, we must mimic the finite **exposure time** of a physical camera, as we need to obtain a numerical result that represents a physical measurement. We achieve that by taking the mean of many optics simulations that are performed in very rapid succession, essentially blurring the light measurement². By repeating the optics code simulations for each fluid time step, we obtain a time series of speckle patterns.

To make our *dynamic* simulations computationally feasible, we have made several simplifications; most notably, we assume that particles are sufficiently small and far apart to be considered to be in each other's far-field³. Although simplifications evidently affect the obtained speckle patterns, they do not restrict us from obtaining meaningful results, especially regarding the dynamics of the underlying scatterers.

Using our combined multi-physics code, we can perform **Laser Speckle Contrast Imaging (LSCI)** simulations. To that end, we use the **speckle contrast** as a metric to analyze the speckle patterns, which equals the ratio of the signal's standard deviation to its mean. However, there exist large-scale intensity fluctuations⁴ that affect the computed speckle contrast. By computing the speckle contrast using **windowing**⁵, we negate their influence, enabling us to obtain results representing the physical reality.

7.1. CONCLUSIONS, DISCUSSION AND REMAINING QUESTIONS

Using our newly developed numerical framework, we are able to perform simulations to help answering our research question. First, we subdivide the question into three main parts, the first being:

*Can we use **Laser Speckle Contrast Imaging (LSCI)** to measure the **frequency signature** of a flow modulated by a **pulsatile heartbeat-like signal**?*

In Chap. 4 we have studied plug flow and laminar flow in a simple cylindrical geometry, representing an artery. **Plug flow** is representative for a **non-Newtonian fluid** (such as blood) in a large artery, whereas laminar **Poiseuille flow** is a more appropriate model for blood flow in a small artery. Suspended in the flow are spherical tracer particles, representing red blood cells.

To model a heartbeat, we firstly modulated the flow rate using a sinusoidal input signal. From a **Fourier analysis** of the computed speckle contrast evolution, the original input frequency could successfully be reconstructed. In Poiseuille flow, unlike plug flow, there is a relative motion between the scatterers, which results in a speckle phenomenon called **speckle boiling**. Very insightful was that we found that speckle boiling introduces a uniform spectral noise to the **Fourier spectrum**, which could easily be filtered out, allowing for the same quality of reconstruction as we obtained for plug flow.

²See Sec. 4.2.1.

³That is, scattered waves are spherical waves. We assume that these spherical waves are locally just plane waves, which is true for small particles that are sufficiently far apart.

⁴These are caused by interference at length scales that are not of interest to us.

⁵See Sec. 4.2.4 and Fig. 4.3c.

Secondly, we modelled a more realistic scenario of a heartbeat-shaped input signal, comprising multiple frequencies. Once again, we could successfully reconstruct the input frequencies and found good agreement with earlier experimental results.

As a first conclusion: yes, LSCI is able to detect the frequency signature of a temporally modulated flow, allowing for the reconstruction of the temporal input signal (e.g., measuring a heartbeat).

However, we still have a deviation to that conclusion left to resolve. For the heartbeat-shaped input signal, we could correctly reconstruct the first- and second-order frequency modes, but higher-order modes started to deviate. In fact, we may only expect the exact same frequency signature from our speckle contrast measurements, if there is a linear relationship between velocity and speckle contrast. Our results indicate otherwise. We found that when the velocity is low, the speckle contrast drops sharply from one towards zero, whereas for high velocities it approaches the asymptotic value of zero slowly. So what exactly is the relationship between speckle contrast and velocity?

This naturally leads us to our next research question in Chap. 5:

Can we use LSCI to measure the velocity of the underlying scatterers in a turbid flow?

Particle Image Velocimetry (PIV) is a very popular technique for velocimetry that can only be used in situations where direct imaging is possible. Therefore, studying (light) techniques that can perform indirect imaging, such as LSCI, are of prime interest for velocimetry in such turbid media. Using the same geometry as before, we have studied the effect of fluid velocity V and camera integration time T on the measured speckle contrast K . Our first finding is that V and T are irrelevant individually, but rather are intertwined through the quantity $d = VT$, which is the distance scatterers have travelled during the camera integration time. This makes sense, since K scales with the amount of blurring in the measured speckle image, which is determined by the amount of movement – and thus by d .

While there exist analytical models that describe how K depends on the speckle decorrelation time τ_c , it remained elusive how τ_c depends on d and, therefore, how K depends on d . By fitting several analytical models to our simulation results, we have found that the Gaussian model in Eq. (5.3) performs best. In particular, at low values of d the model performs very well, whereas at high values of d the model starts to deviate from our numerical findings. Future research will need to determine whether this is a simulation artefact, or whether this is physics still to be studied.

Through comparison with the Gaussian model, we have found in Eq. (5.6) that

$$\frac{\tau_c}{T} \approx 1.06 \frac{w_{\text{speckle}}}{d}, \quad w_{\text{speckle}} = \frac{\lambda z}{D}, \quad (7.1)$$

where w_{speckle} is the characteristic size of a speckle, which depends on the wavelength λ , and on the imaging system: camera distance z and aperture width D . The number 1.06 is a $O(1)$ fitting constant, that likely appears by the lack of a ‘perfect’ definition for τ_c and w_{speckle} ; a topic for future research is to determine whether this number depends on other yet unknown parameters. Regardless of that, our numerical experiments have

provided further evidence to resolve a long-standing disagreement in the literature regarding how K and τ_c depend on V .

Another very important implication of our findings, is that there exists a region in which K is most sensitive to changes in velocity. This means that a small change in velocity results in a large change in K , which results in the desirable property of achieving a more accurate measurement of slightly differing velocities. Based on our simulation results, we hypothesize that the ‘region of high-sensitivity’ is governed by the equation⁶:

$$d = c_{\text{rohs}} \cdot w_{\text{speckle}} \rightarrow T = c_{\text{rohs}} \cdot \frac{\lambda z}{VD}, \quad (7.2)$$

where ideally⁷ $c_{\text{rohs}} \in [1, 10]$ for all values of V in the velocity field being measured⁸. However, whereas we have studied the effect of d thoroughly, future research should still check the veracity of this expression as a whole through (numerical) experiments on the imaging parameters z , D and λ . Nevertheless, this expression makes sense physically: K measures the ‘blurring’ of a speckle image due to scatterer movement, which should have the largest effect when the distance travelled d during time T is a bit larger than the size of a typical speckle w_{speckle} .

The consequence of this expression is that by choosing T , z , D and λ cleverly, it should almost always be possible to perform measurements in the high-sensitivity range, provided that an estimate of the typical V can be made beforehand. Should that be impossible, then a device could be designed that varies these quantities dynamically, until the measured V satisfies the expected high-sensitivity range through Eq. (7.2). The result would be more accurate velocimetry measurements, in turbid media, that are less prone to measurement uncertainties than without the usage of Eq. (7.2).

In conclusion: yes, LSCI may be used to measure the velocity of the scatterers in a turbid flow.

While our present research reveals a quantitative relationship between K and V , and what values for the imaging parameters are required to perform accurate measurements, future research will be required to determine the influence of other parameters on their relationship.

Now that we can reliably measure velocities, and changes in velocity, we take the step towards the medical application of detecting atherosclerosis in Chap. 6:

Can we detect atherosclerosis from light scattered by in-vivo flowing blood?

In the arteries of a patient suffering from atherosclerosis, a **plaque** forms inside the artery at the arterial wall, causing narrowing and stiffening of the artery. Should the disease go undetected and thus untreated, the plaque will grow larger. Eventually, the

⁶From our simulations we know that $d \in [10^{-5}\text{m}, 10^{-4}\text{m}]$ is our ‘region of high-sensitivity’. Now, since $K = K(\tau_c/T)$ and $\tau_c/T = w/d$, it follows that K retains the same value as long as $d \sim w$; hence our hypothesis.

⁷However, as discussed above, our simulation results start to deviate from the Gaussian expression for high values of d ; therefore, until future research resolves that, it will be safest to choose $c_{\text{rohs}} \in [1, 5]$, as in this region the Gaussian expression matches our results within our experimental standard deviations.

⁸This may not always be possible for any given situation. Should it be impossible, then the values should be tweaked such that the velocities of greatest interest are around the optimal value: $c_{\text{rohs}} \approx 2$.

plaque could come loose and could result in a complete blockage downstream, e.g., causing a stroke. Hence early detection of atherosclerosis is pivotal to a patient's chances. Since the flow profile in the sclerosed region will be different than elsewhere, a technique that is able to measure the disturbed flow field will also be able to detect suspicious regions, which LSCI can do cheaply. We would expect a locally higher velocity in the sclerosed region with possibly a vortex upstream as the stenosis grows larger. Far more expensive techniques, such as MRI, may subsequently be used to determine whether a suspicious region is indeed atherosclerosis.

To that end, we use a model of a complex patient-specific carotid artery that is suffering from atherosclerosis in the internal carotid artery. We have simulated the flow using Computational Fluid Dynamics (CFD), and subsequently validated our obtained flow profiles against other simulations and physical experiments, obtaining a good match. We have coupled the CFD code to our own optics code fully modularly, which now permits us to simulate dynamic LSCI on any flow geometry. Inside the artery, we choose to study five specific characteristic sites shown in Fig. 7.1: (A) near the inlet, (B) at the bifurcation, (C) inside the circulation and (D) in the stenosis in the internal carotid artery, and (E) in the external carotid artery.

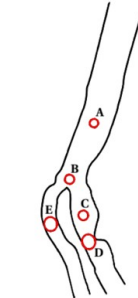


Figure 7.1: Carotid artery with five sites.

Site (A) is near the inlet, and serves as our reference, where the flow has a 'nice' Poiseuille flow profile. In the external artery in site (E) we found virtually the same frequency signature⁹ as in site (A), as we would expect since there is a Poiseuille flow profile in site (E) as well, but the values of the speckle contrast in site (E) are lower than in site (A) due to the higher velocity in site (E). In site (B) we have found virtually the same frequency signature as in site (A), but with a $\sim 10\%$ reduction of the second-order frequency mode and with more added noise to the signal, caused by more relative motion between the particles around the bifurcation and consequently more speckle boiling.

In site (C) we find less extreme and slower velocity fluctuations, resulting in a suppressed second-order frequency mode with a similar amount of spectral noise, compared to site (A). We observe that the circulation's strength varies over the course of a heartbeat cycle, i.e., the circulation's inertia keeps the flow going at the times when the input flow rate decreases. The consequence of less extreme and slower velocity fluctuations is the suppression of higher-order frequency modes, since the slow fluctuations tend to be more sine-like, which comprises a single frequency. Therefore, suppression of higher-order frequency modes is characteristic for a circulation region.

In site (D), where the artery is more narrow, we obtain roughly double the centre velocity of the other sites and consequently the measured frequency signature is considerably different: (i) there is much more spectral noise, and (ii) the second-order frequency mode is slightly suppressed, whereas (iii) higher-order frequency modes become more prominent. We would not expect more speckle boiling in this region, as there should not necessarily be much more relative motion between the particles; however, the high velocity results in low speckle contrast values. From Eq. (7.2) we find that these measurements have $c_{\text{rohs}} \approx 3 \cdot 10^1$, which is outside the region of high-sensitivity, and thus

⁹By which we mean that the relative height of the higher-order frequency modes is the same, at least until the signal-to-noise ratio becomes too small from the fifth-order frequency mode and above.

causes the spectral noise.¹⁰ Finally, the introduction of new higher-order frequency flow features is presumably caused by the unsteadiness of the preceding circulation region.

In conclusion: yes, LSCI holds great promise for detecting atherosclerosis, because measurements from the sclerosed region show a considerably different frequency signature than elsewhere in the carotid artery.

When a stenosis has a buildup of sufficiently much plaque, a circulation region will form before it. In said region, the circulation's inertia will suppress the higher-order frequency modes, while its unsteadiness creates more prominent higher-order frequency modes inside the downstream stenosis. Furthermore, inside the narrowed stenosis, there will be a higher velocity, which can be detected through a lower mean speckle contrast value. All these detection features combined enables us to detect a sclerosed artery – or at least label a region as suspicious, after which a more precise yet far more expensive technique such as MRI can determine whether it is indeed atherosclerosis. While the circumstances of our simulations are not yet identical to the true in-vivo situation, we are confident that future research will show how to adapt our findings to in-vivo, as we have previously already used speckle imaging for an in-vivo carotid artery successfully¹¹.

Our above conclusions enable us to answer our main research question, or at least within the confines of the specific applications we have studied.

In conclusion: yes, we can perform velocimetry measurements using light scattering from turbid media, for which we have revealed an ideal parameter range that should be used.

And, since this includes in-vivo flowing blood:

Yes, we can use this technique for medical diagnosis purposes, such as detecting (periodic) movements (e.g., measuring a heartbeat) or diseases detectable through velocimetry or through the appearance of complex flows (e.g., atherosclerosis).

Our main contribution is the development of a numerical simulation framework capable of studying LSCI on any flow system, which thus far has already shown the potential that LSCI has to become a truly versatile, cheap, in-vivo, and non-invasive technique for medical diagnosis purposes.

¹⁰By tweaking the measuring parameters cf. Eq. (7.2), we can obtain a different result, however, we chose to keep the same parameters in every site, as that is what a measurement device would measure by 'scanning' past the artery.

¹¹See: Nematı, M., Kenjeres, S., Urbach, H. P. & Bhattacharya, N., *Fractality of pulsatile flow in speckle images*. Journal of Applied Physics 119 (2016).

7.2. OUTLOOK

We have shown the great potential of [Laser Speckle Contrast Imaging \(LSCI\)](#) through its ability to measure a heartbeat, perform velocimetry measurements in turbid media, and to identify suspicious regions in the carotid artery to detect the disease atherosclerosis. While we have taken huge steps towards those ends, future research is still required to put our research into practice.

Firstly, we have made several assumptions in developing our numerical model, the first being a far-field assumption in which we assume that the scatterers are ‘sufficiently far apart’. This assumption does not hold for the red blood cell density in blood; however, it does hold in our simulations as our simulations simulate dilute blood due to computational constraints.¹² The primary consequence of the diluteness of our simulation is that the effect of multiscattering is less prevalent than it would be in reality. Multiscattering has the effect of reducing the speckle contrast, most notably for static speckle: our simulations in Chap. 5 yield a speckle contrast value of approximately 1.0 at a zero velocity (i.e., static scattering), whereas similar experiments¹³ find a lower [speckle contrast](#) at a zero flow velocity. However, this effect decreases relatively at higher velocities, and thus we expect this assumption to not have a great effect on our dynamic simulations when compared to other noise factors.

Another assumption is that the scatterers are spherically shaped, whereas in reality red blood cells have a very distinct shape. By their azimuthal symmetry, spherical particles only use the polar angle to determine the strength of the scattering, while on the other hand red blood cells have a rather complex angular scattering behavior. In our application – the carotid artery – it is fair to assume that this effect on the final results is small, since the red blood cells are mostly aligned with one another, and its effect should statistically largely cancel out by the large number of particles being considered. It would, however, be good if future research studies the effect of the shape of the particles¹⁴, especially in applications involving narrow arteries in which the red blood cells become elongated, resembling cylinders more closely than spheres.

Secondly, many improvements to our model can only be made, if we can overcome the computational time constraints. To that end, we had already precomputed the scattering matrix, which greatly reduced the time complexity of our algorithm at the expense of a greatly increased memory complexity. Next, we could consider implementing a connection matrix, which holds information about the distance between each pair of scatterers. A scattered wave falls off with r^2 , therefore it is reasonable to assume that multiscattering caused by distant particles will have a negligible effect on the camera’s measurement. A connection matrix is a computationally cheap method of excluding the

¹²It would be interesting to see the effect of the far-field assumption, which is possible by deploying the T-matrix method to eliminate the far-field assumption. However, this is as of present way too expensive to compute in a *dynamic* system of hundreds of particles, but perhaps a comparison could be made in a static system for comparison purposes.

¹³E.g., G. B. Loozen, Monitoring pulsating flow with dynamic speckle fields. MSc thesis, TUDelft (2015).

¹⁴Particle shape can be taken into account using the T-matrix method, which we haven’t used, since it is not computationally feasible for our dynamic simulations with many scatterers.

interaction of certain pairs of distant particles. However, we ought to be careful here: the scattering matrix depends on the scattering angle, which may (in our situation) differ by a factor ~ 1000 in amplitude depending on the angle between the two scatterers (see Fig. 2.4). Consequently, a particle being ~ 30 times further away than another particle might still contribute more to the final measurement. Fortunately, the scattering matrix is known, and this may thus be taken into consideration by constructing a weighted connection matrix.

Another computational improvement would be to refine the multiscattering **convergence** criterion. Currently, we consider the multiscattering iterations to be converged if for the interaction of each pair of particles the amplitude of the scattered light at the location of every other particle is negligible compared to the amplitude of the incoming plane wave. This criterion is way too strict, since many interactions will have become negligible many iterations before the last interaction becomes negligible. The solution could be similar to the above suggested weighted connection matrix: the matrix could be adapted dynamically with successive multiscattering iterations by turning ‘off’ the negligible interactions.

Thirdly, our computational model may be expanded to include more relevant **in-vivo** effects. For example, the skin around the artery will act like a collection of static scatterers, which is expected to have the effect of introducing an offset to the speckle contrast¹⁵. To get around this, we can probably redefine our region of sensitivity in Eq. (7.2) to be a bit more strict, or as a worst case, patient-specific calibration may unfortunately be required. Future research should identify what precisely the influence of static scatterers depends on, and possibly come up with an automatic calibration procedure (e.g., through a more advanced multiexposure algorithm).

Next, an important future question is in which stage we can detect atherosclerosis, more specifically: *can we already detect atherosclerosis in its earlier stages?* It is known that the arterial wall undergoes a pulsatile radial motion (i.e., widening and narrowing) during a heartbeat cycle. However, as an artery becomes more sclerosed, it stiffens, reducing said radial motion. Therefore, if we are able to measure the amount of radial motion, we might have a new way to detect atherosclerosis, in addition to our findings from Chap. 6.

In order to improve the capability of dynamic **LSCI** to detect atherosclerosis, the region around the stenosis should be studied in more detail. In other words, by scanning a device along an artery, how would the measurement of that device transition as it scans along a sclerosed artery? In Chap. 6 we had found that our measurement in the circulation region before the stenosis was notably different than elsewhere. With further study, this could potentially become another characteristic of the various stages of atherosclerosis, or it could potentially even provide a new cheap way of measuring **vorticity** in various other turbid media.

Furthermore, we know that **LSCI** is primarily sensitive to transverse motion, as that results in **translating speckle** and some **speckle boiling**, whereas the out-of-plane motion only results in speckle boiling. Our findings in Chap. 5 work, because we were measuring

¹⁵See: Boas, D. A., & Dunn, A. K. (2010). Laser speckle contrast imaging in biomedical optics. *Journal of biomedical optics*, 15(1).

mostly translating speckle by measuring at a 90° angle. In a real in-vivo application, the doctor may very well be holding the measuring device at a different angle. Although for measuring the carotid artery the measurement angle should automatically always be near 90° , we should still study the effect of the angle of measurement. After all, it is not yet known whether even small angle differences may already have a big impact on the results.

LSCI being primarily sensitive to transverse motion, allows us to measure the two-dimensional transverse velocity field. As was discussed in Chap. 4, regional laser Doppler techniques are sensitive to the third dimension: the out-of-plane motion. Therefore, it should be explored whether combining these two techniques can provide an accurate flowmetry technique for turbid media.

Fourthly, the more generic **Laser Speckle Imaging (LSI)** method should be capable of measuring more than a heartbeat or the velocity, especially if we start considering other metrics than LSCI's speckle contrast. Light scattering depends on the **refractive index** of the scatterers, and for red blood cells their refractive index happen to depend on their oxygen content. Therefore, LSI should be adoptable to blood perfusion measurements. Additionally, the shape of red blood cells will also affect the scattered light, as we had already discussed above. With further research, LSI could thus potentially be used to measure the dynamic morphology of red blood cells.

Finally, as our technique is further developed, different applications will likely be attainable. These could include, but are not limited to: guided drug delivery, measuring breathing (i.e., movement of the lungs), the oil industry, and other industrial processing applications. Wherever the radiation and detection of radiation is possible behind opaque media, LSI should be usable for flow detection, with the limitation being the absorptivity of the medium. In particular, applications with complex flows in turbid media are all good candidates for LSI.

A

MIE THEORY – THE DETAILS

This appendix gives some more details to the arguments given in Sec. 1.1, which was the derivation of [Mie theory](#). Consequently, this appendix is not meant to be read as a stand-alone text.

A.1. WHY ARE TERMS OMITTED FROM THE EXPANSION?

Instead of writing Eqs. (1.21-1.24), we can include the ignored terms, like such:

$$\vec{E}_1 = \sum_{n=1}^{\infty} E_n \sum_{m=0}^n (c_{mn} \vec{M}_{omn}^{(1)} + d_{mn} \vec{N}_{emn}^{(1)} + v_{mn} \vec{N}_{omn}^{(1)} + w_{mn} \vec{M}_{emn}^{(1)}), \quad (\text{A.1})$$

$$\vec{H}_1 = \frac{k_1}{i\omega\mu_1} \sum_{n=1}^{\infty} E_n \sum_{m=0}^n (c_{mn} \vec{N}_{omn}^{(1)} + d_{mn} \vec{M}_{emn}^{(1)} + v_{mn} \vec{M}_{omn}^{(1)} + w_{mn} \vec{N}_{emn}^{(1)}), \quad (\text{A.2})$$

$$\vec{E}_s = \sum_{n=1}^{\infty} E_n \sum_{m=0}^n (a_{mn} \vec{M}_{omn}^{(3)} + b_{mn} \vec{N}_{emn}^{(3)} + p_{mn} \vec{N}_{omn}^{(3)} + q_{mn} \vec{M}_{emn}^{(3)}), \quad (\text{A.3})$$

$$\vec{H}_s = \frac{k_2}{i\omega\mu_2} \sum_{n=1}^{\infty} E_n \sum_{m=0}^n (a_{mn} \vec{N}_{omn}^{(3)} + b_{mn} \vec{M}_{emn}^{(3)} + p_{mn} \vec{M}_{omn}^{(3)} + q_{mn} \vec{N}_{emn}^{(3)}), \quad (\text{A.4})$$

A.1.1. EXTRACT THE COEFFICIENTS USING ORTHOGONALITY

Define the functional inner product of two vectors as:

$$\langle \vec{a}, \vec{b} \rangle = \int_0^{2\pi} \int_0^{\pi} \vec{a} \cdot \vec{b} \sin(\theta) d\theta d\varphi, \quad (\text{A.5})$$

then it is possible to show that under this inner product all \vec{M}_{pmn} and $\vec{M}_{p'm'n'}$ are orthogonal¹ (same for \vec{N}), and all \vec{M} with all \vec{N} , i.e., the [Vector Spherical Harmonics \(VSHs\)](#) are

¹That is, the functional inner product equals 0 $\forall (p \neq p' \cup m \neq m' \cup n \neq n')$. Here, p refers to either e or o .

linearly independent if tested using this inner product. This permits the coefficients to be extracted individually, e.g.:

$$\langle \vec{E}_s, \vec{M}_{omn} \rangle = E_n a_{mn} \langle \vec{M}_{omn}^{(3)}, \vec{M}_{omn} \rangle, \quad (\text{A.6})$$

where \vec{M}_{omn} may have any **Bessel function**, since it is merely a constant in the integral of Eq. (A.5), as it only depends on the radial coordinate.

It is, however, not trivial to apply this functional inner product to the **Boundary Conditions (BCs)** Eqs. (1.10-1.13), as the BCs are **anisotropic**. However, since $\vec{E} \cdot (c_1 \hat{\theta} + c_2 \hat{\phi})$ for any $\{c_1, c_2\}$ satisfies the tangential BC and since $\vec{M} \cdot \hat{r} = 0$, it immediately follows that the functional inner product with $\vec{M}^{no\rho}$ will satisfy the tangential BC too. That is, c_1 and c_2 above must be the same for both \vec{E}_1 and \vec{E}_2 to satisfy the BC. This is only the case if the ρ -dependent terms (which are material-dependent!) of \vec{M} are excluded, which we call per definition $\vec{M}^{no\rho}$. This does not affect the **orthogonality**, since the ρ -dependent part is merely a constant in the integral of Eq. (A.5). So, we may write:

$$\langle \vec{E}_1, \vec{M}_{emn}^{no\rho} \rangle_{\rho=y} = E_n w_{mn} \langle \vec{M}_{emn}^{(1)}, \vec{M}_{emn}^{no\rho} \rangle_{\rho=y} = E_n q_{mn} \langle \vec{M}_{emn}^{(3)}, \vec{M}_{emn}^{no\rho} \rangle_{\rho=x} = \langle \vec{E}_s, \vec{M}_{emn}^{no\rho} \rangle_{\rho=x}, \quad (\text{A.7})$$

where $\vec{M}_{emn}^{(1)}$ was chosen for convenience, because the incident field does not possess the term, and $x \equiv k_2 a$ and $y \equiv k_1 a$ are as used in Eq. (1.26) (and below it) and represent the sphere's boundary in ρ -space. Henceforth, the superscript $no\rho$ will be left out, but it is always present on the **VSH** with which we take the functional inner product.

\vec{N} is a different story: when applying Eq. (A.6) using some \vec{N} , $\vec{E} \cdot \hat{r}$ is involved and we cannot 'simply' use the tangential BC, Eq. (1.12):

$$\langle \vec{E}_1, \vec{N}_{omn} \rangle_{\rho=y} = E_n v_{mn} \langle \vec{N}_{omn}^{(1)}, \vec{N}_{omn} \rangle_{\rho=y} \neq E_n p_{mn} \langle \vec{N}_{omn}^{(3)}, \vec{N}_{omn} \rangle_{\rho=x} = \langle \vec{E}_s, \vec{N}_{omn} \rangle_{\rho=x}, \quad (\text{A.8})$$

because

$$(c_0 \vec{E}_1 \cdot \hat{r} + c_1 \vec{E}_1 \cdot \hat{\theta} + c_2 \vec{E}_1 \cdot \hat{\phi}) \Big|_{\rho=y} \neq (c_0 \vec{E}_2 \cdot \hat{r} + c_1 \vec{E}_2 \cdot \hat{\theta} + c_2 \vec{E}_2 \cdot \hat{\phi}) \Big|_{\rho=x},$$

which would only hold if $\epsilon_1 = \epsilon_2$ in Eq. (1.10). In Bohren & Huffman² this problem is not mentioned anywhere, although the solution is lurking from deep within the derivation. As it turns out, the \hat{r} -component of \vec{N} satisfies orthogonality on its own, i.e.,

$$\langle (\vec{N}_{pmn} \cdot \hat{r}) \hat{r}, \vec{N}_{p'm'n'} \rangle = 0 \quad \forall (p \neq p' \cup m \neq m' \cup n \neq n'). \quad (\text{A.9})$$

So, whereas the $\hat{\theta}$ and $\hat{\phi}$ components need each other, \hat{r} can do the job on its own. Now, since $(\vec{N} \cdot \hat{r}) \hat{r}$ satisfies orthogonality alone, it then follows by the linearity of the functional inner product Eq. (A.5), that $\vec{N}^r = \vec{N} - (\vec{N} \cdot \hat{r}) \hat{r}$ must too³. \vec{N}^r is a shorthand notation to fix the inequality in Eq. (A.8):

$$\langle \vec{E}_1, \vec{N}_{omn}^r \rangle_{\rho=y} = E_n v_{mn} \langle \vec{N}_{omn}^{(1)}, \vec{N}_{omn}^r \rangle_{\rho=y} = E_n p_{mn} \langle \vec{N}_{omn}^{(3)}, \vec{N}_{omn}^r \rangle_{\rho=x} = \langle \vec{E}_s, \vec{N}_{omn}^r \rangle_{\rho=x}, \quad (\text{A.10})$$

²Bohren, C. F., & Huffman, D. R. (2008). *Absorption and scattering of light by small particles*. John Wiley & Sons.

³Note that \vec{N}^r is just \vec{N} with its \hat{r} -component set to 0. Here, the superscript r stands for 'reduced'.

A.1.2. FIND THE COEFFICIENTS

Now that we have a way to extract individual coefficients, we can do so for all coefficients for both \vec{E} and \vec{H} , which will yield exactly enough equations to solve the problem. Since the process is identical for every coefficient, let us solely observe what happens to v_{mn} and p_{mn} . These coefficients belong to the VSH \vec{N}_{omn} (in the equations for \vec{E} , Eqs. (A.1 and A.3)) and is not contained within the incident field Eq. (1.19)⁴. We can use Eq. (A.10) and its equivalent for \vec{H} :

$$E_n v_{mn} \langle \vec{N}_{omn}^{(1)}, \vec{N}_{omn}^r \rangle_{\rho=y} = E_n p_{mn} \langle \vec{N}_{omn}^{(3)}, \vec{N}_{omn}^r \rangle_{\rho=x}, \quad (\text{A.11})$$

$$\frac{k_1}{i\omega\mu_1} E_n v_{mn} \langle \vec{M}_{omn}^{(1)}, \vec{M}_{omn} \rangle_{\rho=y} = \frac{k_2}{i\omega\mu_2} E_n p_{mn} \langle \vec{M}_{omn}^{(3)}, \vec{M}_{omn} \rangle_{\rho=x}. \quad (\text{A.12})$$

If we now use the form of the VSHs, cf. Eqs. (1.16 and 1.17), and the definition of the functional inner product Eq. (A.5), it follows that the only common factors, are the material-dependent terms:

$$\frac{\langle \vec{N}_{omn}^{(1)}, \vec{N}_{omn}^r \rangle_{\rho=y}}{\langle \vec{N}_{omn}^{(3)}, \vec{N}_{omn}^r \rangle_{\rho=x}} = \frac{\psi'_n(y)/y}{\xi'_n(x)/x}, \quad \frac{\langle \vec{M}_{omn}^{(1)}, \vec{M}_{omn} \rangle_{\rho=y}}{\langle \vec{M}_{omn}^{(3)}, \vec{M}_{omn} \rangle_{\rho=x}} = \frac{\psi_n(y)/y}{\xi_n(x)/x}, \quad (\text{A.13})$$

where ψ_n and ξ_n are the Riccati-Bessel functions as introduced in Eqs. (1.29 and 1.30). Upon substitution we may then write:

$$\frac{p_{mn}}{v_{mn}} = \frac{x}{y} \frac{\psi'_n(y)}{\xi'_n(x)}, \quad (\text{A.14})$$

$$\frac{p_{mn}}{v_{mn}} = \frac{x}{y} \frac{k_1 \mu_2}{k_2 \mu_1} \frac{\psi_n(y)}{\xi_n(x)} = \frac{\mu_2}{\mu_1} \frac{\psi_n(y)}{\xi_n(x)} = \frac{x^2}{y^2} \frac{\epsilon_1}{\epsilon_2} \frac{\psi_n(y)}{\xi_n(x)}, \quad (\text{A.15})$$

from which it is seen that, unless we have *very* specific material properties⁵, $p_{mn} = v_{mn} = 0$. A similar derivation will yield that $p_{mn} = q_{mn} = v_{mn} = w_{mn} = 0$ and $a_{mn} = b_{mn} = c_{mn} = d_{mn} = 0$ if $m \neq 1$. In other words, all coefficients for the VSHs which are not contained within the incident field are 0. By analogy, if there is no force to hit a string, the string will not start vibrating spontaneously. Physically, we require a source term for things to get into motion. Also, by linear independence, hitting string #1 cannot cause any string other than string #1 to vibrate.

A.2. DERIVING THE MIE COEFFICIENTS

In the case that $m = 1$, the incident field will provide a source for two VSHs (for every n). Using the notation of the previous section together with the expansions as given in Eqs. (1.21-1.24), the BCs for a_n and c_n read:

$$\langle \vec{E}_s, \vec{N}_{e1n}^r \rangle_{\rho=x} + \langle \vec{E}_i, \vec{N}_{e1n}^r \rangle_{\rho=x} = \langle \vec{E}_1, \vec{N}_{e1n}^r \rangle_{\rho=y}, \quad (\text{A.16})$$

$$\langle \vec{H}_s, \vec{M}_{e1n} \rangle_{\rho=x} + \langle \vec{H}_i, \vec{M}_{e1n} \rangle_{\rho=x} = \langle \vec{H}_1, \vec{M}_{e1n} \rangle_{\rho=y}, \quad (\text{A.17})$$

⁴Finding the non-zero Mie coefficients in which the incident field does contribute is performed in Sec. A.2.

⁵These very specific material properties do not serve a physical problem, since nothing in nature can have an infinite accuracy, which would be required in order to ever satisfy those material properties.

A

which after cancelling E_n and i may be reduced to

$$a_n \langle \vec{N}_{e1n}^{(3)}, \vec{N}_{e1n}^r \rangle_{\rho=x} + d_n \langle \vec{N}_{e1n}^{(1)}, \vec{N}_{e1n}^r \rangle_{\rho=y} = \langle \vec{N}_{e1n}^{(1)}, \vec{N}_{e1n}^r \rangle_{\rho=x}, \quad (\text{A.18})$$

$$a_n \frac{k_2}{\mu_2} \langle \vec{M}_{e1n}^{(3)}, \vec{M}_{e1n} \rangle_{\rho=x} + d_n \frac{k_1}{\mu_1} \langle \vec{M}_{e1n}^{(1)}, \vec{M}_{e1n} \rangle_{\rho=y} = \frac{k_2}{\mu_2} \langle \vec{M}_{e1n}^{(1)}, \vec{M}_{e1n} \rangle_{\rho=x}. \quad (\text{A.19})$$

Now, upon applying relations similar to Eq. (A.13), the functional inner products are replaced like such:

$$a_n y \xi_n'(x) + d_n x \psi_n'(y) = y \psi_n'(x), \quad (\text{A.20})$$

$$a_n \mu_1 \xi_n(x) + d_n \mu_2 \psi_n(y) = \mu_1 \psi_n(x), \quad (\text{A.21})$$

where $y = mx$ could be used to rewrite these relations into the same form as used by the book of Bohren & Huffman.

Finally, two similar equations may be derived for the coefficients b_n and c_n . Upon solving this system of equations, the Mie coefficients as given in Eqs. (1.31 and 1.32) will follow.

B

OPTOFLUIDS CODE IMPLEMENTATION

In this appendix, we will explain the inner workings of our developed codes at a more technical and practical level. All codes are made publicly available, as listed in the [List of Publications](#) on page 137. In the following sections, we'll first discuss the fluids code, then the optics code, and finally the workflow of how they are coupled.

B.1. FLUIDS

In Chaps. 4 and 5, we did not use a dedicated [Computational Fluid Dynamics \(CFD\)](#) code to simulate the fluid flow. Instead, we generated random particle positions based on a realistic volume distribution (see Sec. 2.2.1), and evolved their positions over time using exact solutions (see Sec. 1.3).

In Chap. 6, we have used OpenFOAM v2.4.x, as obtained from the official GitHub repository May 29th 2015 [1]. Additionally, we have used the pyFoam and swak4Foam add-ons (e.g., to use Python to set the initial particle positions based on the realistic volume distribution). PyFoam was obtained June 9th 2015 using the official subversion repository [2]. Swak4Foam was obtained May 29th 2015 using the official subversion repository [3].

The choice for OpenFOAM is rather arbitrary: any [CFD](#) code could be used (e.g., Ansys Fluent), provided that it can simulate blood, as well as newer versions of OpenFOAM. OpenFOAM was initially chosen for two reasons: (1) our past experience and (2) the open-source character of OpenFOAM, making it easier to couple the optics code with the fluids code. The latter turned out to be an unnecessary requirement, because there is no reason to design the code as a monolithic code: the optics code depends on the fluids code's output, but the fluids code does not need any feedback from the optics code (unlike in, e.g., fluid-structure interaction problems).

B.2. OPTICS

B.2.1. CLASSES / DATA STRUCTURE

Fig. B.1 shows a class UML diagram for the optics part of our code. The classes are primarily a way to store the parameters of the algorithm in a convenient way. Sphere-Manager provides an interface for the algorithm to access the spheres. Sphere permits easy storage of per-sphere information (see Fig. 2.3 and the surrounding text). Camera holds information about the camera's pixels and accumulates the electric field.

The modules are the computational machinery of the algorithm. main is the starting point of the code, which can be an external code (see Sec. B.3). MieAlgorithmFF performs the algorithm as described in Sec. 2.1. bhmie is the algorithm from Bohren & Huffman [4], adapted to our needs (see Sec. 2.1.1). IO is responsible for the **Input & Output (I/O)** part of the code: read the input parameters, read the particle positions and write the intensity to a file.

To greatly speed up the code, the value of the scattering matrix was approximated through interpolation based on precomputed values (see Sec. 2.1.5). This was achieved by creating a new ScatteringStrategy class, abstracted through an **adapter interface**. Through an input file, either a FullBHMie or an InterpolationScatteringStrategy object is instantiated, which is subsequently used by MieAlgorithmFF to either recompute or interpolate the scattering matrix respectively.

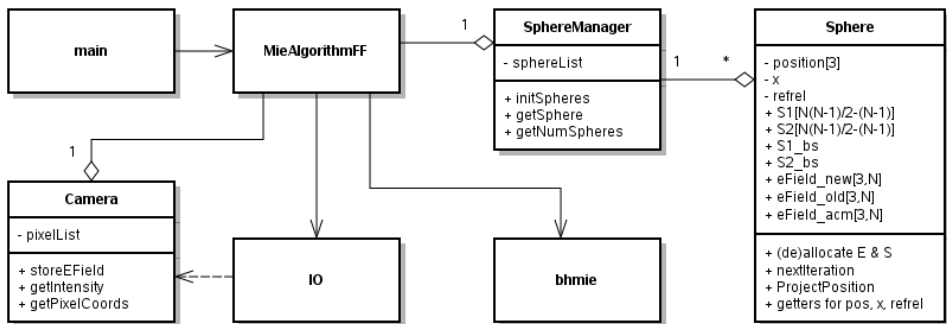


Figure B.1: Class UML diagram for the **MSFF** code. The code consists of both modulated programming and **Object-Oriented Programming (OOP)** codes. Modules are shown as just a name. Objects are shown as a class: name, variables, and methods. The normal arrows show how modules depend on each other with the source of the arrow being the owner. The striped arrow shows a dependency without ownership. MieAlgorithmFF also owns an instance of a child of ScatteringStrategy, which is not depicted in the figure.

B.2.2. PSEUDOCODE OF THE ALGORITHMS

Our implemented algorithms are shown in Algs. 1-5 in pseudocode. Alg. 1 shows the main procedure of our code. The other algorithms are procedures called by either the main procedure or by other procedures. In each algorithm, the appropriate equations from this thesis are referenced where they are computed.

Algorithm 1: Global structure of the MieAlgorithmFF module. See Fig. 2.2 in particular.

Input: A set of particles $\{\vec{r}, a, m\}$, \vec{k}_i , and the camera (size, position, orientation)

Result: The intensity profile on the camera written to a file

- 1 `init()`: read input files and instantiate classes
- 2 Do Alg. 2: `initialScatter()`: $p = 1, 2$ scattering order
- 3 Do Alg. 3: `multiScatter()`: $p > 2$ scattering order
- 4 Do Alg. 4: `scatter2Camera()`: scatter the accumulated field Eq. (2.8) to the camera, cf. Eq. (2.7).
- 5 `output()`: compute the resulting intensity Eq. (2.9) and write to an output file

Algorithm 2: Global structure of the initialScatter algorithm

Input: SphereManager, \vec{k}_i, \vec{E}_i

Result: Computed $[S]$ (to be used by 'multiScatter') and updated the \vec{E} 's of all spheres

- 1 **forall** *particles, i* **do**
- 2 | Allocate all arrays
- 3 **end**
- 4 **forall** *'via' particles, i* **do**
- 5 | // Compute the $p = 1$ field:
- 6 | Compute $\vec{E}_{ii}^0 = \vec{E}_i e^{ikz_i}$, cf. Eq. (1.47)
- 7 | Store it directly into the accumulator $\vec{E}_{ii}^{\text{accum}}$
- 8 | // Compute the $p = 2$ field:
- 9 | **forall** *'target' particles, j ≠ i* **do**
- 10 | | Compute the scattering angle, θ_s , from the incident field via i to j .
- 11 | **end**
- 12 | Call `bhmie`($\{\theta_s\}$) to find all $[S]_{jii}$
- 13 | **forall** *'target' particles, j ≠ i* **do**
- 14 | | Use $[S]_{jii}$ to scatter the field: from \vec{E}_{ii}^0 to $\vec{E}_{ji}^1 = \vec{E}_{ji0}^1$, cf. Alg. 5.
- 15 | | Accumulate to $\vec{E}_{ji}^{\text{accum}}$ (cf. Eq. (2.8)).
- 16 | **end**
- 17 | // Prepare for multiscattering:
- 18 | **forall** *'target' particles, j ≠ i* **do**
- 19 | | **forall** *'source' particles, l < j ∩ l ≠ i* **do**
- 20 | | | Compute the scattering angle, θ_s , from l via i to j .
- 21 | | **end**
- 22 | **end**
- 23 | Call `bhmie`($\{\theta_s\}$) to find all $[S]_{jil}$
- 24 | Call `bhmie`(π) to find the backscattering matrix $[S]_{bs} \approx [S]_{jij}$
- 25 **end**

Algorithm 3: Global structure of the multiScatter algorithm

Input: SphereManager
Result: Computed all \vec{E} 's of all spheres. $\vec{E}_{ji}^{\text{accum}}$ will be scattered to the camera

```

1 forall scattering orders, p do
2   forall 'via' particles, i do
3     | Call spherei.nextIteration()
4   end
5   forall 'via' particles, i do
6     | forall 'target' particles, j do
7       | forall 'source' particles, l do
8         | | Use [S]jil to scatter the field: from  $\vec{E}_{il}^{p-1}$  to  $\vec{E}_{jl}^p$ , cf. Alg. 5
9         | | Accumulate to  $\vec{E}_{ji}^p$  cf. Eq. (2.3).
10        | end
11       | end
12      end
13     forall i, j do
14       | Accumulate to  $\vec{E}_{ji}^{\text{accum}}$  cf. Eq. (2.8).
15     end
16     If converged, then break the p-loop. Else continue.
17 end

```

Algorithm 4: Global structure of the scatter2Camera algorithm

Input: SphereManager, Camera
Result: The camera now has a measured electric field for every pixel, c

```

1 forall 'via' particles, i do
2   forall 'source' particles, l do
3     | forall camera pixels, c do
4       | | Compute the scattering angle,  $\theta_s$ , from l via i to c.
5       | end
6     end
7     Call bhmie( $\{\theta_s\}$ ) to find all [S]cil
8     forall 'source' particles, l do
9       | forall camera pixels, c do
10        | | Use [S]cil to scatter the field: from  $\vec{E}_{il}^{\text{accum}}$  to  $\vec{E}_{cil}$ , cf. Alg. 5
11        | end
12        | Call camera.addEField( $\vec{E}_{cil}$ ) to slowly accumulate to  $\vec{E}_c^{\text{scattered}}$  cf. Eq. (2.7)
13       | end
14     end
15 Optionally add  $\vec{E}_c^0$  (which is incident on the camera, but not part of the scattered field)

```

Algorithm 5: Global structure of the S2E function**Input:** $[S], \vec{E}_i, \vec{z}, \vec{k}_i$ **Output:** \vec{E}_s **Result:** Scattered an incoming PW to a scattered PW, cf. Eq. (2.4)

- 1 Find $\{\hat{E}_{i\parallel}, \hat{E}_{i\perp}, \hat{E}_{s\parallel}\}$ using clever cross products
- 2 Compute $E_{i\perp}$ and $E_{i\parallel}$ by projection
- 3 Compute $E_{s\perp}$ and $E_{s\parallel}$, cf. Eq. (1.44)
- 4 Compute $\vec{E}_s = E_{s\perp}\hat{E}_{i\perp} + E_{s\parallel}\hat{E}_{s\parallel}$
- 5 Include the $e^{ikz}/(-ikz)$ term of Eq. (1.44)

B.3. OPTOFLUIDS: COMBINING THE WORKFLOW

In an OptoFluids simulation, the previously explained fluids and optics codes are executed in sequence. The magic glue is provided by the coupling and post-processing scripts which fully automate a full OptoFluids simulation. These are programmed in Bash (.sh) and Python (.py). The entire workflow is displayed in Algs. 6-12 as pseudocode, which are all ultimately ran through Alg. 6.

Algorithm 6: Overarching workflow, runAll.sh**Input:** Input file with the required OptoFluids variables**Result:** The fluids and optics codes are ran in succession

- 1 Enter the 'fluids' directory
- 2 Execute runAll.sh (Alg. 7 or Alg. 8)
- 3 Return to the root directory
- 4 Execute coupling script (Alg. 9)
- 5 Enter the 'optics' directory
- 6 Execute runAll.sh (Alg. 10)
- 7 Return to the root directory

Algorithm 7: CFD: fluids/runAll.sh : exact solution version

Input: Input file with the required OptoFluids variables, and a setup CFD geometry and simulation parameters

Result: Computed particle positions for each timestep.

- 1 Generate N particles at random positions, either through a uniform or through a specified volume distribution (see Sec. 2.2.1)
- 2 **forall** *timesteps* **do**
- 3 **forall** *particles* **do**
- 4 Compute the particle's position at the current timestamp, using the specified exact solution (see Sec. 1.3)
- 5 **end**
- 6 **end**

Algorithm 8: CFD: fluids/runAll.sh : OpenFOAM version

Input: Input file with the required OptoFluids variables, and a setup CFD geometry and simulation parameters

Result: Computed velocity and pressure fields and particle positions for each major timestep, Δt .

- 1 Perform some sanity checks
- 2 Prepare the case (e.g., generate the mesh and prepare OpenFOAM input files)
- 3 Copy the "case" template to "case_IC" (*'IC' stands for 'Initial Condition'*)
- 4 Run the "case_IC" simulation until a steady state is reached; this will serve as the initial condition for the actual simulation, below
- 5 Delete everything but the last timestep from "case_IC", and rename it to time 0
- 6 Copy "case_IC" to "case_run"
- 7 Run "case_run" for the duration specified in the OptoFluids input file
- 8 Copy "case_run" to "case_us" (*'us' stands for 'microsecond'*)
- 9 **forall** *Timestamps in "case_run"* **do**
- 10 Write 'timestamp' as starting time, Δt_{int} as timestep, and t_{int} as duration to 'system/controlDict' (see Fig. 4.2)
- 11 Perform the **microstepping** simulation
- 12 **end**
- 13 Optional: post-processing if the specific case needs it

Algorithm 9: Coupling: convert the CFD output to the optics input

Input: All particle position files (from the fluids simulation)

Result: All particle position files in the data format required by the optics code

Algorithm 10: Optics: `optics/runAll.sh`: Laser Speckle Imaging (LSI)**Input:** All particle position files and other optics parameters**Result:** An intensity file for each input particle position file

- 1 Substitute all optics parameters into the optics code's input file
- 2 **forall** *particle position files* **do**
- 3 | Substitute the particle position filename into the optics code's template input file, and save it as a temporary input file
- 4 | Run Alg. 1: MieAlgorithmFF
- 5 | Remove the temporary input file
- 6 **end**
- 7 Run Alg. 11: post-processing the output of MieAlgorithmFF

Algorithm 11: Optics: post-processing the file- and data structure**Input:** The file structure of a finished MieAlgorithmFF simulation**Result:** A new output file structure and data structure, that is easier to process further. The mean 'blurred' intensity is computed by averaging over the [camera integration time](#); for each major timestep, Δt , that result is saved to a separate intensity file.

- 1 Convert the camera's 3D (x,y,z)-coordinates into 2D (u,v)-coordinates
- 2 Restructure the 1D list of camera coordinates into a 2D array
- 3 **forall** *intensity output files* **do**
- 4 | Restructure the 1D list of intensity values into a 2D array, based on the camera's (u,v)-coordinates
- 5 **end**
- 6 Create one directory per major timestamp (from timestep Δt , see Fig. 4.2)
- 7 Sort the [microstepped](#) Δt_{int} intensity files into the appropriate major timestamp directory
- 8 **forall** *major timestamp directories, mimic the camera integration time* **do**
- 9 | For each camera pixel: compute the average intensity from all intensity files
- 10 | Save the averaged data into a new 'blurred' mean intensity file
- 11 **end**
- 12 Optional: run Alg. 12 to further post-process the data into results

Algorithm 12: Optics: compute the [speckle contrast](#)**Input:** Intensity files in the post-processed 2D array format from Alg. 11**Result:** Metrics, such as the speckle contrast

- 1 Compute the speckle contrast of the (blurred) intensity files, cf. Eq. (4.6)
- 2 Compute the [Fourier transform](#) of the speckle contrast data
- 3 Plot the speckle contrast and its Fourier transform
- 4 Optional: plot colored contour plots of the (blurred) intensity files
- 5 Optional: turn the contour plots into a video to visualize speckle motion

BIBLIOGRAPHY OF APPENDICES

1. OpenFOAM-2.4.x. *Github* <https://github.com/OpenFOAM/OpenFOAM-2.4.x> (OpenFOAM Foundation, Maya 22nd 2015).
2. Gschaider, B. *openfoamwiki.net:Contrib/PyFoam* <http://openfoamwiki.net/index.php/Contrib/PyFoam> (OpenFOAM Foundation, 2015).
3. Gschaider, B. *openfoamwiki.net:Contrib/swak4Foam* <http://openfoamwiki.net/index.php/Contrib/swak4Foam> (OpenFOAM Foundation, 2015).
4. Bohren, C. F. & Huffman, D. R. *Absorption and Scattering of Light by Small Particles* Wiley Professional Paperback. ISBN: 0-471-05772-X (John Wiley & Sons, Inc., 1998).

CURRICULUM VITÆ

Kevin VAN AS

19-05-1992 Born in Alphen aan den Rijn, The Netherlands.

EDUCATION

2015–2024 PhD. Physics
Technische Universiteit Delft, Delft
Thesis: Dynamic laser speckle imaging for velocimetry in blood flow: A Numerical Study
Promotors: Dr. N. Bhattacharya, Prof. Dr. S. Kenjereš, Dipl.-Ing., and Prof. Dr. Ir. C.R. Kleijn

2019–2021 MSc Physics teacher (voorbereidend hoger onderwijs, eerstegraads),
ICLON, Universiteit Leiden, Leiden

2013–2015 MSc Applied Physics
Technische Universiteit Delft, Delft
Honours Track Master, Excellence Track in Solid & Fluid Mechanics

2010–2013 BSc Applied Physics
Technische Universiteit Delft, Delft
Honours Track Bachelor, Minor in Software Development

2004–2010 High school
Ashram College, Alphen aan den Rijn

AWARDS

2015 Shell Afstudeerprijs voor Natuurkunde, KHMW
2015 The Student Prize Applied Physics 2014-2015, TU Delft
2014 Grant for my PhD proposal, NWO via J.M. Burgerscentrum
2011 Aanmoedigingsprijs, KHMW

VOLUNTEERING

2018–present Mentor and content-lead of TechCamps at Tweehek Jeugdvakanties
2017–present Founder of and mentor at CoderDojo Alphen aan den Rijn

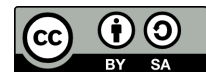
LIST OF PUBLICATIONS

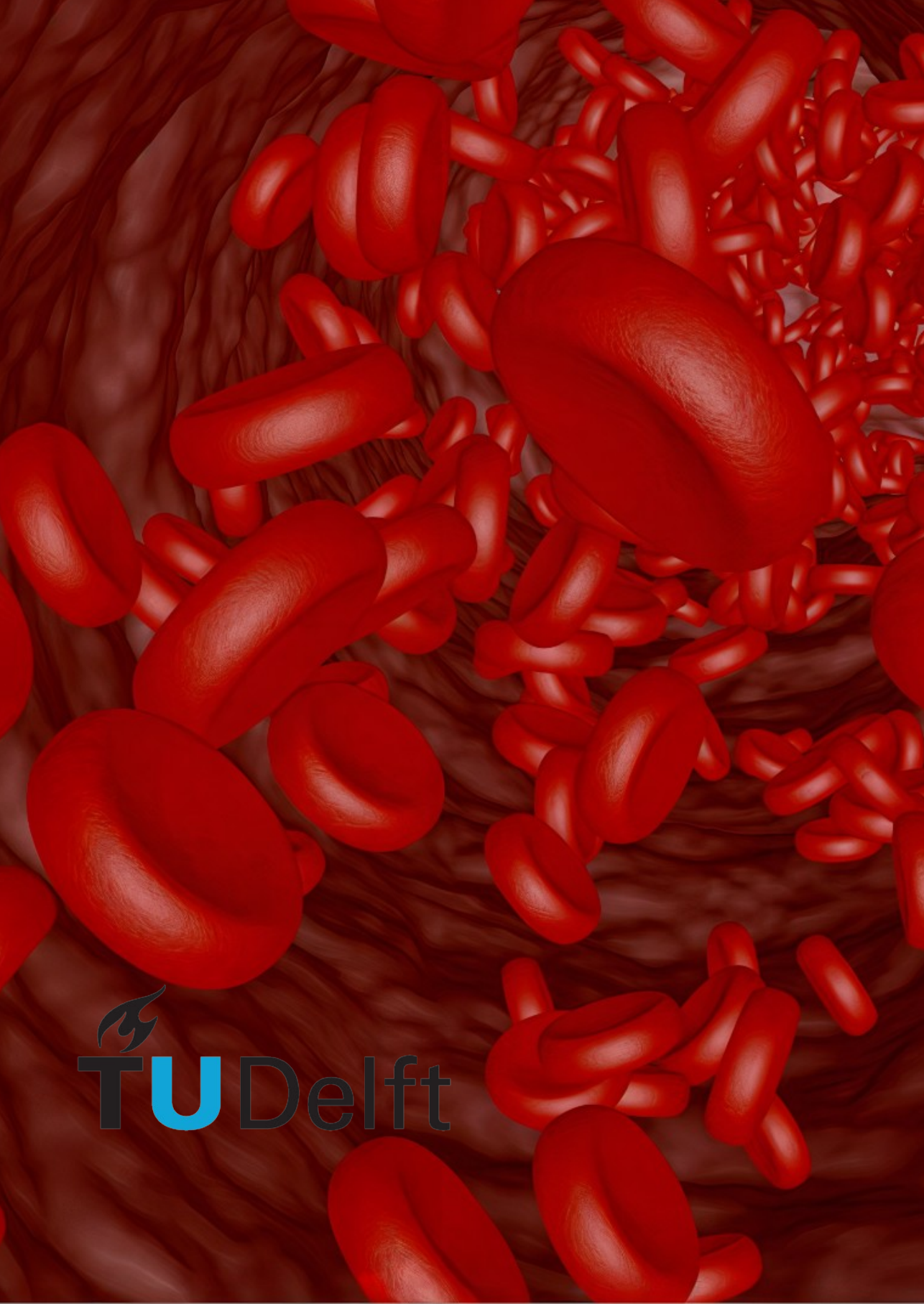
RESEARCH PAPERS

4. **Van As, K.**, Dellevoet, S. F. L. J., Boterman, J., Kleijn, C. R., Bhattacharya, N., & Kenjeres, S. (2022). *Toward detecting atherosclerosis using dynamic laser speckle contrast imaging: A numerical study*. *Journal of Applied Physics*, 131(18), 184902.
3. **Van As, K.**, Simons, B. A., Kleijn, C. R., Kenjeres, S. & Bhattacharya, N. (2022). *The dependence of speckle contrast on velocity: A numerical study*. *Journal of the European Optical Society - Rapid Publications*, 18(2), 11.
2. **Van As, K.**, Boterman, J., Kleijn, C. R., Kenjeres, S., & Bhattacharya, N. (2019). *Laser speckle imaging of flowing blood: A numerical study*. *Physical Review E*, 100(3), 033317.
1. Mukherjee, S., Zarghami, A., Haringa, C., **van As, K.**, Kenjereš, S., & Van den Akker, H. E. (2018). *Simulating liquid droplets: A quantitative assessment of lattice Boltzmann and Volume of Fluid methods*. *International Journal of Heat and Fluid Flow*, 70, 59-78.

CODE REPOSITORY

The codes used in this thesis, as are described in Chap. 2, are publicly available and published through GitHub: <https://github.com/floquation/optoFluids>. You are free to use our code for any purpose, provided that you cite at least our 2019 paper in your publications. Should you expand upon our code and publish your new version, then please cite both our 2019 paper and our original code repository.






TUDelft